AN INVESTIGATION OF THE TRANSPORT PROPERTIES OF HOLES IN A SEMICONDUCTING DIAMOND

By

LEONARD CHESTER LASKOWSKI

Bachelor of Arts

Saint Mary's College

Winona, Minnesota

1964

Submitted to the Faculty of the Graduate College
of the Oklahoma State University
in partial fulfillment of the requirements
for the Degree of
DOCTOR OF PHILOSOPHY
July, 1972

AN INVESTIGATION OF THE TRANSPORT PROPERTIES OF HOLES IN A SEMICONDUCTING DIAMOND

Thesis Approved:

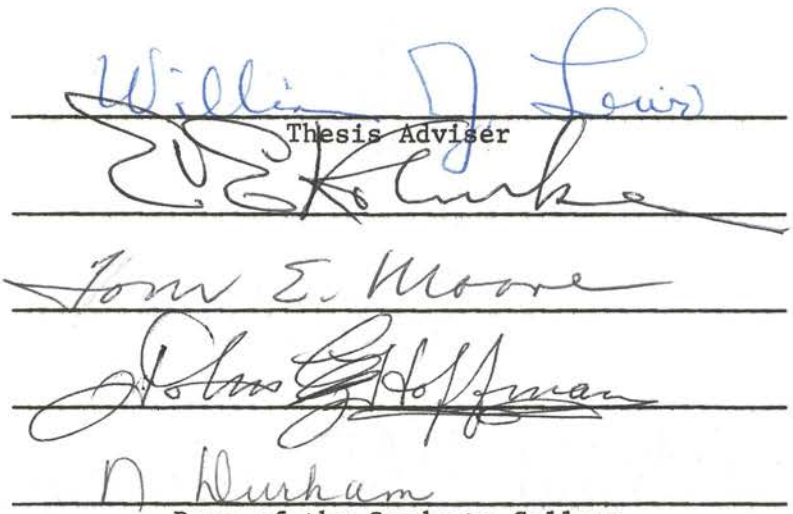

Thesis Adviser

Dean of the Graduate College

ACKNOWLEDGEMENTS

I wish to express my gratitude to Dr. W. J. Leivo, who kindly allowed me to pursue a relatively independent path of research, but who was constantly willing to give useful advice. Thanks are also given to the members of my committee, Dr. E. E. Kohnke, J. E. Hoffman, Dr. T. E. Moore and former members of my committee, Dr. F. C. Todd and Dr. H. L. Jones for their aid and cooperation. I would also like to thank Dr. H. E. Harrington, former Head of the Physics Department, and Dr. W. A. Sibley, Head of the Physics Department, for aid in obtaining some of the equipment necessary for this study.

The traineeship support provided by the National Aeronautics and Space Administration (1966-1969) and administered through the Research Foundation of Oklahoma State University is gratefully acknowledged.

I acknowledge indebtness to the Physics and Chemistry Shop personnel, H. Hall, R. Gruhlkey, F. Vulgamore, and F. Hargrove for making the pulse magnets and other hardware necessary for this study. The assistance of W. Rhodes in redesigning the electronics of the capacitive energy storage system is acknowledged. The use of the Oklahoma State University computing facilities was generously supported by the University.

Gratitude is expressed to Dr. J. F. H. Custers, Research Consultant, and Dr. H. B. Dyer, Director of Research of the Diamond Research Laboratory, both of Industrial Distributors (1946) Limited for furnishing

semiconducting diamonds in our collection. Thanks also go to Dr. G. Switzer of the U. S. National Museum for the loan of a semiconducting diamond.

Most of all, I wish to thank my wife, Mary, for her continual patience and encouragement throughout my graduate study.

TABLE OF CONTENTS

LIST OF TABLES

LIST OF FIGURES

CHAPTER I

INTRODUCTION

Preliminary Remarks

In the absence of a magnetic field, the symmetry of the diamond lattice requires the vanishing of all off-diagonal elements and the equality of all diagonal elements of the conductivity tensor. However, in the presence of a magnetic field, the conductivity tensor is no longer a constant tensor. Information leading to conclusions of this type were discovered in two experiments performed in the nineteenth century. Sir Wm. Thomson (1) first observed, in 1856, that a magnetic field caused an increase in resistance of iron when longitudinally magnetized. In 1879, E. H. Hall (2) found that an electric field was set up in a gold leaf in a direction perpendicular to both the direction of the current and of the magnetic field when the magnetic field is applied at right angles to the direction of the current flow. These two phenomena, known as magnetoresistance and Hall effect, are labeled as transport phenomena because they involve the spatial motion of charged particles within the crystal as well as the transfer of both energy and momentum (3). The transport properties are then the set of parameters, which can be extracted from the observation of galvanomagnetic effects, describing the motion of the charge carriers, as well as the types of interaction they experience, within the crystal.

In the presence of a magnetic field, the motion of a hole traces

out a helix whose axis points along the magnetic field direction. When the frequency ω of the circular motion, called the cyclotron frequency, multiplied by the relaxation time τ yields a product much less than unity, the galvanomagnetic measurements are being done in the low-field region. Pictorially, the charge carriers traverse only a small fraction of the cyclotron orbit before being scattered (4). The magnetoresistance will vary as the square of the magnetic field strength; the Hall coefficient will not be a direct measure of the density of holes. In diamond, the upper limit of this region occurs at a magnetic field around six kilogauss.

Increasing the magnetic field strength until $\omega\tau \gg 1$ allows the hole to traverse more than one cyclotron orbit before being scattered. Quantum effects will not be detected in this region, called the classical high-field region, because the thermal spread in the energy of a hole is larger than the energy difference between quantizied energy levels. This second requirement could alternately be written as $kT \gg \hbar\omega$ where k is Boltzmann's constant, T is the temperature of the diamond and $\hbar$ is Planck's constant divided by 2π. Thus, energy levels with large quantum numbers will be occupied, and the behavior of the holes will be that of a classical system. For large enough magnetic fields, the magnetoresistance will saturate to a value dependent on the energy dependence of the relaxation time, and the Hall coefficient will be independent of the relaxation time and a direct measure of the density of holes in the diamond. This is the type of information that can be determined about hole conduction in diamond when galvanomagnetic measurements are made in large magnetic fields.

Previous Galvanomagnetic Studies of Diamond

All of the known transport studies of diamond, except one, have been confined to the low-field region. Information extracted from these studies will be reviewed in the paragraphs that follow.

The first measurement of the Hall effect of type IIb blue-white diamond was reported by J. J. Brophy (5). He found that the Hall coefficient was independent of the magnetic field up to fields of ten kilogauss; the Hall mobility at room temperature was 1400 cm^2/volt-sec.

I. G. Austin and R. Wolfe (6) measured the Hall coefficient of a 'natural blue' semiconducting diamond over the temperature range of -100°C to 600°C. The geometrically corrected Hall mobility at room temperature was 1550 $\pm$ 150 cm^2/volt-sec., and it varied as $T^{-3/2}$ over the range of temperatures of 0°C to 100°C. No magnetoresistance was detected in magnetic fields up to four kilogauss.

The Hall coefficient of six semiconducting diamonds were measured by P. T. Wedepohl (7) as a function of temperature from 200°K to 800°K. His results indicated that the room temperature Hall mobility, which varied from specimen to specimen, was in the range 1300 $\pm$ 200 cm^2/volt-sec. At 500°K, the mobility of the specimens were in the neighborhood of 460 $\pm$ 100 cm^2/volt-sec. The temperature dependence of the Hall mobility varied continuously up to 500°K; for higher temperatures, it varied approximately as $T^{-2.8}$. A preliminary report on the transverse magnetoresistance of one specimen was made; the details of this effect was more fully reported in another paper by E. W. J. Mitchell and P. T. Wedepohl (8). The transverse magnetoresistance, corrected for geometrical effects, reasonably satisfied the relationship

$$\Delta R/(R_0 H^2) = 3.54 \times 10^{-10} \text{ gauss}^{-2}$$

for magnetic fields between 1.5 and 4 kilogauss. The magnetoresistance was also measured as a function of the angle between the electric and the magnetic field vectors. The results were used to evaluate the coefficients in the theory proposed by F. Seitz for the low-field magnetoresistance of cubic semiconductors. The longitudinal magnetoresistance was found to be about one third of the transverse magnetoresistance.

R. T. Bate and R. K. Willardson (9) measured the transverse magnetoresistance and Hall coefficient of two type IIb semiconducting diamonds as a function of the magnetic field at fixed temperatures between $0^{o}C$ and $100^{o}C$. At low fields, the magnetoresistance was proportional to H^2 but deviates from this behavior above four kilogauss. It was suggested that a warped valence band could explain that the magnetoresistance was larger than expected for a spherical band. They noticed that the Hall coefficient increased as the magnetic field increased. They remarked that the field dependence is usually associated with a warped energy band. That the Hall coefficient was still field dependent at weak magnetic fields suggested a warped light-mass band and associated high mobility holes.

A. C. Beer (10) reported a quantitative study of the magnetic field dependence of the Hall coefficient of a semi-conducting diamond. Positioning the maximum in the Hall coefficient factor data at the same value of the magnetic field parameter $(\gamma_2)^{\frac{1}{2}}$ as determined for silicon required that the heavy-hole lattice scattering mobility be about eight times larger than expected from $R_0 \sigma_0$ data and from magnetoresistance. It was suggested that the scattering treatment used in the analysis may not be applicable to diamond and perhaps the light-mass band is warped.

The room temperature magnetoresistance of three oriented semiconducting diamonds was reported by P. J. Kemmey and E. W. J. Mitchell (11). They measured the ratio $\Delta R/(R_0 H^2)$ for orientations of the electric and magnetic fields along the high symmetry axes of the diamond lattice. The results of the experiments were used to determine the components of the magnetoconductive tensor and to compare with calculations carried out for a triply degenerate valence band, assuming that the energy surfaces can be approximated by two warped spheres and one sphere. Using a power law dependence of the relaxation time, they estimated that their model accounted for the magnetoresistance within a factor of two.

W. J. Leivo et. al. (12) measured the Hall coefficient of the white end of the specimen used in this investigation as a function of temperature from room temperature to 527°C. The Hall coefficient was essentially constant with respect to its magnetic field dependence; the room temperature Hall mobility, corrected for the geometry of the sample, was found to be 1300 cm^2/volt-sec.

R. L. Schelhorn and H. G. Nordlin (13) measured the Hall coefficient of three semiconducting diamonds as a function of temperature in the range of 100°K to 900°K. The Hall mobility was observed to vary with temperature as $T^{-2.8}$ for temperatures above 400°K. The room temperature Hall mobility varied from sample to sample; it was within the range 1000 $\pm$ 300 cm^2/volt-sec.

The magnetoresistance of the blue end of a semiconducting diamond (the one used in this investigation) was measured by K. J. Russell (14, 15) in pulsed magnetic fields up to 170 kilogauss. Measurements made in dc magnetic fields closely agreed with those made using a pulse magnet. The longitudinal magnetoresistance was measured in the $[\bar{1}11]$

and $[1\bar{1}3]$ directions and the transverse magnetoresistance was measured for four orientations of the magnetic and electric field vectors. The results of the experiment were compared with the theory for an isotropic, isothermal solid which is based on the assumptions of three uncoupled valence bands with spherical energy surfaces and mixed scattering by lattice vibrations and ionized impurities. Fitting the theoretical curve to the transverse magnetoresistance for the current in the $[1\bar{1}3]$ direction and the magnetic field in the $[110]$ direction led to the values for the lattice scattering mobilities of 3900 $cm.^2$/volt-sec., 195 $cm.^2$/volt-sec., and 1365 $cm.^2$/volt-sec. for the light hole band, the heavy hole band, and the split-off band respectively. Ionized impurity scattering was found to be less important than lattice scattering.

Present Study

The experimental objective of this paper is to report the measurement of both the magnetoresistance and the Hall effect of the blue end of a particular diamond specimen at the temperatures of $307.7 \pm 0.5^{o}K$ ($308^{o}K$) and $436 \pm 3^{o}K$ ($436^{o}K$). The diamond specimen is known as DS-2; this shorthand nomenclature will be used at appropriate places in this paper. The blue end is chosen because of its lower resistivity. The experimental measurements, in most instances, were made with two independent sets of electrical probe contacts on DS-2. Repeating these galvanomagnetic measurements allowed some speculation as to the homogeneity of the blue end of DS-2.

The theoretical objective of this paper is to quantitatively analyze the magnetoresistance and Hall effect using the theoretical framework which has been developed and used for the last twenty years.

The results of the analysis cast only a diffused light as to why the conventional approach to transport phenomena in semiconductors does not yield consistent parameters with which to describe the transport properties of holes in semiconducting diamond.

The objective of making galvanomagnetic measurements in high magnetic fields is that they give influential information as to the transport properties of holes. The information is clearest when exacting procedures have been followed. Of critical importance is ascertaining the homogeneity of the specimen. Only if a sample is homogeneous, can parameters be extracted which are representative of the bulk characteristics of the material. This statement relative to diamond assumes that naturally-grown diamonds are characterized by homogeneity rather than inhomogeneity. The measurement of the electrical resistivity and magnetoresistivity indicate that the blue end of DS-2 may be inhomogeneous. The next requirement is to reduce the influence of geometry on the measurements by using specimens which are long and rod-like, and positioning the electrical probe contacts far from the electrical current contacts. Because this study was made on the blue end of DS-2, this requirement was not fulfilled. However, it is possible to correct for the influence of the geometry if both the Hall coefficient and the magnetoresistance can be simultaneously measured. Measurements of this type were made; the geometrical corrections could not be made due to the correlation of the Hall coefficient data with the pattern of producing the pulsed magnetic fields. Finally, the electrical contacts should be made in such a manner that they do not influence the measurements. If the homogeneity and geometry requirements were met, it would be easier to analyze the effect of the electri-

cal contacts. Some of the magnetoresistance measurements do indicate that the time varying magnetic field does influence the conductivity properties of the electrical contacts.

CHAPTER II

BASIC CONCEPTS AND EXPERIMENTAL PRECAUTIONS

Magnetoresistance and Hall Effect: Elementary Explanation

A typical arrangement of an experiment to measure the magnetoresistance and Hall effect of a rectangular parallelepiped is shown in Figure 1. The current contacts, labeled #5 and #6, cover each end of the sample in order to provide a uniform current density in the x-direction throughout the sample. Four potential probe contacts, small in area so as not to greatly disturb the uniformity of the current, are put on the surfaces whose normal is the y-axis. The outermost point contacts on the upper surface, labeled #1 and #2, are used to measure the potential difference associated with the magnetoresistance (called magnetoresistance contacts), while the two remaining point contacts, labeled #3 and #4, are used to measure the Hall voltage (called Hall effect contacts). The probe contact lead wires are connected to a switch S arranged to measure either one or the other of the voltages with a potentiometer. A steady current is supplied by the battery B; the resistance R in series with the sample is chosen to be large compared with the sample resistance (whether the sample is in or out of the magnetic field) so that the current is approximately independent of the magnetoresistance effect. The voltage across the standard resistor R_s, measured with a potentiometer, is used to determine the current in the

sample. A steady magnetic field H, supplied by an electromagnet not shown in Figure 1, is directed along the z-axis.

The magnetoresistance at the field H is the ratio of the change in the electrical resistance at that field to the resistance of the sample in vanishing magnetic field. It is expressed by the relation

$$\frac{\Delta \rho}{\rho_0} = \frac{\rho(H) - \rho(0)}{\rho(0)} = \frac{V(H) - V(0)}{V(0)} = \frac{\Delta V}{V_0} \qquad (1)$$

where $\rho(H)$ is the resistivity of the sample in a magnetic field of strength H and $\rho_0 = \rho(0)$ is the resistivity in vanishing magnetic field. The change in the potential difference between the magnetoresistance probe contacts is $V(H) - V(0)$ while $V(0) = V_0$ is the corresponding potential difference in vanishing magnetic field. The symbol Δ is defined by the first equality sign and is used throughout the text in this capacity. If the magnetic field is directed along the z-axis, the magnetoresistance is labeled as a transverse effect. If, instead, the magnetic field is directed along the x-axis, the magnetoresistance is labeled as a longitudinal effect.

The Hall coefficient of the sample is expressed by the quantity

$$R_H = \frac{V_H T}{HI} \qquad (2)$$

where V_H is the Hall voltage in the magnetic field H, I is the sample current in the x-direction, and T is the thickness of the sample in the direction of the magnetic field.

An elementary explanation of the Hall effect and transverse magnetoresistance can be given on the basis of the particle nature of conduction. Since many reviews on the subject exist in the literature,

especially the articles written by F. J. Blatt (16), and E. N. Adams and R. W. Keyes (17), only the highlights of the results will be discussed. As a specific example, consider a p-type semiconductor in which the energy band structure consists of a single valence band composed of spherical energy surfaces. The transverse magnetoresistance satisfies the relation

$$\lim_{H \to 0} \left(\frac{\Delta \rho}{\rho_0} \right) = \left(\frac{eH}{m^* c} \right)^2 \frac{\langle \tau \rangle^3 \langle \tau \rangle - \langle \tau^2 \rangle^2}{\langle \tau \rangle^2}$$

in the low-field region, while in the high-field region, it saturates to the value

$$\lim_{H \to \infty} \left(\frac{\Delta \rho}{\rho_0} \right) = \frac{\left(\left\langle \frac{1}{\tau} \right\rangle \right)^{-1} - \langle \tau \rangle}{\langle \tau \rangle} .$$

The quantities e, m*, c, and H are respectively the electric charge and effective mass of the hole, the velocity of light, and the strength of the magnetic field. An average of a power of the relaxation time τ over the Boltzmann distribution of energy among the holes in the crystal is indicated by a set of angular brackets. If τ were independent of the energy of a charge carrier, there would not be a magnetoresistance. Pictorially, the force on a charge carrier due to the Hall field exactly cancels the Lorentz force due to the magnetic field, and the charge carrier is not deflected from its longitudinal motion within the crystal. The energy dispersion of the relaxation time τ, which can be determined from the saturation value of the magnetoresistance, is responsible for the magnetoresistance effect; the force on a charge carrier due to the Hall field does not cancel the Lorentz force, and the carrier is deflected from a longitudinal motion within the crystal.

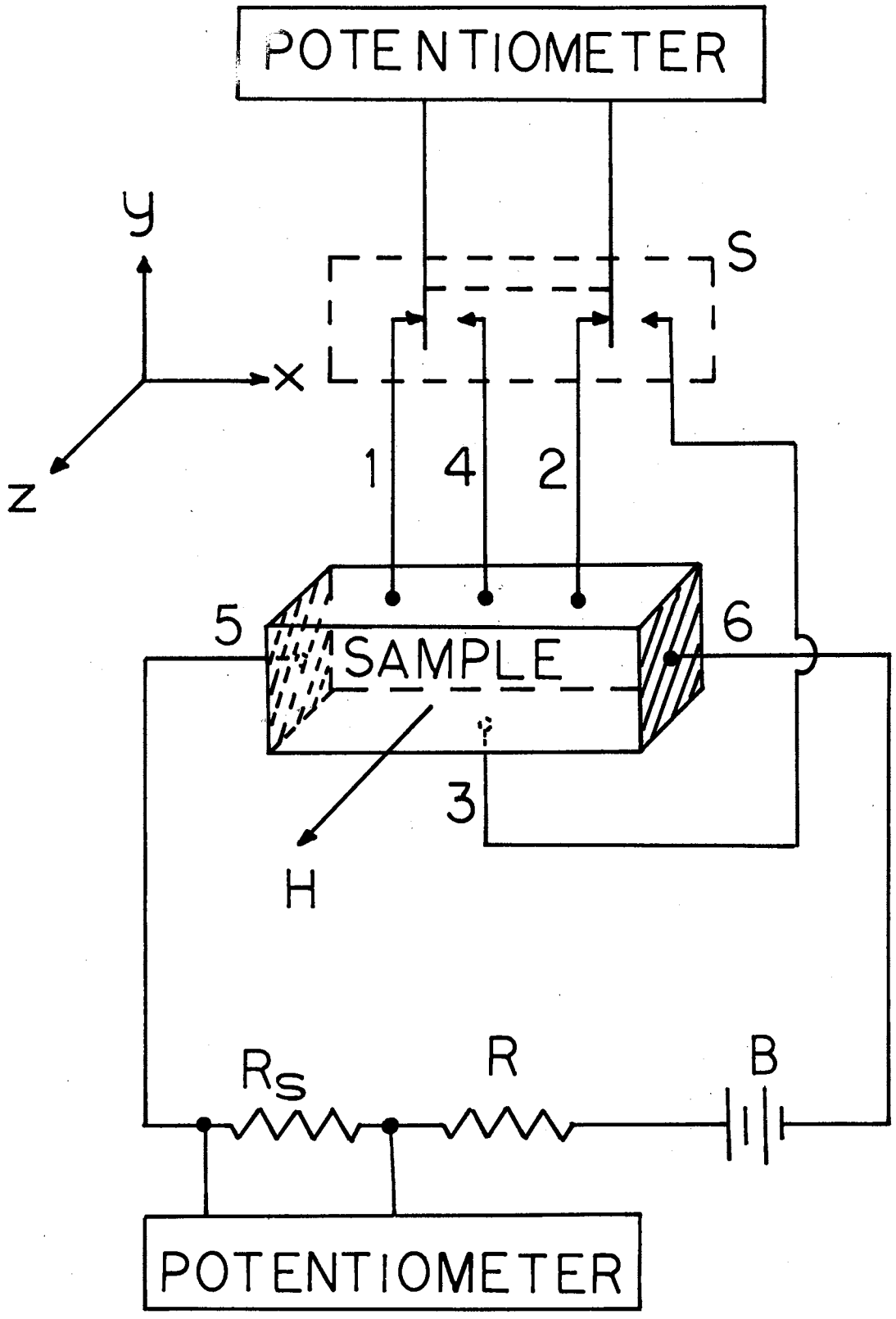

Figure 1. Experimental Arrangement for Galvanomagnetic Measurements

The Hall coefficient satisfies the relation

$$R_{H\to 0} = \frac{1}{pec}\,\frac{\langle\tau^2\rangle}{\langle\tau\rangle}$$

in the low-field region, while in the high-field region, it saturates to the value

$$R_{H\to\infty} = \frac{1}{pec} \quad .$$

The quantity p is the density of holes within the crystal. Only in large magnetic fields is the Hall coefficient independent of the energy dispersion of the relaxation time and a measure of the carrier density.

As an example of the complexity arising in a multicomponent system, the example of extrinsic p-type germanium will be considered. Only the highlights of an article written by R. K. Willardson, T. C. Harman, and A. C. Beer (18) will be presented. The parameters of the heavy hole valence band, indicated by the subscript "2", are the lattice scattering mobility in the limit of vanishing magnetic field μ_2 and the particle density p_2 associated with spherical energy surfaces characterized by an effective mass m_2. The subscript "3" labels similar parameters characterizing the light hole valence band. In the limit of weak magnetic fields, the magnetoresistance is

$$\lim_{H\to 0}\left(\frac{\Delta\rho}{\rho_0}\right) = \frac{9\pi}{16}(\mu_2 H)^2\left\{\frac{1+\left(\frac{p_3}{p_2}\right)\left(\frac{\mu_3}{\mu_2}\right)^3}{1+\left(\frac{p_3}{p_2}\right)\left(\frac{\mu_3}{\mu_2}\right)} - \frac{\pi}{4}\left(\frac{1+\left(\frac{p_3}{p_2}\right)\left(\frac{\mu_3}{\mu_2}\right)^2}{1+\frac{p_3}{p_2}\,\frac{\mu_3}{\mu_2}}\right)^2\right\},$$

and the Hall coefficient is

$$R_{H\to 0} = \frac{3\pi}{8ep_2}\,\frac{1+\left(\frac{p_3}{p_2}\right)\left(\frac{\mu_3}{\mu_2}\right)^2}{\left\{1+\left(\frac{p_3}{p_2}\right)\left(\frac{\mu_3}{\mu_2}\right)\right\}^2} \quad .$$

If the density of fast holes is only two per cent of the density of slow holes and have a mobility eight times as large, the Hall coefficient is 1.7 times as large as that considering only the heavy mass holes. At the same time, the presence of fast holes cause the magnetoresistance to be 30 times larger than that in a crystal with only the slow holes. Thus, the addition of a small amount of high-mobility holes can substantially influence the weak-field galvanomagnetic effects.

In the limit of large magnetic fields, the magnetoresistance saturates to the value

$$\lim_{H\to\infty}\left(\frac{\Delta\rho}{\rho_0}\right) = \frac{32}{9\pi}\,\frac{\left[1+\left(\frac{p_3}{p_2}\right)\left(\frac{\mu_3}{\mu_2}\right)\right]\left[1+\left(\frac{p_3}{p_2}\right)\left(\frac{\mu_2}{\mu^3}\right)\right]}{\left(1+\frac{p_3}{p_2}\right)^2} - 1\,,$$

and the Hall coefficient saturates to the value

$$R_{H\to\infty} = \frac{1}{e(p_2+p_3)}\,.$$

The saturation value of the Hall coefficient is seen to involve only the total density of holes. The ratios of the density and mobility of holes determine the saturation value of the magnetoresistance.

Thermoelectric and Thermomagnetic Effects

The Ettingshausen, Righi-Leduc, and Nernst effects are thermomagnetic effects. They cause a temperature or a potential gradient to exist within the crystal when a magnetic field is applied perpendicular to either the electric or thermal current in the crystal. An elementary explanation of these effects from the viewpoint of the particle nature of conduction is given in the article written by E. H. Putley (19). An estimate of the size of these effects as applied to the diamond DS-2 at a temperature of 300°K is summarized in Table I. It

was assumed that a 10 milliampere current is directed along the x-axis ([110] axis in Figure 24) and that a 150 kilogauss magnetic field is directed along the z-axis ([$\bar{1}$11] axis in Figure 24). The diamond was approximated as having one valence band composed of spherical energy surfaces, and the holes are scattered by interacting with lattice vibrations. The resistivity of the diamond was taken to be 200 ohm-cm., the conductivity mobility as 2000 $cm.^2$/volt-sec., the thermal conductivity (as determined by R. Berman, E. L. Foster, and J. M. Ziman (20)) as 13.5 watts/cm.^oK, and the temperature gradient along the direction of current flow as 20^oK/cm. The temperature gradients associated with the Ettingshausen and Righi-Leduc effects are much smaller than the possible temperature gradients in the oil medium surrounding the diamond specimen. The Nernst effect produces a voltage 6000 times smaller than the Hall voltage which was measured in a 150 kilogauss magnetic field. An error in the estimates by a factor of 100, due to the multicarrier process of conduction in diamond, would not significantly change these conclusions.

The Peltier and Seebeck effects are thermoelectric effects. They cause a temperature or a potential gradient to exist within the crystal when either an electric or a thermal current is present in dissimilar materials (metallic electrical contacts and diamond). An estimate of the size of the potential gradient associated with the Seebeck effect is also given in Table I. The thermoelectric power of the diamond was taken to be 3.5 millivolts/^oK (as determined by H. J. Goldsmid, C. C. Jenns, and D. A. Wright (21)); the thermoelectric power of the metallic current contacts was neglected. The temperature gradient between the current electrodes was determined by putting 100 milliwatts of power into

the diamond. The estimation of the potential gradient is about 1000 times smaller than the potential gradient between the magnetoresistance contacts in measuring the transverse magnetoresistance in a magnetic field of 10 kilogauss.

The Influences of Sample Misalignment

Compromises used in the design of the sample holder (to be described in Chapter III) increased the uncertainity in the orientation of the diamond when positioned in the bore of the electromagnet. Estimates of the uncertainity in the measured magnetoresistance due to sample misalignment can be made from the measurement of the low-field magnetoresistance as a function of the angle θ between the current density and the magnetic field vectors.

The first type of misalignment is that when the angle θ is different from 0^{o} in the case of longitudinal magnetoresistance of different from 90^{o} in the case of transverse magnetoresistance and Hall effect. The experimental set-up is depicted in Figure 2. The data in Figure 3 is that taken in a magnetic field of 5.55 kilogauss with the electric current in DS-2 parallel to the $[1\bar{1}0]$ axis and with a $[11\bar{3}]$ axis of rotation. From the data it can be seen that a misorientation of 5^{o} in measuring the transverse magnetoresistance will cause an error of about 2%, while a 5^{o} misorientation in measuring the longitudinal magnetoresistance will cause an error of about 6%.

The second type of misalignment is that when the angle ϕ is always 90^{o} but the magnetic field is not directed perpendicular to the desired surface of the diamond. The arrangement is illustrated in Figure 4. Figure 5 shows the data taken in a magnetic field of 6.97 kilogauss

TABLE I

ESTIMATE OF THE SIZE OF THE THERMOMAGNETIC AND THERMOELECTRIC EFFECTS IN DIAMOND DS-2

Nernst Coefficient $1X10^{-5} m.^2/^oK$-sec.

Potential Gradient Along the $[1\bar{1}3]$ Axis: 0.3 volts/m.

Ettingshausen Coefficient: $2.2X11^{-6} m.^3 ^oK$/joule

Temperature Gradient Along the $[1\bar{1}3]$ Axis: $4.5X10^{-2} ^oK/m.$

Righi-Leduc Coefficient $3.4X10^{-10} m.^2$/volt-sec.

Temperature Gradient Along the $[1\bar{1}3]$ Axis: $1X10^{-5} ^oK/m.$

Seebeck Effect

Potential Gradient Along the $[110]$ Axis: 0.03 volts/m.

when the electric current density in DS-2 is parallel to the [$\bar{1}$11] axis of rotation. The experimental data reveals that only a 2% error is caused by a 5^{o} misorientation of the magnetic field direction.

These estimates have been made from data taken at the upper limit of the low-field region. In large magnetic fields, the error may be larger.

Geometrical Effects

If the galvanomagnetic properties of a material are determined by experiments using homogeneous specimens which are rod-like in shape and have a length much greater than the width and thickness, the experimental data will be independent of the size of the sample. On the other hand, the configuration of the sample will markedly affect the experimental data if the specimen is short and wide. To understand the influence of the geometry of the specimen on the magnetoresistance and Hall voltage, consider the drawing in Figure 6 for the realistic case of a current in a semiconductor under the influence of a magnetic field. The cross section of the specimen, which is a rectangular parallelepiped, is shown; the magnetic field is perpendicular to the plane of the page. The disturbance of the flow of current due to the finite size of the probe contacts emphasizes the need for extremely small-area probe contacts.

The electric field inside the semiconductor and in front of the current electrodes is, to a good approximation, normal to the plane of the current contacts. This conclusion is based upon the observations that the small Hall coefficient of metals implies a small Hall field and that the Hall field is the tangential component of the electric

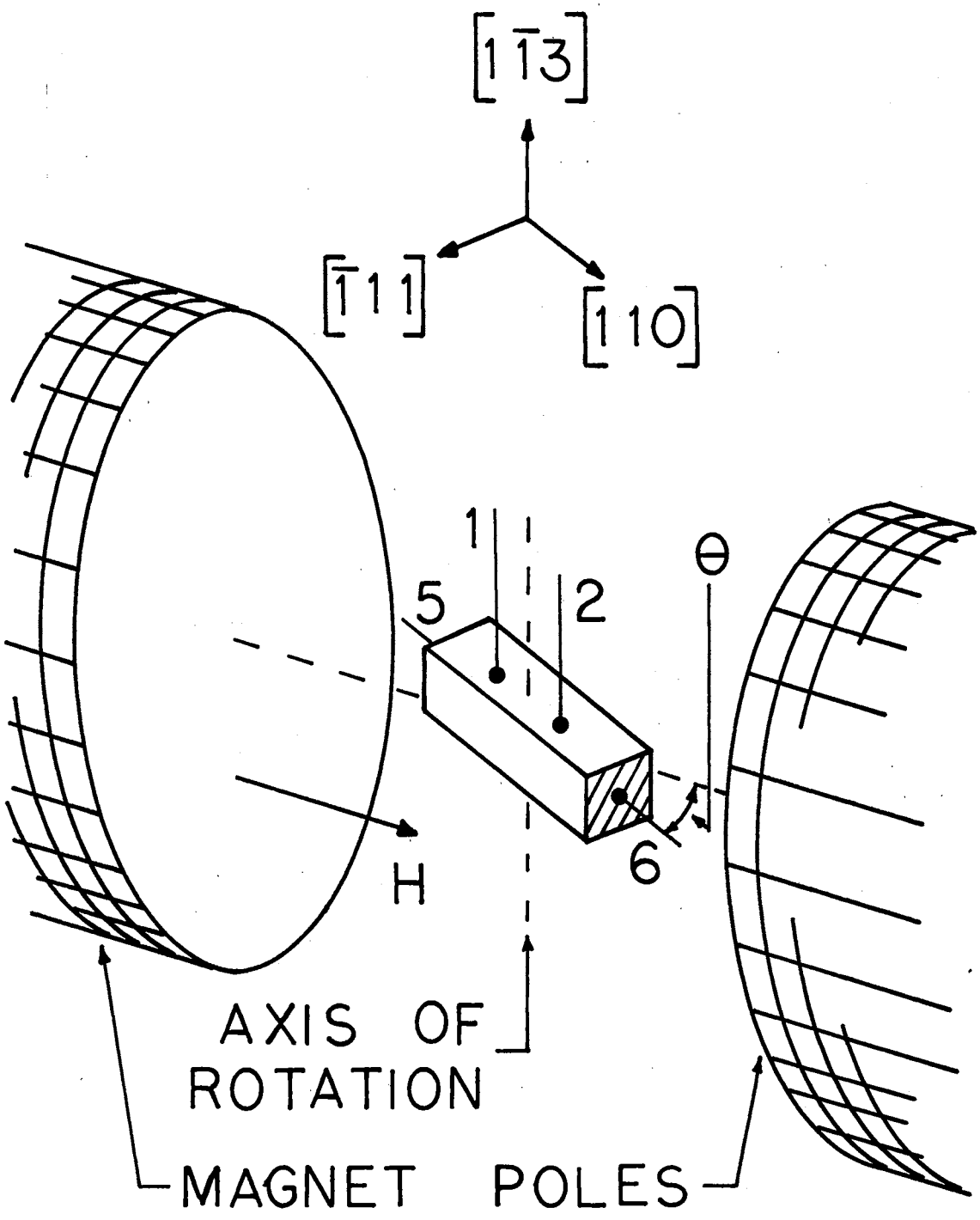

Figure 2. Experimental Arrangement to Measure Magnetoresistance as a Function of Angle θ

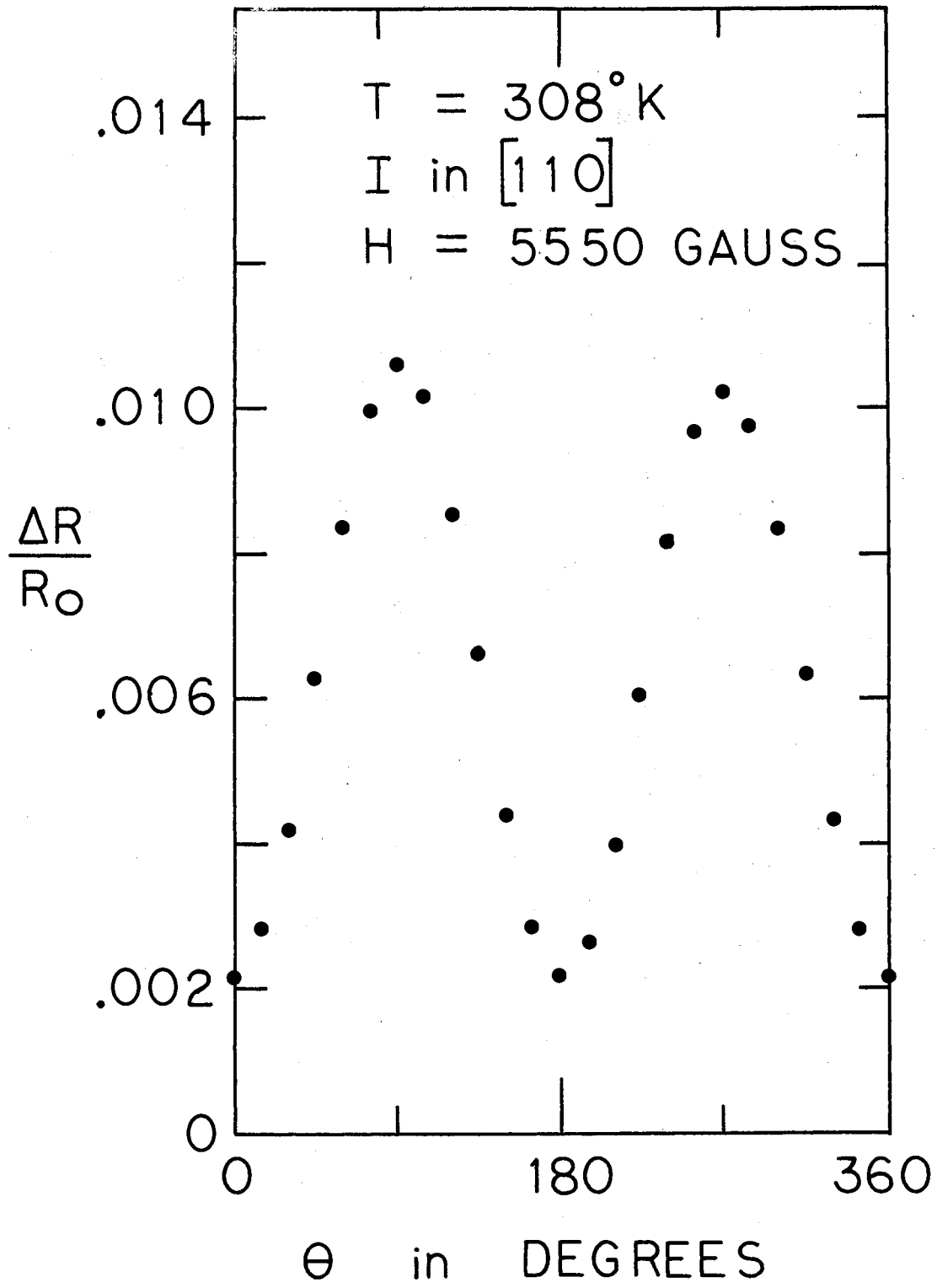

Figure 3. Magnetoresistance of DS-2 as a Function of Angle θ

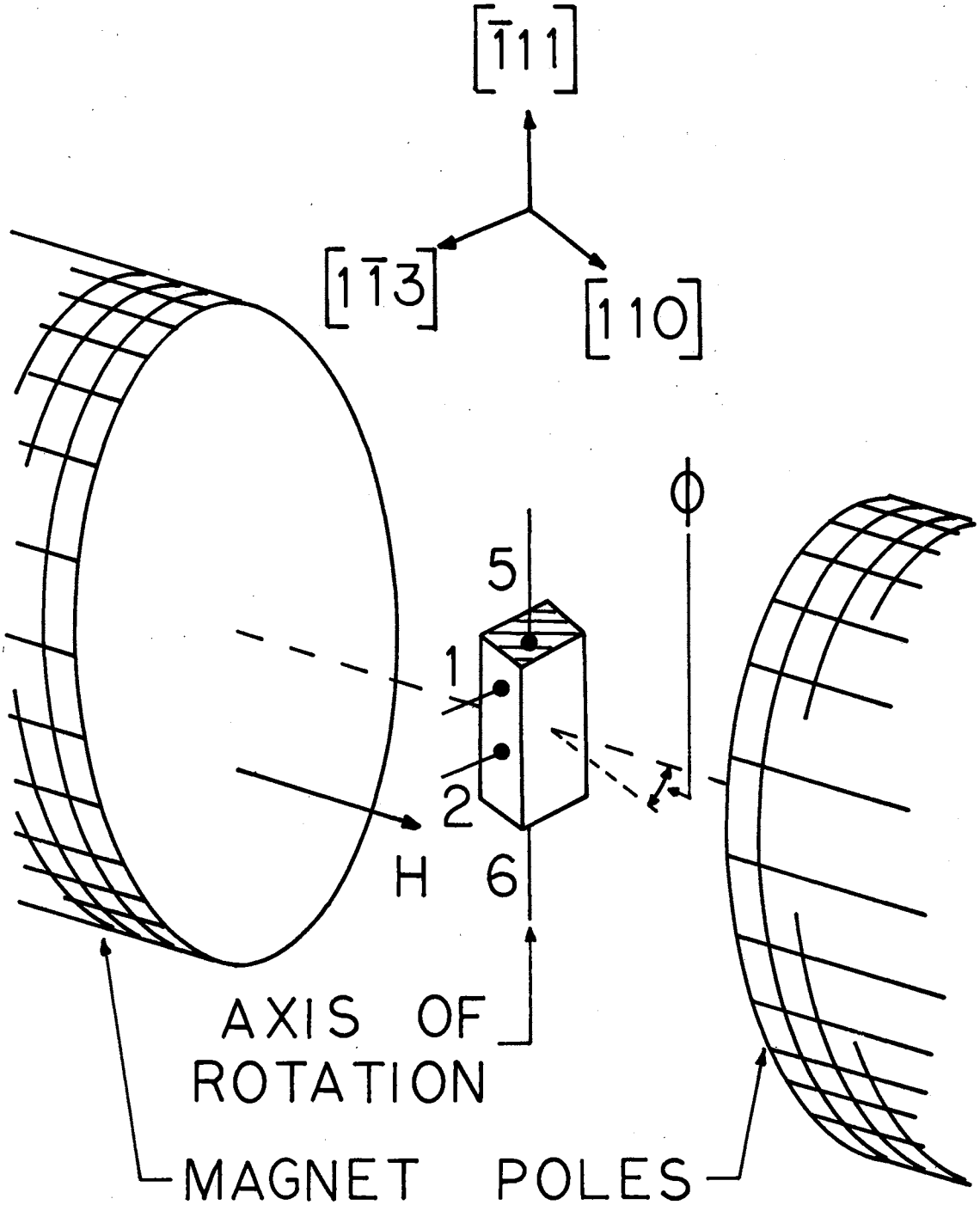

Figure 4. Experimental Arrangement to Measure Magnetoresistance as a Function of Angle ϕ

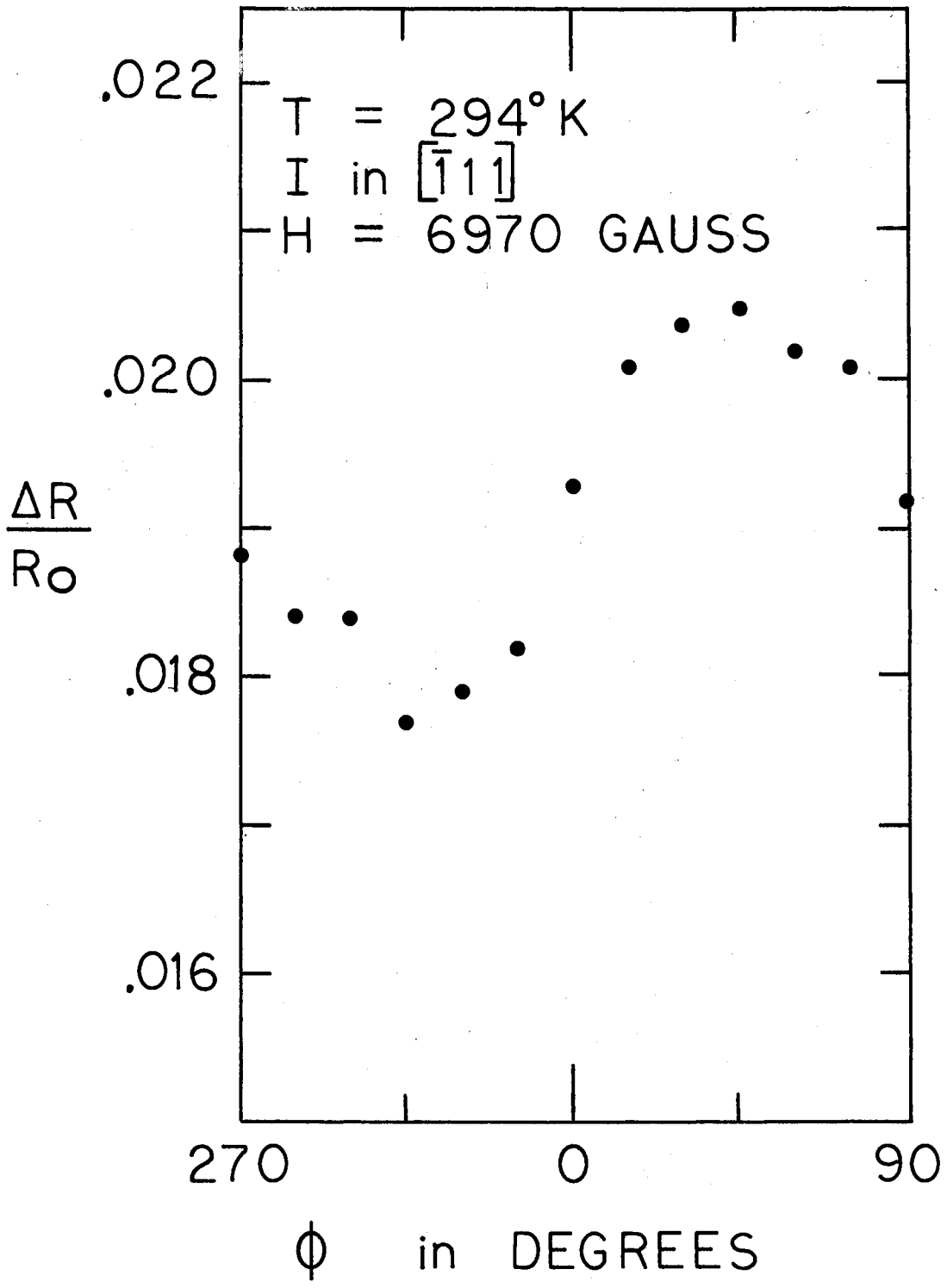

Figure 5. Magnetoresistance of DS-2 as a Function of Angle ϕ

field which is continuous across the metal-semiconductor boundary. In a magnetic field, the lines of current flow are rotated through the Hall angle $\theta_H/2$ relative to the electric field. Thus, the electric current density vector in front of the current electrodes will not be perpendicular to the plane of the current contacts. Along the longitudinal edges of the semiconductor, the current density will be essentially longitudinally directed if the impedances of the measuring instruments (not shown in Figure 6) are large.

Due to the shorting effect of the current electrodes, the voltage measured by the probe contacts #3 and #4 in Figure 6 will be largest near the center of the sample between the current electrodes, will diminish as the current electrodes are approached, and will vanish in the region in front of the current contacts. The length of the semiconductor plate must be much greater than the width and the probe contacts #3 and #4 must be far enough away from the current contacts in order that the voltage which is recorded closely approximate the Hall voltage. Likewise, the shorting of the Hall field in the vicinity of the current electrodes allows the charge carriers in this region to be more influenced by the deflecting force of the magnetic field. The result is a smaller component of the drift velocity in the longitudinal direction; the measurement of the magnetoresistance using probe contacts #1 and #2 in Figure 6 in this region of the sample will be larger than that measured near the center of the sample between the current contacts.

When measuring the resistance of the material with and without a magnetic field, the lines of current flow should be parallel to the measured component of the electric field. Probe contacts #1 and #2 should be placed such as to avoid the regions in the vicinity of the

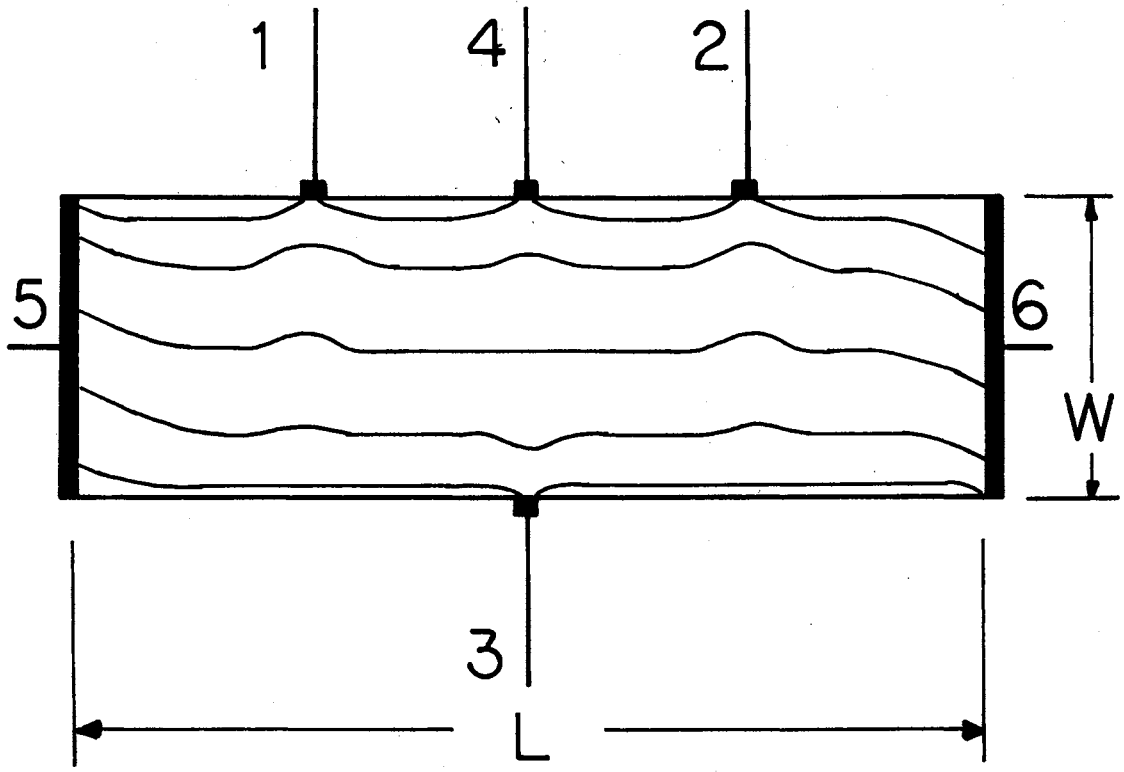

Figure 6. Flow Lines of Current in a Semiconductor Plate in a Magnetic Field

The magnetic field is normal to the cross section.

current electrodes where the current density is not parallel to the longitudinal direction. To do this, each probe contact should be placed at least a distance of 2W from each current contact, and that L/W should be greater than 10. The experimental evidence upon which this rule of thumb is based is presented in an article written by H. Weiss (22).

An article which takes into account both the size and position of the electrical contacts on the galvanomagnetic properties of homogeneous materials was written by R. Wick (23). To illustrate his suggestions, based on the method of conformal mapping, consider the cross section of the semiconductor shown in the insert of Figure 7. The magnetic field is perpendicular to the plane of the drawing, and the probe contacts have been idealized as mathematical points. The dimensions of the cross section as well as the positions of the probe contacts were used in obtaining some of the data reported in Chapter IV for the electric current along the $[\bar{1}11]$ axis and the magnetic field along the $[1\bar{1}0]$ axis.

If Z_{MR} is the impedance which is measured between the probe contacts when the magnetic field has an intensity H and if Z_0 is the corresponding experimentally determined impedance without the magnetic field, then the ratio Z_{MR}/Z_0 can be shown to be given by

$$\frac{Z_{MR}}{Z_0} = \left(\frac{\rho}{\rho_0}\right)\frac{6.171}{\cos(0.5\ell\pi)}\left\{\int_{-7.5}^{7.5}\left(\frac{1-\tanh\theta}{1.965-\tanh\theta}\right)^{\frac{1}{2}(1+\ell)}\left(\frac{1+\tanh\theta}{1.965+\tanh\theta}\right)^{\frac{1}{2}(1-\ell)}d\theta\right\}^{-1} \times$$

$$\left\{\int_{1.19}^{1.76}\frac{\tanh^{(2-\ell)}\theta\ d\theta}{\sinh^{(1-\ell)}\theta\left[(1.965\tanh^2\theta-1)(\tanh^2\theta+1)\right]^{\frac{1}{2}(1-\ell)}(1.965\tanh^2\theta+1)^{\frac{1}{2}(1+\ell)}} + \right.$$

$$\left. + \int_{1.19}^{1.76}\frac{\tanh^{(2+\ell)}\theta\ d\theta}{\sinh^{(1+\ell)}\theta\left[(1.965\tanh^2\theta-1)(\tanh^2\theta+1)\right]^{\frac{1}{2}(1+\ell)}(1.965\tanh^2\theta+1)^{\frac{1}{2}(1-\ell)}}\right\}. \quad (3)$$

The quantities ρ and ρ_0 are the true resisitivities (as measured on long rod-like specimens) of the material with and without the magnetic field. The numerical constants in the integrand and the limits of the integrals depend on the dimensions of the semiconductor listed in Figure 7. The quantity $\ell\pi/2$ is the Hall angle and satisfies the relation

$$\tan(\ell\pi/2) = \frac{R_H H}{\rho} ,$$

where R_H is the Hall coefficient of the material in the magnetic field H (as measured on a long rod-like specimen). If the Hall coefficient of the material is known as a function of the magnetic field, it is possible to find the resistivity ratio ρ/ρ_0 by using equation (3). The integrals on the right hand side of equation (3) were numerically evaluated for selected values of the quantity ℓ; a plot of the ratio $Z_{MR}\rho_0/Z_0\rho$ as a function of the Hall angle is shown in Figure 7. It is easily seen that the increase of the resistance of a specimen due to the geometry is large if the mobility of the carriers in the material is large and/or if the measurements are made in large magnetic fields.

The influence of the geometry on the magnetoresistance of a rectangular plate has been calculated by H. J. Lippmann and F. Kuhrt (24). A plot of the ratio $Z_{MR}\rho_0/Z_0\rho$ as a function of the tangent of the Hall angle is presented for representative values of the parameter L/W. Applying their results to the specimen cross section shown in the insert in Figure 7 indicates that the ratio $Z_{MR}\rho_0/Z_0\rho$ is roughly twice as large as the numerical values calculated by the author and given in Figure 7. The reason for the difference in the calculations has not been investigated. H. J. Lippmann and F. Kuhrt (25) have also calculated the influence of the geometry on the Hall effect of a rectangular plate. Their results indicate that the measured Hall

coefficient will increase with increasing magnetic field; this effect is more pronounced when the quantity L/W is less than unity. Thus, if the dependence of the Hall coefficient on the magnetic field is to be measured, specimens with large values of L/W must be used in order that the geometrically produced increase in the Hall coefficient with increasing magnetic field is negligible.

Equation (3) was derived by adding the potential difference between the probe contacts for the case of the magnetic field directed out of the plane of Figure 7 to the potential difference between the probe contacts for the case of the magnetic field directed down into the plane of Figure 7. If these two potential differences are subtracted from one another, the Hall coefficient can be determined. If $Z_H \tau/H$ is the measured Hall coefficient, it can be shown to be given by

$$\frac{Z_H \tau}{H} = \frac{\rho}{H \cos(0.5\ell\pi)} \left\{ \int_{-7.5}^{7.5} \left(\frac{1-\tanh\theta}{1.965-\tanh\theta} \right)^{\frac{1}{2}(1+\ell)} \left(\frac{1+\tanh\theta}{1.965+\tanh\theta} \right)^{\frac{1}{2}(1-\ell)} d\theta \right\}^{-1} \times$$

$$\left\{ \int_{1.19}^{7.5} \frac{\tanh^{(2-\ell)}\theta \; d\theta}{\sinh^{(1-\ell)}\theta \left[(1.965\tanh^2\theta - 1)(\tanh^2\theta + 1) \right]^{\frac{1}{2}(1-\ell)} (1.965\tanh^2\theta + 1)^{\frac{1}{2}(1+\ell)}} + \right.$$

$$+ \int_{1.76}^{7.5} \frac{\tanh^{(2-\ell)}\theta \; d\theta}{\sinh^{(1-\ell)}\theta \left[(1.965\tanh^2\theta - 1)(\tanh^2\theta + 1) \right]^{\frac{1}{2}(1-\ell)} (1.965\tanh^2\theta + 1)^{\frac{1}{2}(1+\ell)}} +$$

$$- \int_{1.76}^{7.5} \frac{\tanh^{(2+\ell)}\theta \; d\theta}{\sinh^{(1+\ell)}\theta \left[(1.965\tanh^2\theta - 1)(\tanh^2\theta + 1) \right]^{\frac{1}{2}(1+\ell)} (1.965\tanh^2\theta + 1)^{\frac{1}{2}(1-\ell)}} +$$

$$\left. - \int_{1.19}^{7.5} \frac{\tanh^{(2+\ell)}\theta \; d\theta}{\sinh^{(1+\ell)}\theta \left[(1.965\tanh^2\theta - 1)(\tanh^2\theta + 1) \right]^{\frac{1}{2}(1+\ell)} (1.965\tanh^2\theta + 1)^{\frac{1}{2}(1-\ell)}} \right\}. \quad (4)$$

As in equation (3), the numerical constants and limits of the integrals depend on the dimensions of the cross section of the specimen shown in Figure 7. At least in principle, it is possible to use the measured values of Z_{MR}, Z_0, $Z_H^{\mathcal{C}/H}$ and the computed value of ρ_o to determine the resistivity ρ and Hall coefficient R_H in a magnetic field H which satisfies both equations (3) and (4).

Inhomogeneity

If the lines of current flow in a semiconductor are not disturbed by the presence of a magnetic field and if the equipotential surfaces are rotated by the full Hall angle, the magnetoresistance of the semiconductor has its lowest value and the Hall coefficient has its largest value. Perturbations in the Hall field, such as due to the inhomogeneous distribution of impurities within a specimen, causes, in general, a change in the distribution and the direction of the lines of current flow in the semiconductor; a strong influence may be exerted on the galvanomagnetic voltages. Some comments highlighting three studies which have been made of the influence of inhomogeneities on galvanomagnetic measurements will be given. The subject is potentially broad, as shown by the examples to be discussed, because the nature of the inhomogeneities (size of aggregate in relation to the size of the crystal, orientation within the crystal, distribution throughout a region of the crystal) plays a decided role in the mathematical approach to the description of the effects they produce.

C. Herring (26) considered the effect of random inhomogeneities on the galvanomagnetic properties of materials where the size of the inhomogeneities is small compared to the size of the specimen but large

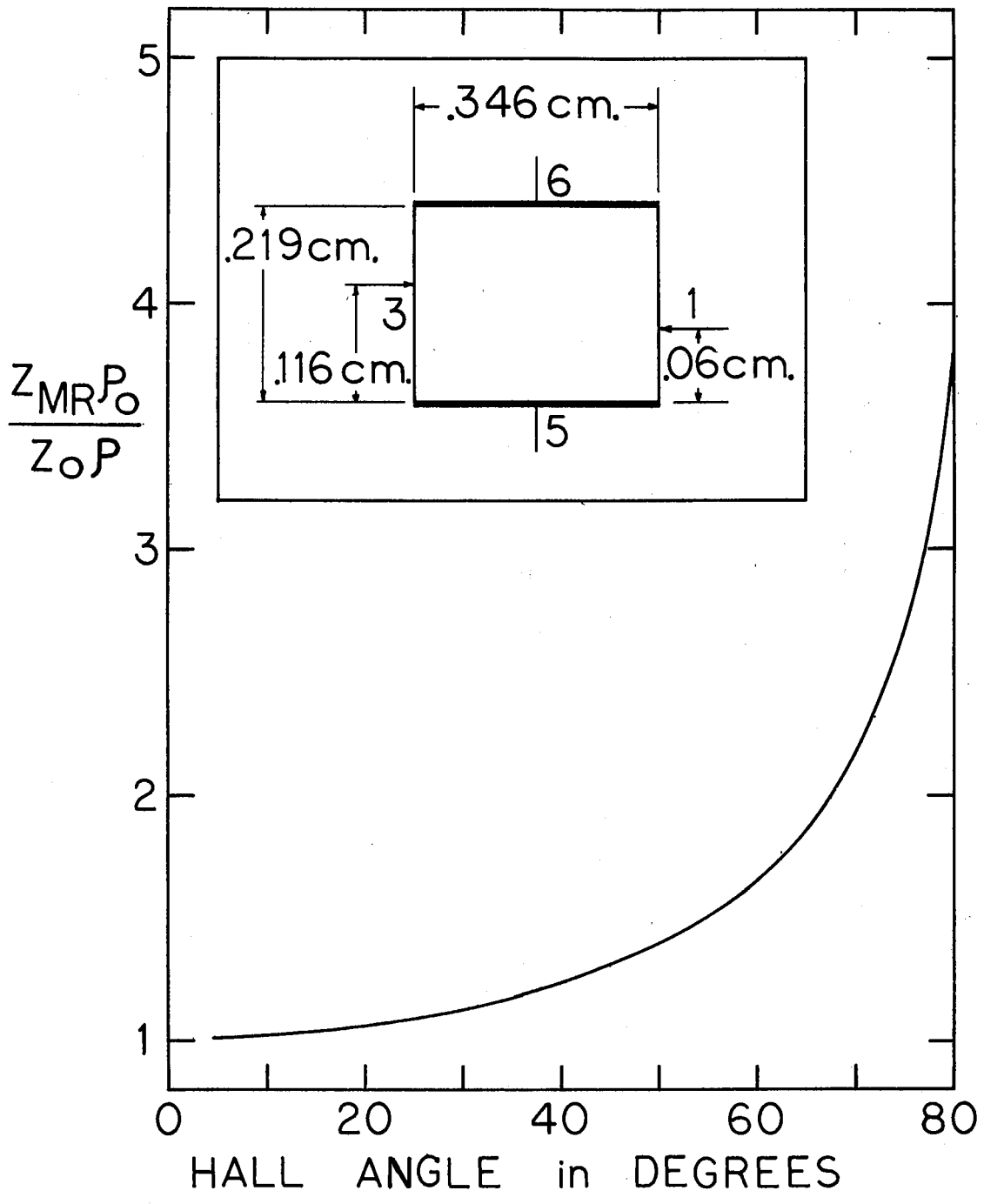

Figure 7. Geometrical Contribution to the Magnetoresistance

compared to a suitably defined mean free path of the charge carriers. If the inhomogeneities in the sample gives rise to only a fluctuation in the density of the charge carriers, the measured Hall coefficient in the limit of vanishing magnetic field $R_{eff}(0)$ is shown to satisfy the relation

$$R_{eff}(0) = \frac{\left(\frac{\mu_H}{\mu}\right)}{\langle p \rangle ec} .$$

The angular bracketed term is the spatial average of the carrier density; μ_H and μ are the Hall and drift mobilities of the carriers. This relation is of the same form as previously given for a homogeneous material in the weak-field region with the substitution of the spatial average of the charge density $\langle p \rangle$ for the uniform charge density p. In the limit of large magnetic fields and when the local magnetoresistance saturates, the measured Hall coefficient saturates approximately to the spatial average of the local saturation value of the Hall coefficient. In the limit of an isotropic fluctuation in the carrier density, but not in the mobility, the observed magnetoresistance in the limit of weak magnetic fields indicates an intermixing of the transverse and longitudinal magnetoresistance effects. Thus, a longitudinal magnetoresistance may be observed in a material due to only the inhomogeneities of the impurities in the material. In the limit of strong magnetic fields, the transverse magnetoresistance is a sensitive function of the directional distribution in the fluctuations in the carrier density. For a statistically isotropic fluctuation in p, the transverse magnetoresistance does not saturate and linearly increases with increasing magnetic field. On the other hand, if the fluctuations in p are limited to the directions perpendicular to the

direction of the magnetic field, the transverse magnetoresistance will vary as the square of the magnetic field.

The effect of a longitudinal gradient in the carrier concentration on the transverse magnetoresistance of an infinitely long rod has been evaluated by R. T. Bate and A. C. Beer (27). For the sake of mathematical simplicity, the carrier density was assumed to be exponentially dependent only on the x-direction (longitudinal direction). Only for this special case will there be no transverse currents in the y- and z-directions in the sample. The results are best explained with the help of Figure 8, which is taken from an article written by H. Weiss (28). Without a magnetic field, the current density is uniform across the sample; with a magnetic field, the current density is dependent on the y-direction and on the strength of the magnetic field. The increased spacing between the equipotential lines in the +x-direction is the result of a decreasing density of carriers in that direction. A magnetic field H (labeled as "B" in the article by H. Weiss (28)), directed outward from the plane of the drawing, deflects the positive charge carriers in the -y-direction. It is seen that the lower half of the semiconductor carries a larger current (as represented by the decreased spacing between the lines of current flow) than the upper half. Due to the shift in the distribution of current, the potential difference between probe contacts #3 and #4 will decrease as the magnetic field is turned on while the change in the potential difference between probe contacts #1 and #2 will increase. Upon reversing the direction of the magnetic field, the upper half of the semiconductor will carry the larger share of the current, and the changes in the potential difference between the two pairs of probe contact will be interchanged.

The average change in the potential difference will, however, give a positive magnetoresistance. This is not true if the probe contacts are placed at the center of the surface perpendicular to the direction of the magnetic field (marked by the symbol X in Figure 8). For both directions of the magnetic field, the change in the potential difference between the probe contacts will be negative, and a negative magnetoresistance would be recorded.

R. T. Bate, J. C. Bell, and A. C. Beer (29) have considered the case of a single planar discontinuity in the resistivity and Hall coefficient in the current direction between two long uniform parallelepipeds. This case is illustrated in Figure 9; the cross section of the sample to the left of the dashed line (speckled) has the higher concentration of charge carriers, lower resistivity and smaller Hall coefficient. Part (a) of Figure 9 illustrates the current density and electric field vectors for the case of no magnetic field; part (b) illustrates the same vectors for the case of a magnetic field directed perpendicular to the plane of the drawing. If the mobility of the carriers is independent of the concentration of impurities in the material, then the equipotential surfaces of both homogeneous sections of the sample will be rotated through the Hall angle Θ relative to their positions in the absence of a magnetic field. However, this violates the continuity of the tangential component of the electric field across the discontinuity boundary. To satisfy $\nabla \times \vec{E} = 0$, the lines of current flow in the left hand section of the parallelepiped must be rotated upwards through the angle ϕ while those in the right hand section must be rotated downwards through the same angle ϕ. The resulting tangential component of the electric field which is

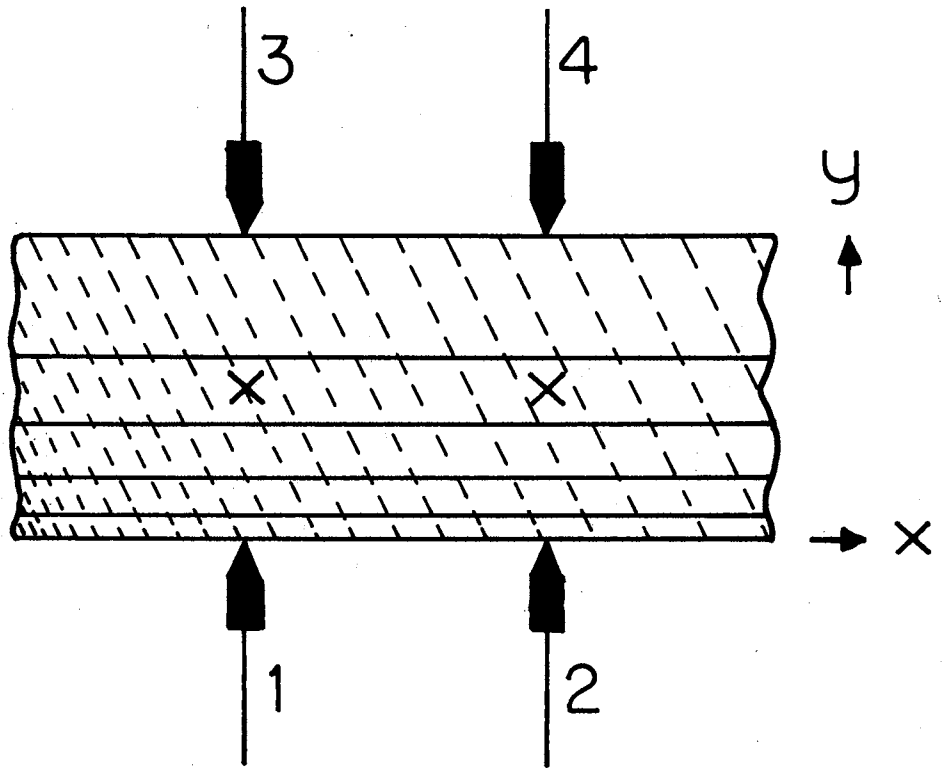

Source: H. Weiss, "Magnetoresistance," Semiconductors and Semimetals, Eds. R. F. Willardson and A. C. Beer. (Academic Press, New York, 1966), Vol. 1, Chap. 10, p. 315.

Figure 8. Equipotential Lines (--) and Current Lines (—) in the Magnetic Field in a Small Rod with a Constant Relative Impurity Gradient in the Length Direction

The magnetic field is normal to the cross section.

continuous across the boundary is labeled $\vec{E}'_H$. In the two sections, there will be oppositely directed current densities directed along the y-axis. The net current density in the y-direction will vanish. This means that in the section of the parallelepiped with the higher density of charge carriers the electric field will be rotated through more than the Hall angle as compared to a homogeneous specimen. Likewise, the longitudinal component of the electric field will be smaller than that for a homogeneous specimen. The right hand section with the smaller density of charge carriers can be similarily analyzed to show that the electric field is rotated through less than the Hall angle and its component in the longitudinal direction is larger than that for a completely homogeneous sample. If the Hall voltage is measured at the boundary between the sections, the result will be an intermixing of Hall coefficients and magnetoresistance effects. The contributions of the inhomogeneity to the magnetoresistance will depend on the location of the probe contacts on the parallelepiped and may be positive or negative.

Sample Resistivity and Time Varying Magnetic Fields

The resistivity of the diamond DS-2 varies markedly with temperature as shown in Figure 10. When electrical measurements are made at room temperature, using a steady field electromagnet, temperature excursions of $\pm$ 0.05°K are the limits of tolerance. It is estimated from Figure 10 that the uncertainity in the zero field resistivity due to a temperature excursion of 0.05°K at 308°K is 0.2% of ρ_0. In the case of pulsed magnetic fields, temperature excursions

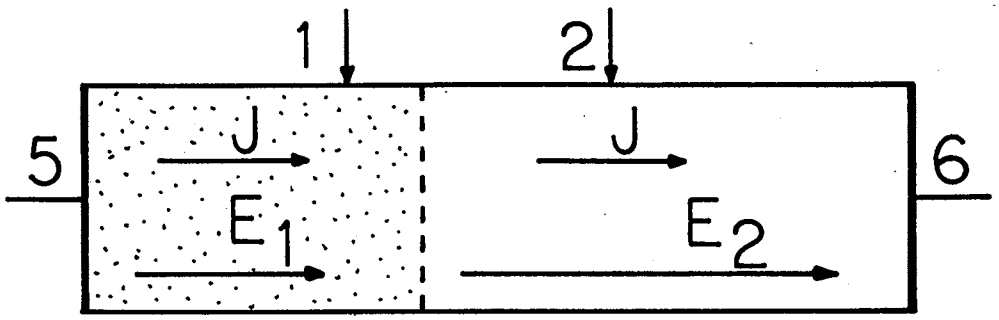

(a) Current Density and Electric Field Vectors in Absence of a Magnetic Field

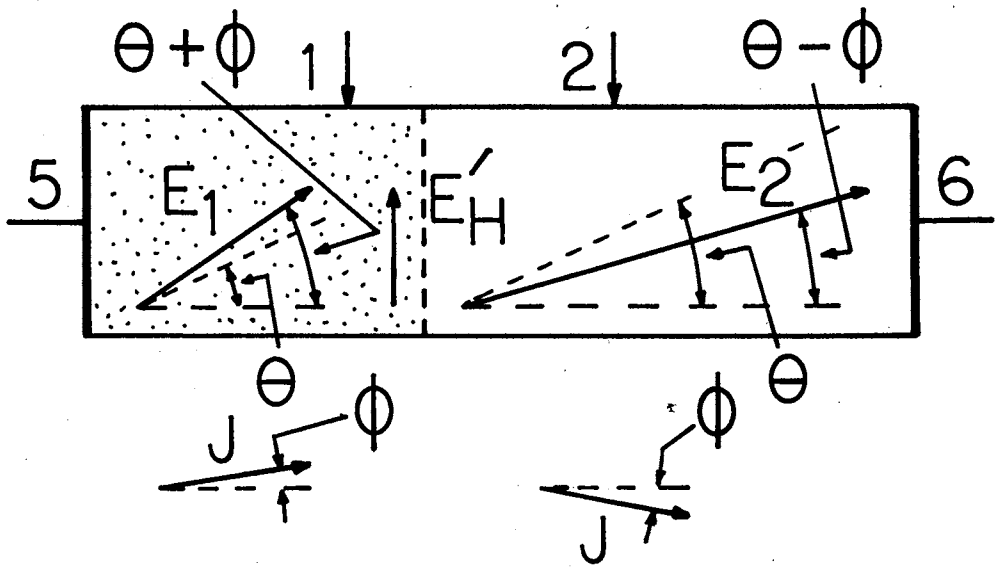

(b) Rotation of Current Density and Electric Field Vectors to Satisfy the Relation $\nabla \times \vec{E} = 0$

Figure 9. Single Planar Discontinuity between Two Specimens of a Material with Different Charge Carrier Concentrations

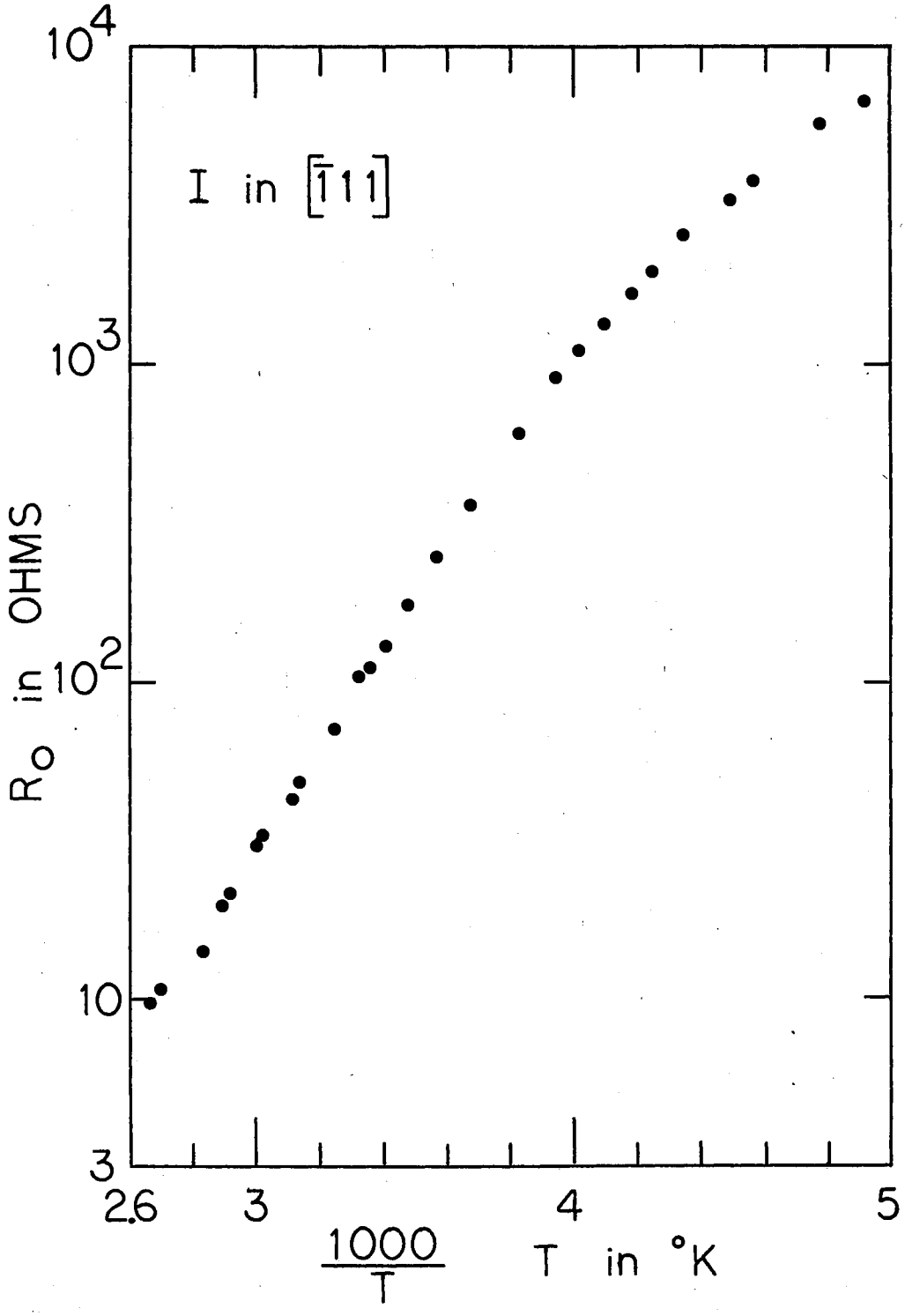

Figure 10. Resistance of the Blue End of DS-2 as a Function of Temperature

during the measurement may be small due to the quickness of the measurement. However, the initial temperature of the diamond will be unknown due to a time lag between preparing the pulsed magnet system for use and the completion of the magnetic field production.

The steady dc current through the sample should be small enough so that Joule heating is negligible. This was checked by measuring the magnetoresistance of the diamond as a function of sample current. The magnetoresistance was found to be linearly dependent on the current for sample currents of 100 microamperes to 25 milliamperes. Likewise, the resistance of the diamond satisfied Ohm's law for these currents. For both the magnetoresistance and Hall effect measurements at 308^{o}K, a steady current of 3 milliamperes was used. For experimental runs at 436^{o}K, steady currents were chosen such as not to exceed a power input of 1 milliwatt (just as at 308^{o}K).

During the presence of a time varying magnetic field, an electromotive force (abbreviated emf) is induced in the lead wires and the diamond. All lead wires were twisted and the bare gold wires attached to the electrical contacts on the diamond were placed next to one another so as to reduce the area exposed to the pulsed field. A brute force technique for reducing the size of the induced emf relative to the voltage associated with the magnetoresistance is accomplished by increasing the size of the electric current in the diamond specimen. From equation (1), it is seen that the change in the potential difference between the magnetoresistance contacts ΔV for a given magnetoresistance $\Delta\rho/\rho_o$ is linearly dependent on the initial potential difference V_0. For this reason, a continuous current of 3 milliamperes, applied by a method described in Chapter III, was chosen for the

galvanomagnetic measurements at 308°K.

Another technique of reducing the effect of the induced emf was developed when measuring the galvanomagnetic effects of p-type germanium in 460 kilo-oersted magnetic fields. A simplified schematic of the circuit is shown in Figure 11. The sample is placed in the bore of an electromagnet (not shown in Figure 11). The constant current power supply, labeled B, was modulated with a single square wave pulse in synchronous with the production of the magnetic field. This allowed large currents to flow in the germanium sample for short periods of time, and thereby increase ΔV without appreciable heating effects. Also, a portion of the emf induced in the single turn coil L was connected in series with one of the magnetoresistance contacts. The variable resistor R was adjusted so that the opposing voltage generated in the coil L nearly canceled the emf induced in the probe contact wires. The coil L was concentric with the germanium sample within the bore of the electromagnet.

Separation Techniques for Electrical Measurements

The magnetoresistance is an odd function of the electric current because the sign of the voltage between the probe contacts #1 and #2 in Figure 1 changes upon reversal of the current in the sample. It is an even function of the magnetic field because the sign of the voltage does not change upon reversal of the magnetic field. A similar analysis reveals that the Hall voltage is an odd function of both the electrical current and the magnetic field. By making electrical measurements for four combinations of electric current and magnetic field directions, the magnetoresistance and Hall effect can be separated from one another.

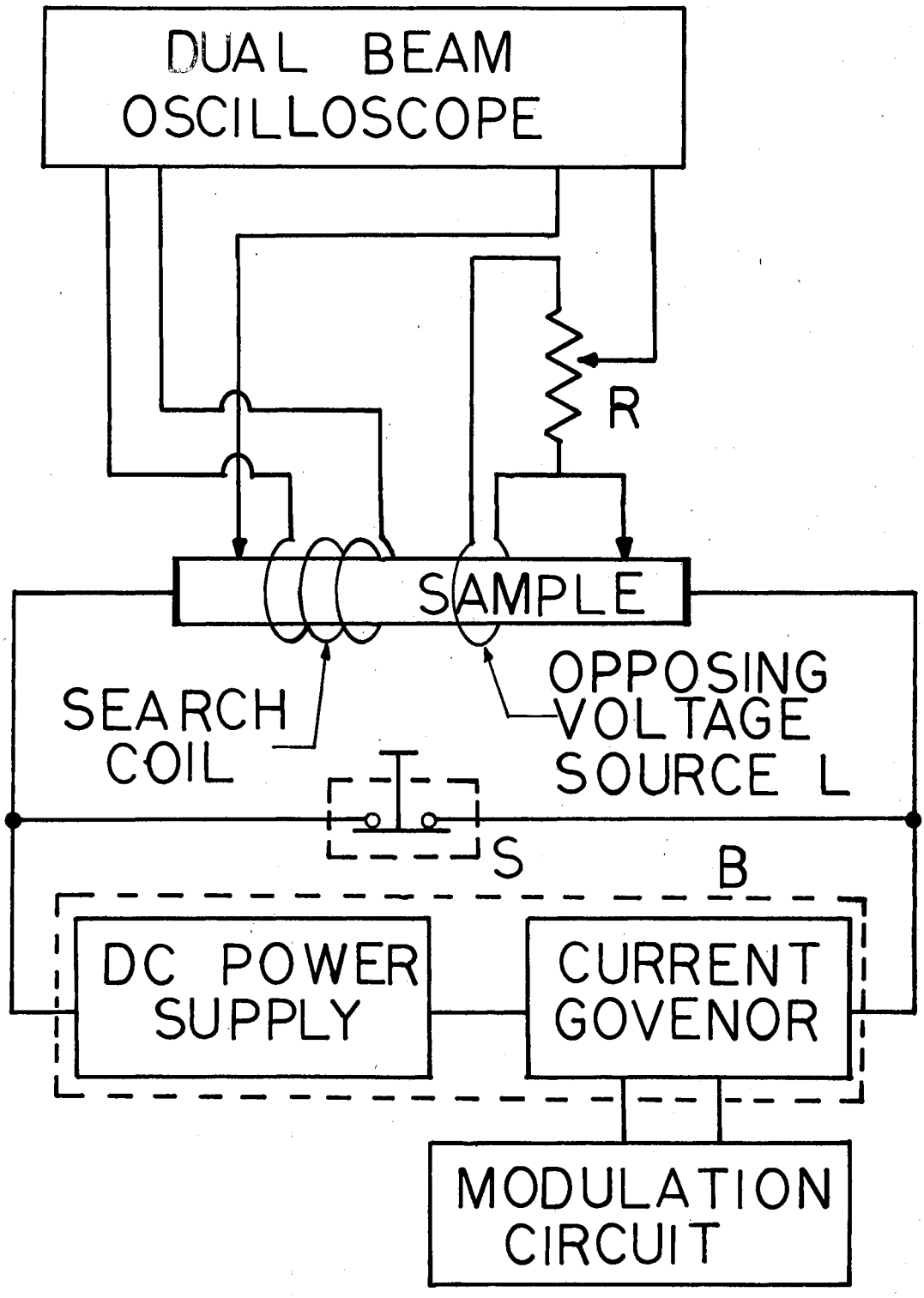

Figure 11. Simplified Circuit to Decrease the Effect of an Induced Electromotive Force

The sample is located in a pulsed magnetic field.

The analysis requires the use of ten subscripted variables. Let "FI" stand for "forward current", "RI" for "reverse current", "FH" for "forward magnetic field", "RH" for "reverse magnetic field", "OI" for "odd function of the current", "EI" for "even function of the current", "OH" for "Odd function of the magnetic field", and finally, "EH" for "even function of the magnetic field". Next, let E^0_{FI} be the potential difference between the magnetoresistance probe contacts when the sample carries a forward current in zero magnetic field. Define E_{FIFH} as the potential difference between the magnetoresistance probe contacts when the sample carries a forward current in a forward magnetic field. And, finally, let V_{EIEH} be the change in the potential difference between the magnetoresistance contacts which is an even function of the current and an even function of the magnetic field. Similar to the above, the quantities E_{RIFH}, E_{FIRH}, E_{RIRH}, E^0_{RI}, V_{EIOH}, V_{OIEH}, and V_{OIOH} are defined. Note that the two directions of sample current have been labeled "forward" and "reverse" and similarily for the magnetic field. These are just labels and should not be construed to imply, for example, that in the "forward" direction, the magnetic field and the current density are pointing in the same direction. It can be shown that the voltage associated with the magnetoresistance is given by

$$V_{OIEH} = \tfrac{1}{4}\left[E_{FIFH} + E_{FIRH} - E_{RIFH} - E_{RIRH} - 2E^0_{FI} + 2E^0_{RI}\right], \tag{5}$$

and that the magnetoresistance is

$$\frac{\Delta\rho}{\rho_0} = \frac{2V_{OIEH}}{E^0_{FI} - E^0_{RI}} . \tag{6}$$

A similar analysis for the Hall effects yields the Hall voltage

$$V_{OIOH} = \tfrac{1}{4}\left[E_{FIFH} - E_{FIRH} - E_{RIFH} + E_{RIRH}\right] , \tag{7}$$

and the Hall coefficient

$$R_H = \frac{V_{OIOH}\, T}{HI} . \tag{8}$$

There is an ambiguity in the sign of the Hall voltage as given by equation (7); the correct sign must be experimentally determined.

CHAPTER III

EXPERIMENTAL EQUIPMENT

The Capacitive Energy Storage System

Large, transient magnetic fields can be produced by discharging a bank of capacitors into an electromagnet. Such a capacitive energy storage system was designed and built by K. J Russell (30), formerly of this laboratory. Changes in that design have been confined to the sequence control equipment. The principal components of the system are shown in block diagram form in Figure 12. The capacitor bank is charged to the desired potential difference and then discharged through the discharge switch into the electromagnet. The charging and discharging sequence is controlled by the sequence control equipment. When the crowbar equipment is inoperative and while the discharge switch remains closed, the current in the magnet is a damped sinusoidal function of time. See the curve in part (a) of Figure 13. The crowbar equipment is designed to increase the life of both the capacitors and the pulse magnets. Activated by the sequence control equipment, the crowbar circuit is a low impedance path in parallel with the magnet. If the crowbar action is initiated at the peak magnetic field, the time variation of the current in the electromagnet is that shown in part (b) of Figure 13. However, during the measurement of the galvanomagnetic properties of diamond, the crowbar action was set to occur after the first half period of discharge. The magnetic field varied with time as

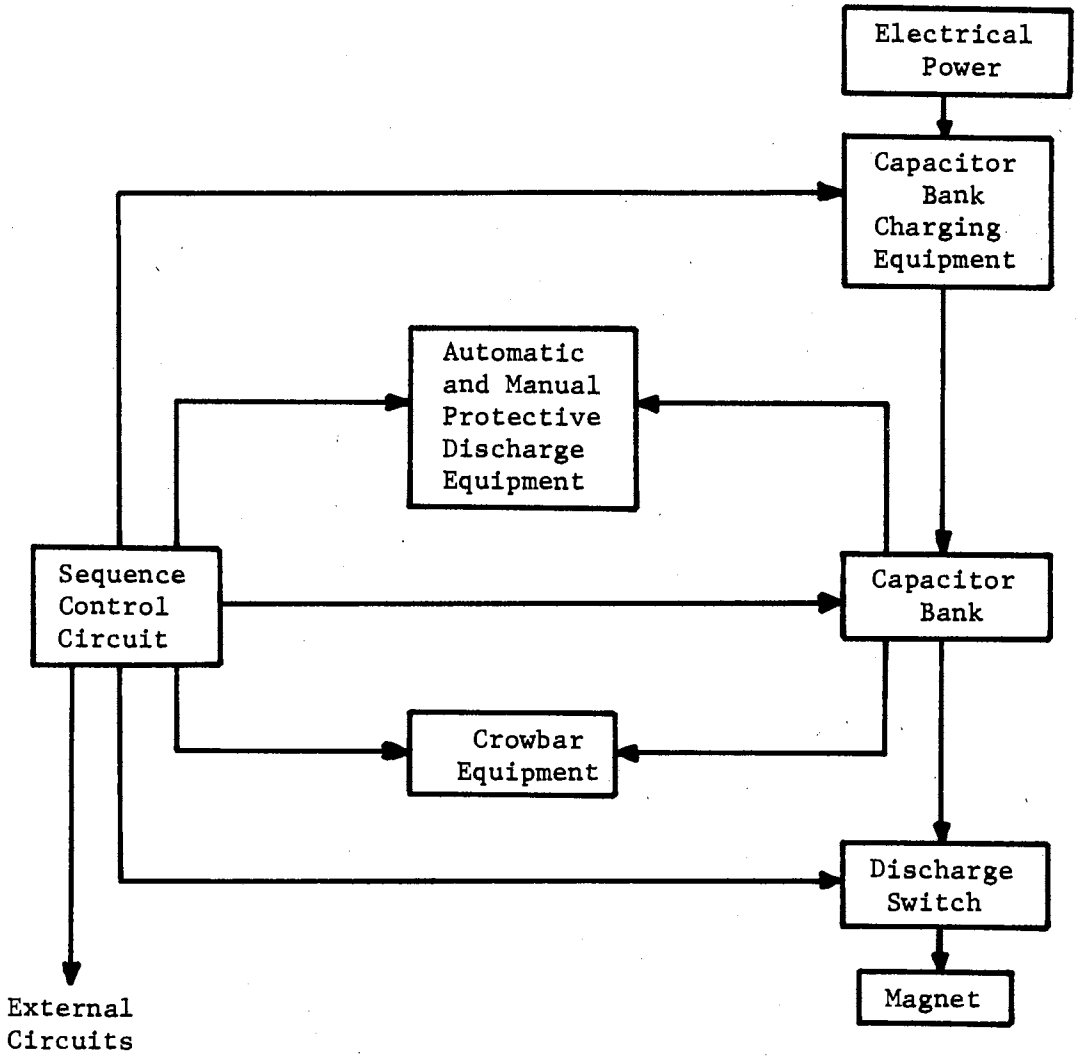

Figure 12. Capacitive Energy Storage System

shown in part (c) of Figure 13. In event of an emergency, the capacitor bank can be discharged into a set of power resistors composing the protective discharge equipment.

A block diagram of the sequence control equipment is shown in Figure 14. The sequence control switch and relay circuit controls the charging of the capacitor bank as well as the method of its discharge. The first method of discharge involves the modulation of circuits external to the capacitive energy storage system prior to and during the production of the magnetic field. This is accomplished by triggering the single shot pulse generator and current gate generator. The current gate output is a square wave of variable length; it was designed to modulate a constant current power supply used in the measurement of the galvanomagnetic effects. The bank discharge delay circuit is also triggered by the single shot generator. The delay is the length of time between the initiation of the modulating square wave and the initiation of the capacitor bank discharge. This delay allows the external circuits time to be properly functioning before the bank discharges. The pulse produced by the bank discharge delay circuit triggers the bank blocking oscillator, and sequentially, the crowbar delay circuit and crowbar blocking oscillator. The crowbar delay is the time between the initiation of the capacitor bank discharge and the initiation of the crowbar action; it is adjusted for the type of electromagnet used and the type of experiment being performed. The second method of discharging the capacitor bank does not involve the modulation of external circuits. The bank discharge delay circuit can be triggered directly by the sequence control switch and relay circuit. The bank voltage sensing circuit is used to manually or

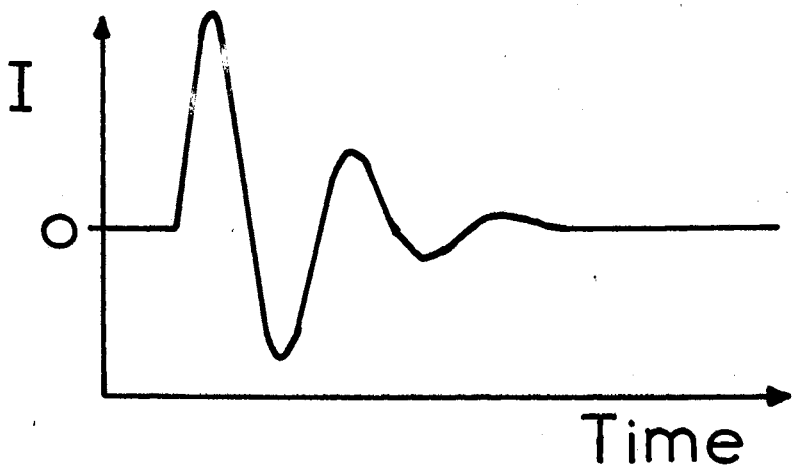

(a) Uncrowbarred Discharge.

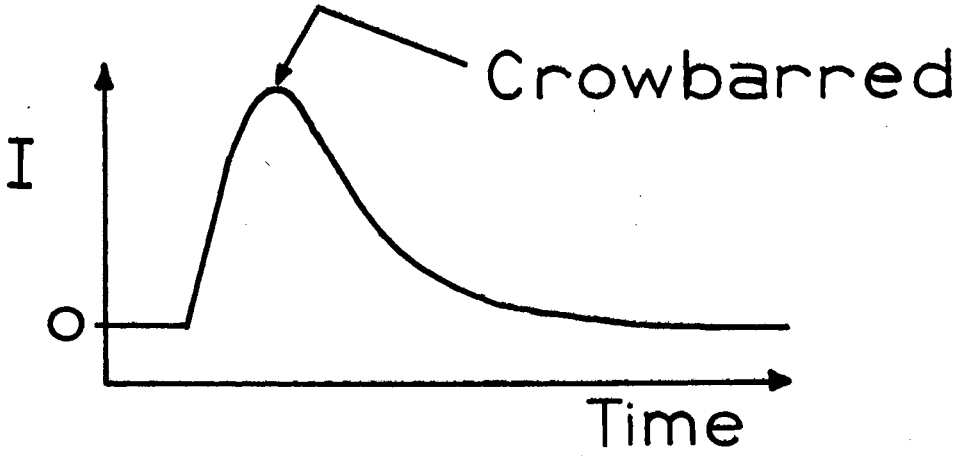

(b) Discharge Crowbarred at Peak Magnet Current.

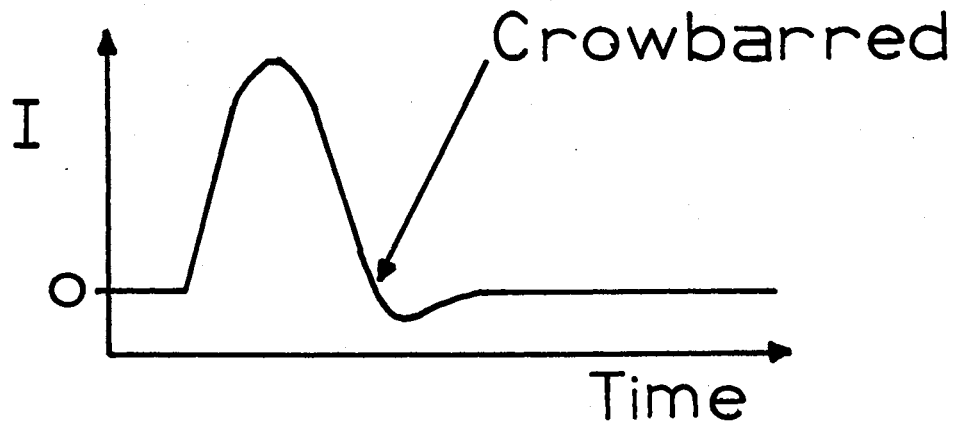

(c) Discharge Crowbarred at End of First Half-Period.

Figure 13. Magnet Current I versus Time.

automatically charge the bank to a desired voltage. The discharge of the capacitors into the power resistors composing the protective discharge equipment is controlled by the sequence control switch and relay circuit.

The details of the hardware in the capacitor bank (excluding the sequence control equipment) have been adequately described by K. J. Russell (30). Likewise, the detailed circuitry in the sequence control equipment have been described by the author in a manual now being used in conjunction with the operation of the pulse magnet system. It will be unnecessary to reproduce these circuit diagrams here.

The Electromagnet

The type of electromagnet used to produce the high magnetic fields is a multilayer coil of copper wire wound on an insulating mandral and reinforced against the destructive Lorentz force. The design of many types of electromagnets is given in a review written by D. B. Montgomery (31). The cross section of the magnet is shown in Figure 15. The insulating mandral (a) was machined out of a rod of linen based phenolic. Magnet wire (b) of square cross section and covered with a heavy insulating film was wound on the mandral. To increase the electrical insulation between each of the eight layers of wire, two layers of fiberglass cloth were wound over each layer of wire and kept in place with fiberglass filament tape. During the winding of a layer of wire, the outermost turns have a diameter slightly larger than the central turns. To achieve a more uniform diameter, narrow extra layers of fiberglass cloth had to be wrapped around the central portion of the fifth and sixth layers of wire. Fiberglass cloth (c) was also wrapped

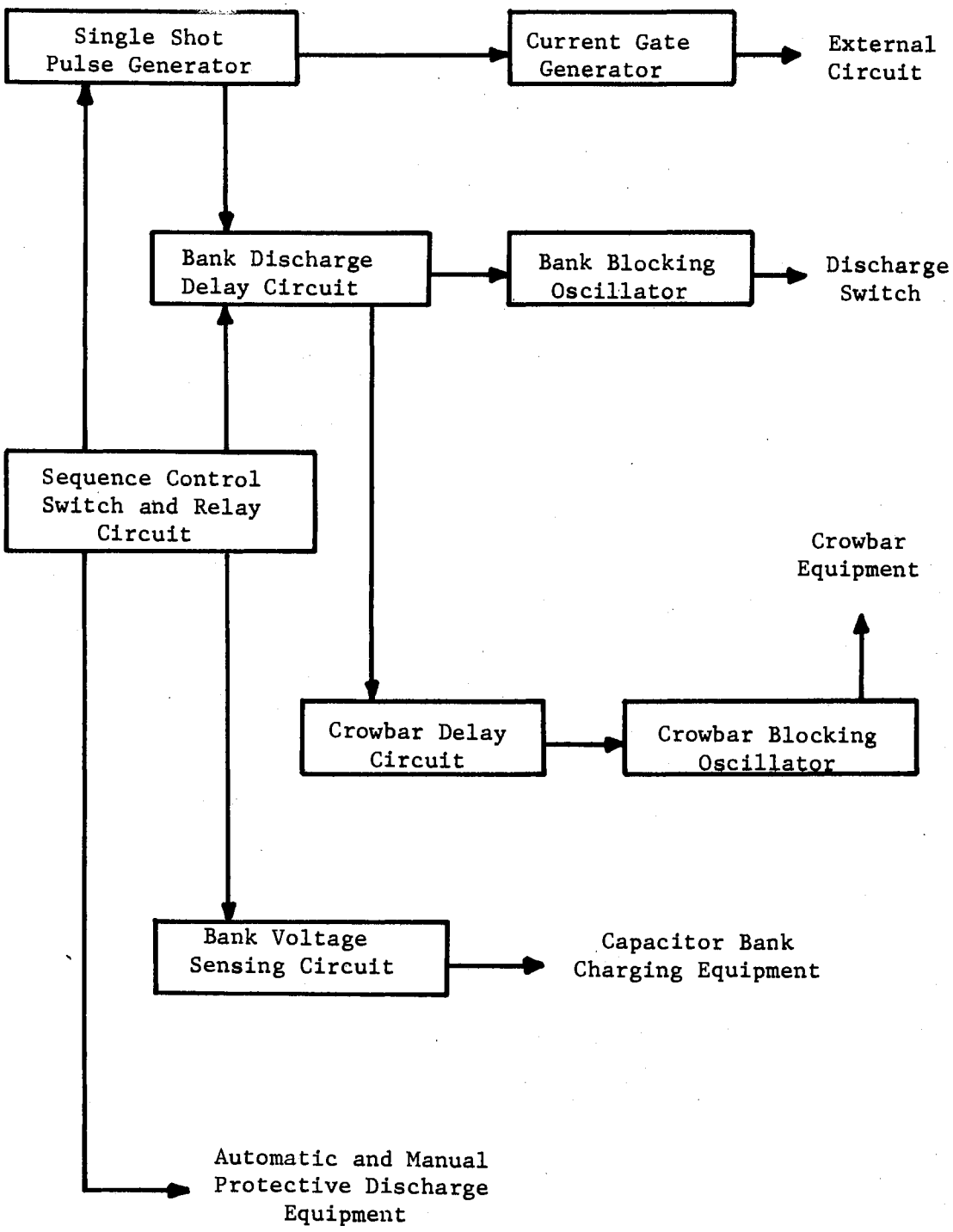

Figure 14. Sequence Control Circuit

around the eighth layer of wire to fill the space between the coil and the reinforcement shell composed of fiberglass tube (d) and a stainless steel tube (e). Both ends of the magnet wire were brought out through the same end plate of the insulating mandral and securely positioned between the two brass plates (f) forming each buss bar lead.

With the reinforcement shell epoxied into position, the magnet was heated to 100°C in vacuum for 24 hours. After cooling to room temperature, it was vacuum impregnated with an impregnating resin. The magnet was slipped into a phenolic plate (g); this plate was used to fasten the magnet to the collector plate of the capacitor bank. A phenolic insulating end plate (h) was placed over the buss bars. Two stainless steel end plates, (j) and (k), were rigidly held in place by four stainless steel bolts (m). A flexible strap (not shown) attached to each buss bar was bolted to the collector plate. The flexible leads allowed the magnetic field to be easily reversed.

Eight strands of asbestos cloth were symmetrically positioned around the bore of the magnet and epoxied into place. These strings provided a cushion between the variable temperature chamber (to be described later in this chapter) and the wall of the magnet. Water was used to cool the magnet during the experimental runs at 436°K. The water flowed through a copper tube (n) into a collecting chamber (p) and then down the bore of the magnet.

Typical parameters characterizing this type of electromagnet are summarized in Table II. Figure 16 is a photograph of the magnet.

Two helical solenoid magnets were constructed and used to measure the galvanomagnetic properties of several p-type germanium crystals in magnetic fields up to 460 kilogauss. The design of the magnets was

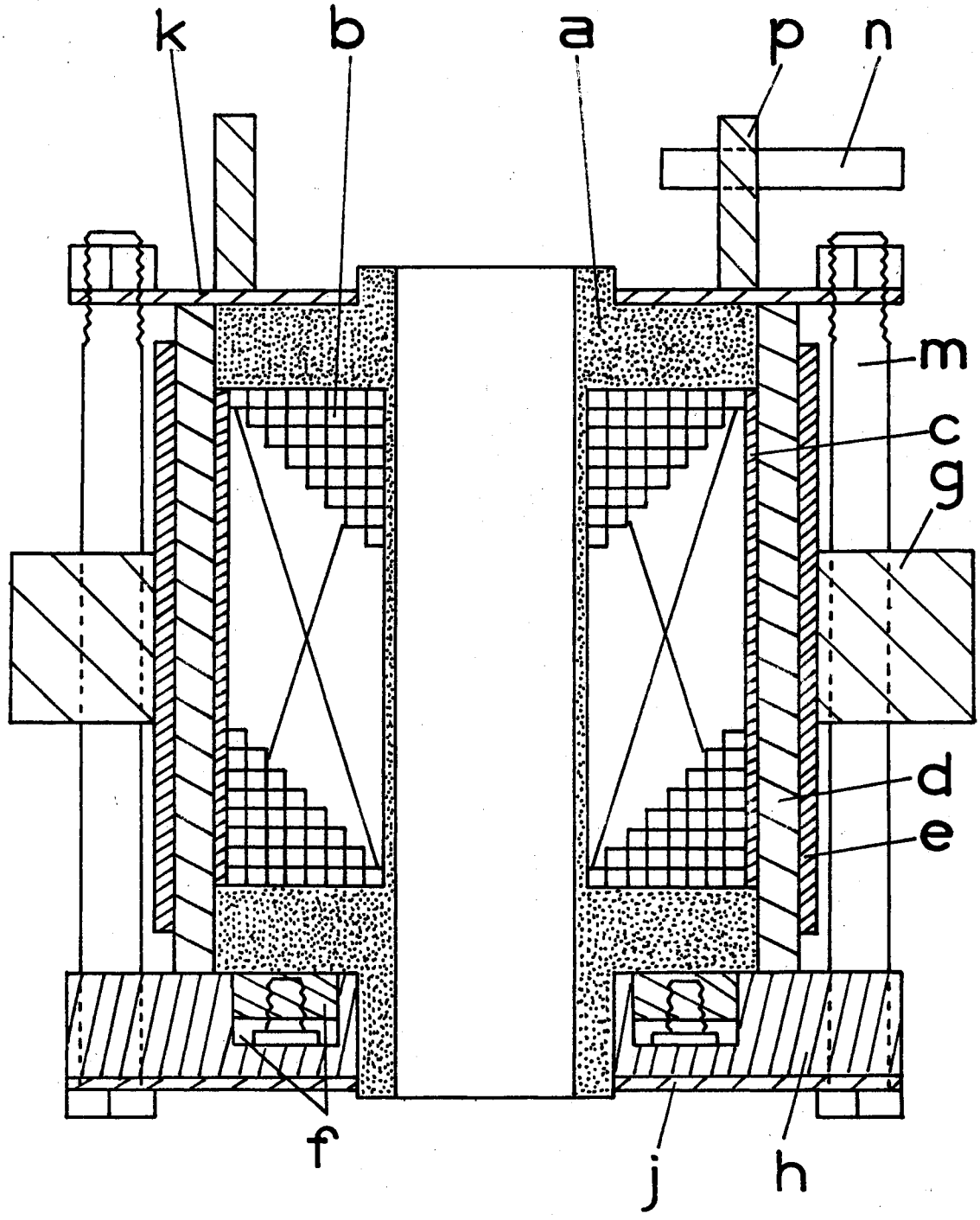

Figure 15. Cross Section of Wirewound Electromagnet

TABLE II

PARAMETERS CHARACTERIZING THE

WIREWOUND ELECTROMAGNET

Inside Diameter of Magnet Coil	3 cm.
Outside Diameter of Magnet Coil	8 cm.
Length of Coil	7.6 cm.
Number of Layers of Wire	8
Number of Turns per Layer	About 26½
Diameter of Magnet Bore	2.7 cm.
Magnet Coil Material	Magnet Wire; AWG Size 10; Square Cross Section; Film Coated.
Thickness of Fiberglass Insulation between Layers	About 0.04 cm.
DC Resistance of Magnet Coil	About 0.1 ohms
Inductance of Magnet Coil	About 0.9 millihenries
Half Period of Magnet	About 5 milliseconds
Peak Magnetic Field/Voltage of Capacitor Bank/Capacitance of Capacitor Bank	16.3 kilogauss/(kilovolt/millifarad)
Uniformity of Magnetic Field	Within Sphere of 1 cm. Diameter, Deviation from Maximum Magnetic Field is ½%

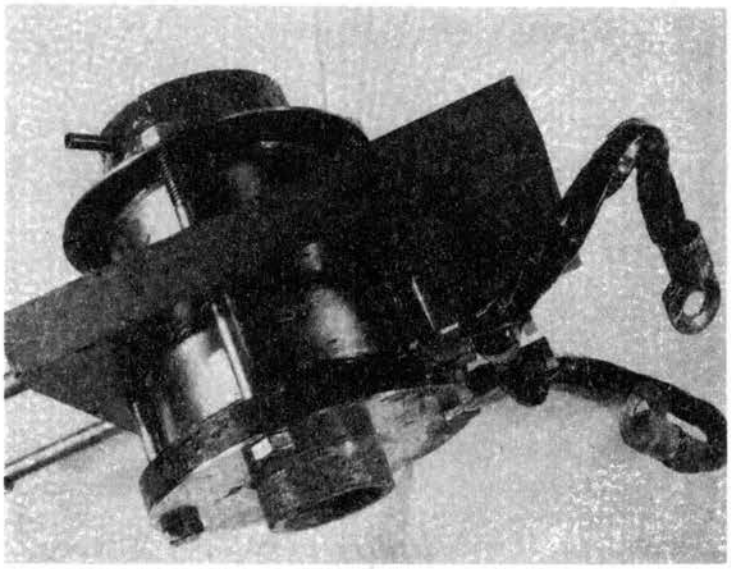

Figure 16. Wirewound Electromagnet

similar to that described by S. Foner and W. G. Fisher (32). Some galvanomagnetic measurements on diamond were made with these magnets. However, the mechanical containment of the Lorentz force was not sufficient and the lifetime of these magnets were short (when producing fields of 500 kilogauss).

Sample Holder and Variable Temperature Chamber

A cross section of the glass sample holder used to position the diamond in the electromagnet is shown in Figure 17. Cemented to a glass plate (A) are a pyrex glass tube (B), a corral made of four pieces of glass (C), and four binding posts (D) machined out of brass and fitted with minature screws (E) and washers. The binding posts served as a connecting link between the insulated, twisted pairs of lead wires (F), made of copper thermocouple wire, and the gold wires (G) bonded to the electrical contacts on the diamond. An iron-constantan thermocouple (H) positioned in close proximity to the diamond (J) is used to measure the temperature. The diamond is wedged securely in place with a number of mica sheets (K).

The variable temperature chamber shown in Figure 18 consists in a test tube (a) filled with a heavy paraffin oil and a nichrome strip (b) wrapped around the test tube. A seven turn search coil (c) made of insulated copper thermocouple wire is cemented to the test tube. Asbestos cloth (d) is wrapped around the heating strip, and the whole assembly is slipped inside a quartz tube (e). The ac power supply for the one ohm nichrome heater strip consists in a step-down transformer with a variable input controlled by an autotransformer.

The variable temperature chamber and the sample holder are placed

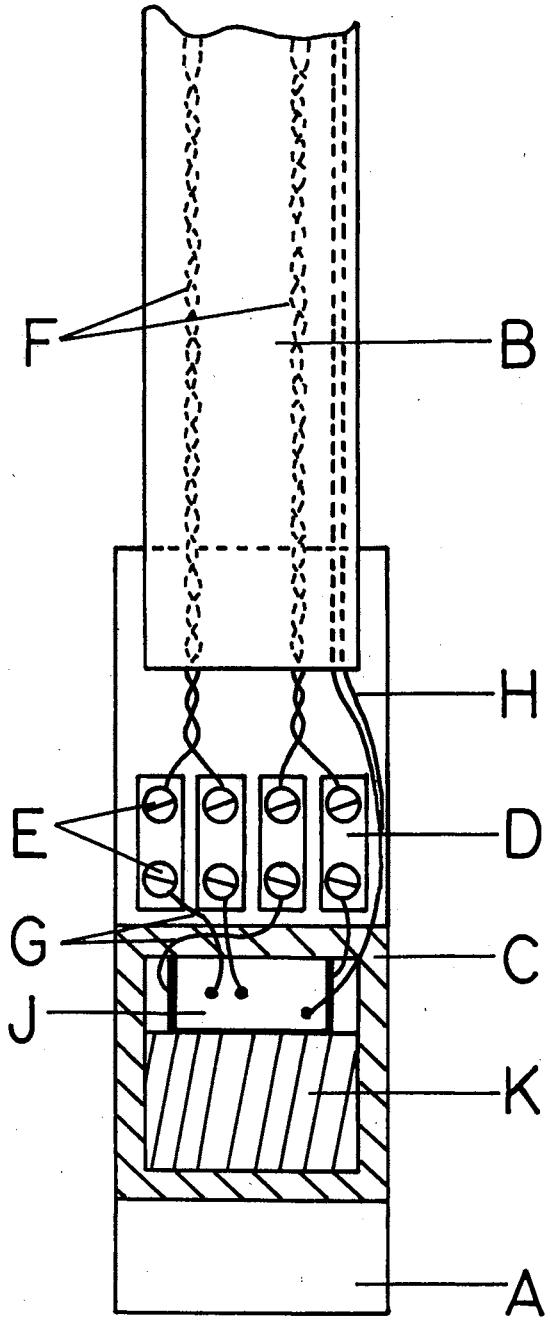

Figure 17. Cross Section of Sample Holder

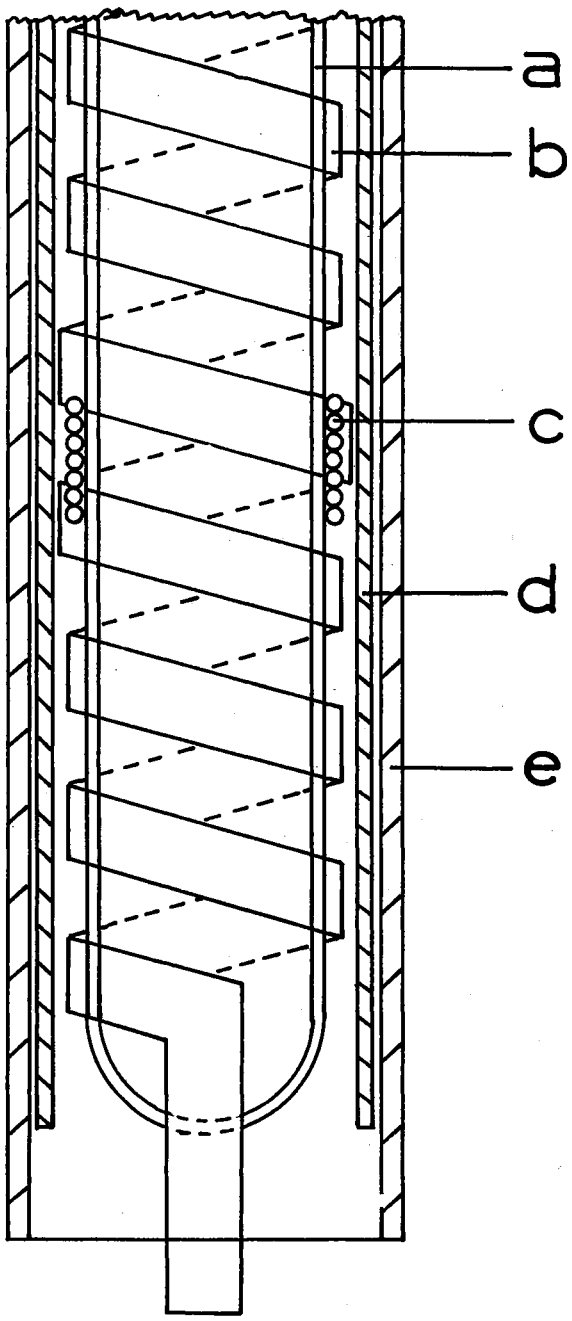

Figure 18. Cross Section of Variable Temperature Chamber

in the bore of the magnet so that both the search coil and the diamond are in the center of the magnet. Both the flow of water down the bore of the magnet and the heater current are adjusted to give the desired temperature of the diamond.

The final design of the sample holder and variable temperature chamber suffered from three defects. First of all, glass parts cannot be fitted together as plastic parts can; this caused an uncertainty as to the alignment of the diamond in the magnetic field. To offset this deficiency, the glass sample holder and variable temperature chamber were made long enough so that the alignment was known to within a tolerance of five degrees. The second defect is that the oil in the test tube could not be stirred due to a lack of room. This increases the size of the temperature gradients possible in the oil bath. The third defect is the time with which the diamond could be held at a constant temperature. It was determined that at 308^{o}K, the diamond could be held to within 0.25^{o}K for about two minutes. At 436^{o}K, the temperature cycled up and down, and the sample experienced temperature excursions of $\pm$ 3^{o}K. A temperature variation of 1^{o}K could be held for about 15 seconds.

Measurement Procedure

The procedure for actually making a complete set of measurements to compute the magnetoresistance is described in the following steps. Figure 19 is a simplified schematic of the circuit used in the experiment. (1) Both the current in the heater of the variable temperature chamber and the flow of water down the bore of the magnet were adjusted to give the desired temperature of the diamond to within the

tolerances previously mentioned. The temperature was determined by measuring the output of an iron-constantan thermocouple (in close proximity to the diamond) with a Leeds and Northrup Type K-3 Universal Potentiometer. (2) With the capacitor bank uncharged, the foot switch S was momentarily opened and the oscilloscope sweep was triggered. The trace on the oscilloscope screen was the potential difference between the probe contacts #1 and #2 in zero magnetic field; it was recorded on film using a Hewlett Packard Model 196A Oscilloscope Camera. A reference trace with the foot switch closed was also recorded. If the current in the diamond is in the "forward" direction, the potential difference between the straight line traces is E^0_{FI} and is illustrated in part (a) of Figure 20. (3) The capacitor bank was charged to the desired voltage. The foot switch S was opened, and the capacitors were discharged through the electromagnet. During the pulse, both the potential difference between the probe contacts on the diamond and the integrated output of the search coil were displayed on a Tektronix Type 551 Dual Beam Oscilloscope and recorded on film. Reference traces were recorded immediately after the discharge. The signal from the search coil was fed into a Tektronix Type O Plug-In connected as an integrator. The amplitude of the trace, labeled $\mathcal{E}_H$ in part (a) of Figure 20, was proportional to the magnetic field; the proportionality constant is determined by the area-turns (19.2 $cm.^2$-turns) of the search coil and the RC time constant of the integrator. The signals from the probe contacts were ac coupled into the "A" and "B" inputs of a Tektronix Type D Plug-In connected in the "A-B" mode. The potential difference at each input was measured relative to a grounded current contact on the diamond. For a "forward" current in the diamond and a "forward"

magnetic field, the trace recorded gives $E_{FIFH}-E^0_{FI}$; this is shown in part (a) of Figure 20. The traces shown in Figures 20 and 21 do not show a contribution due to the electromotive force induced in the diamond. This was not the case for all measurements; however the induced emf in all cases was much smaller (typically less than 20% of the maximum voltage recorded) than the voltages used in measuring the magnetoresistance. (4) Usually the discharge of the capacitors through the electromagnet had heated the magnet and the diamond. The flow of water down the bore of the magnet and the current in the heater strip were adjusted to bring the diamond back to the desired temperature. (5) The procedure described in steps (1) through (4) were repeated with the only difference being that the direction of the sample current was reversed. The voltage recorded in step (2) was E^0_{RI} and is shown in part (b) of Figure 20. The voltages recorded in step (3) are $\mathcal{E}_H$ and $E_{RIFH} - E^0_{RI}$; these are also shown in part (b) of Figure 20. The opposite current contact on the diamond to that used in steps (1) through (4) was grounded. (6) The procedure described in steps (1) through (5) were repeated with the only difference being that the direction of the magnetic field was reversed. The voltages which are recorded for the sample current in the "forward" direction, namely E^0_{FI}, $\mathcal{E}_H$, and $E_{FIRH} - E^0_{FI}$, are shown in part (a) of Figure 21. Likewise, the voltages which were recorded for the sample current in the "reverse" direction, namely E^0_{RI}, $\mathcal{E}_H$, and $E_{RIRH} - E^0_{RI}$, are shown in part (b) of Figure 21. (7) The gain of the oscilloscope and the magnification of the camera were measured by displaying a calibrated square wave on the oscilloscope screen and recording it on film. The voltages as a function of the magnetic field were measured from the photographs and

combined as indicated in equation (6) to yield the magnetoresistance as a function of the magnetic field.

The procedure for actually making a complete set of Hall effect measurements is the same as described in the above paragraph. A typical set of photographs from which the data was measured is shown in Figures 22 and 23; the appropriate voltages which were recorded are clearly labeled in the same manner as in Figures 20 and 21. Instead of using the probe contacts #1 and #2, either the pair of contacts #1 and #3 or the pair of contacts #2 and #3 were used. In addition, the current in the diamond was determined by measuring the volt- across a 30 ohm precision resistor in series with the diamond. This resistor is not shown in Figure 19. The voltages from the set of photographs were combined as given in equation (8) to yield the Hall coefficient as a function of the magnetic field.

The probe contact #3 was purposely placed on the surface of the diamond nearly opposite to contact #2. This allowed the voltages recorded with the pair of contacts #2 and #3 to be approximately sensitive to only the Hall voltage; the voltages recorded with the pair of contacts #1 and #3 are sensitive to both the Hall voltage and the magnetoresistance.

The constant current power supply consisted in a Hewlett-Packard Type 712B constant voltage power supply, labeled "B" in Figure 19, and a North Hill Model CG-1 current govenor, labeled "R" in Figure 19.

The magnetic field dependence of a galvanomagnetic effect up to 150 kilogauss was recorded in three steps. The dependence was first measured in magnetic fields up to 11 kilogauss; the capacitor bank was charged to only 275 volts. Next, the dependence was measured in

magnetic fields up to 70 kilogauss; the capacitor bank was charged to 1700 volts. Finally, the dependence on magnetic fields up to 150 kilogauss was achieved by charging the capacitor bank to 3800 volts.

The dependence of the magnetoresistance on magnetic field did exhibit little correlation with the aforementioned pattern of magnetic field production. However, the dependence of the Hall coefficient on the magnetic field was strongly correlated to the above pattern.

The Diamond Specimen

The specimen examined in this study, referred to as DS-2, was a semiconducting diamond geometrically close to a rectangular parallelepiped with sides equal to the dimensions listed in Figure 24. The large faces lie about 8^{o} off the true $(\bar{1}11)$ planes. The faces with dimensions 6.4 millimeters by 2.2 millimeters are close to $(11\bar{3})$ planes (within 2^{o}). The small faces are within $\frac{1}{2}^{o}$ to (110) planes. The surfaces are highly polished for optical work. The diamond can be classified visually into a blue region and a clear region, as illustrated in Figure 24. The blue region extends from one end to about 2 millimeters into the diamond. The color, though faint, is easily visible to the unaided eye. The two regions, though both semiconducting, show remarkable differences. In the blue end, the room temperature resistivity ranges from 62.5 ohm-cm. to 287 ohm-cm., while in the clear end it varies from 177 kiloohm-cm. to 350 kiloohm-cm. (12). Much experimental work has been done on this diamond (12, 15).

The electrical contacts were always put on the blue end of the specimen in about the central portion of the blue section. The size and position of the contacts were recorded so that a geometrical correction

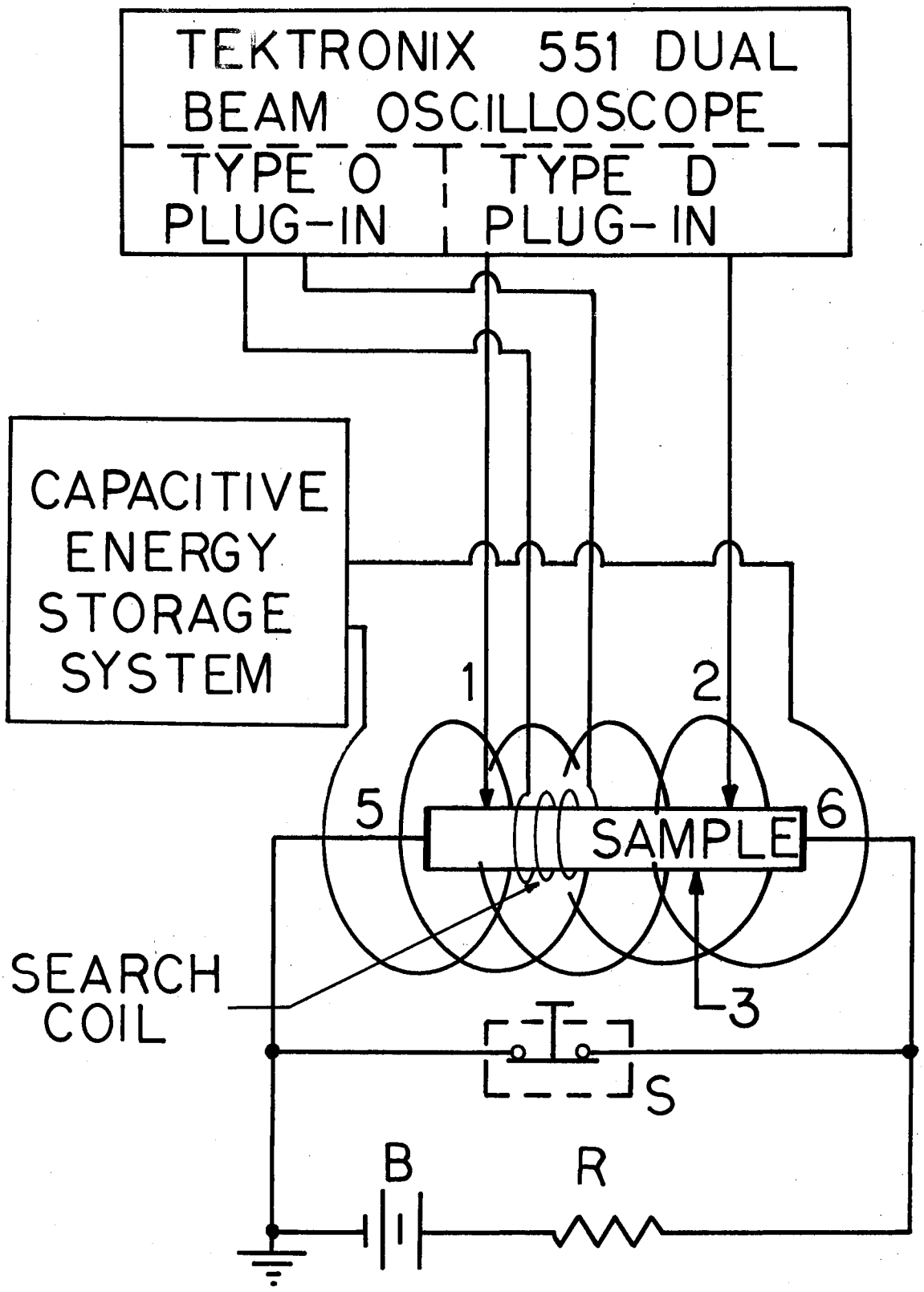

Figure 19. Simplified Circuit Used in Galvanomagnetic Measurements

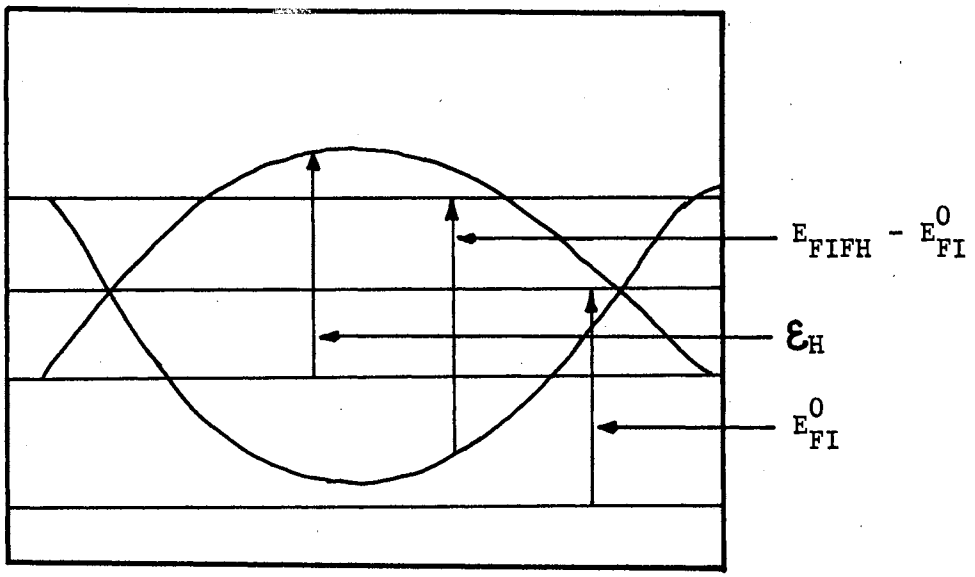

(a) Forward Sample Current

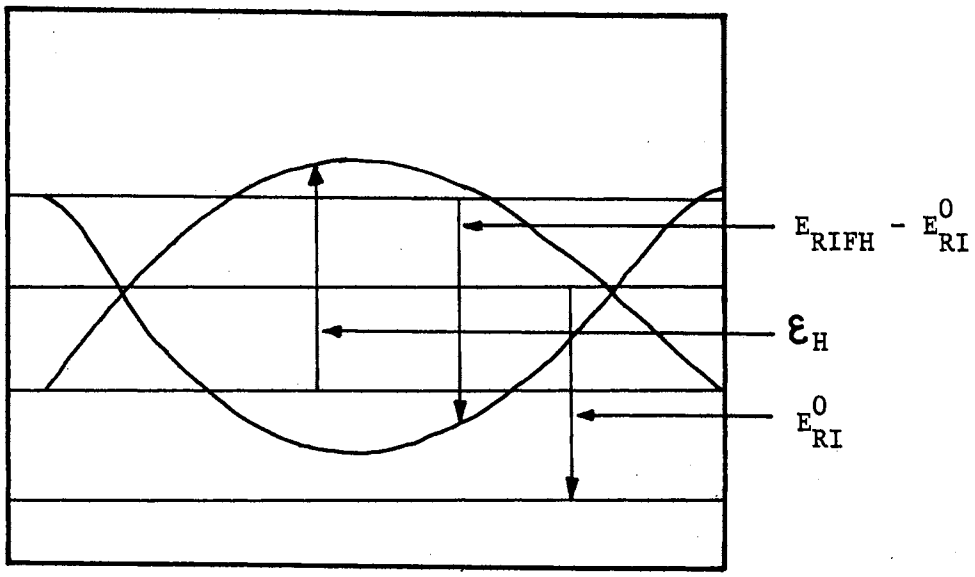

(b) Reverse Sample Current

Figure 20. Data Record Used to Compute Magnetoresistance of DS-2 in Forward Magnetic Field

All voltages measured in direction of the arrows (positive voltage upward and negative voltage downward).

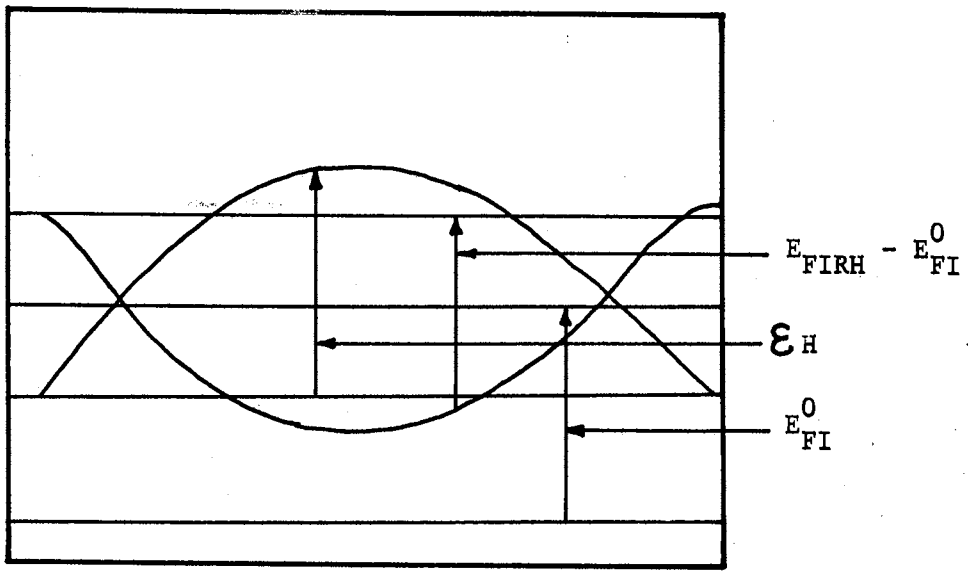

(a) Forward Sample Current

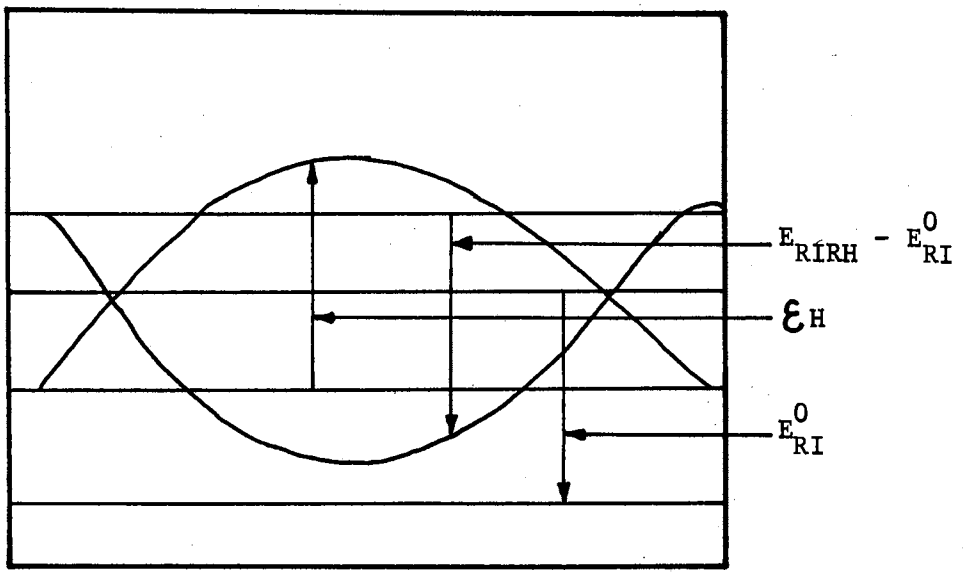

(b) Reverse Sample Current

Figure 21. Data Record Used to Compute Magnetoresistance of DS-2 in Reverse Magnetic Field

All voltages measured in direction of the arrows (positive voltage upward and negative voltage downward).

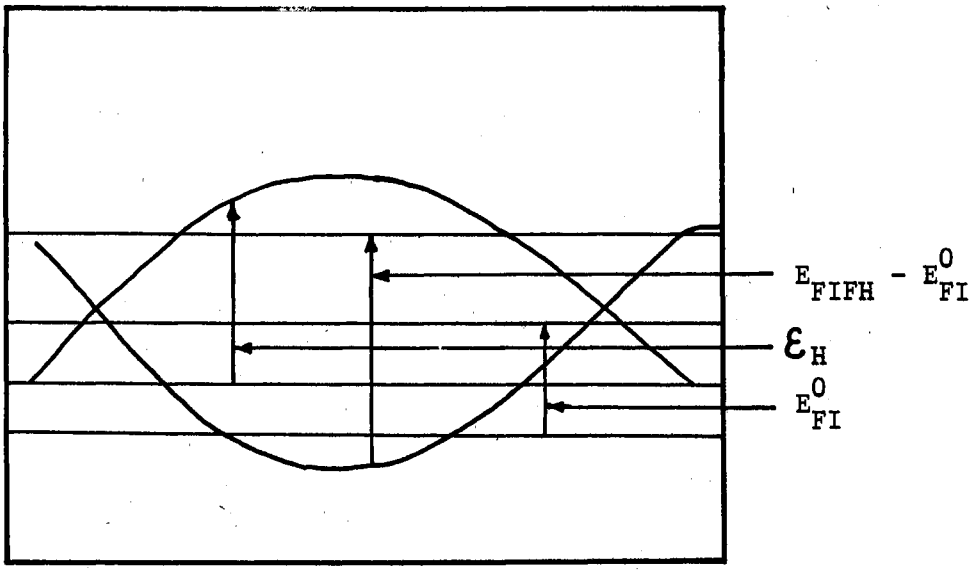

(a) Forward Sample Current

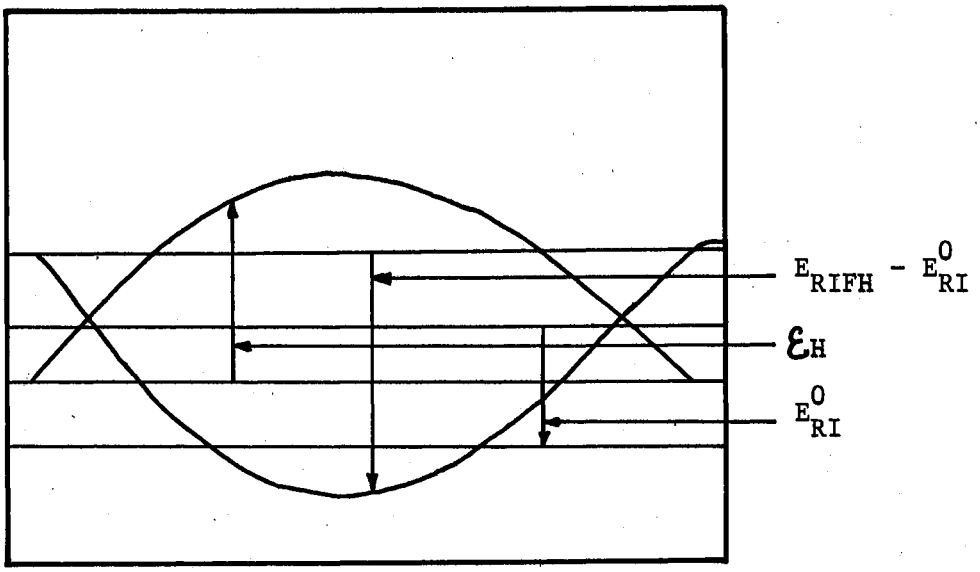

(b) Reverse Sample Current

Figure 22. Data Record Used to Compute Hall Coefficient of DS-2 in Forward Magnetic Field

All voltages measured in direction of the arrows (positive voltage upward and negative voltage downward).

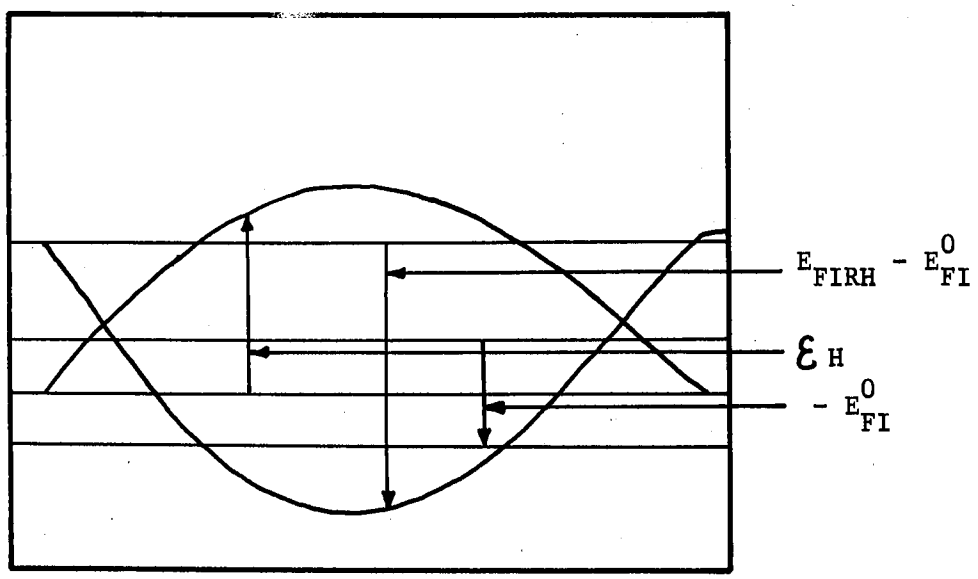

(a) Forward Sample Current

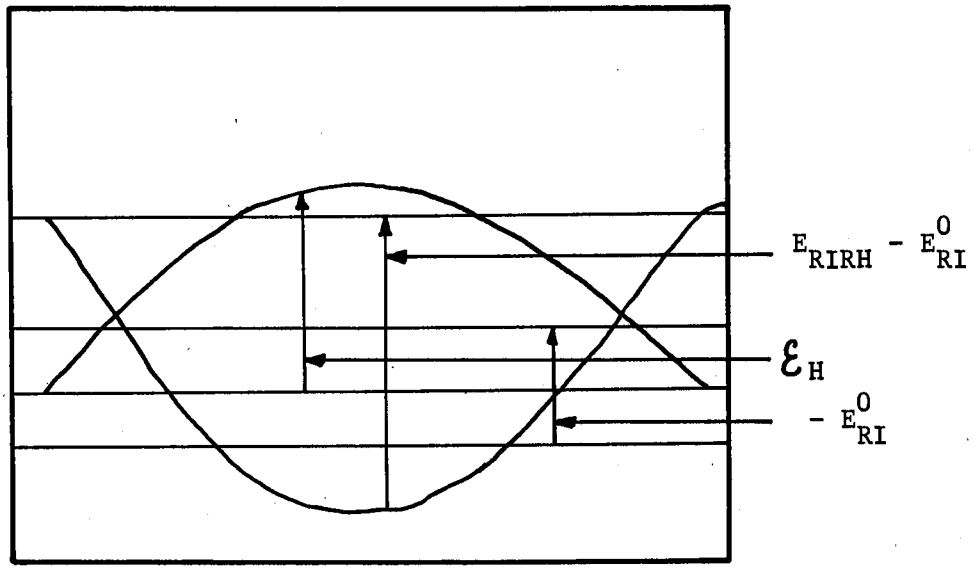

(b) Reverse Sample Current

Figure 23. Data Record Used to Compute Hall Coefficient of DS-2 in Reverse Magnetic Field

All voltages measured in direction of the arrows (positive voltage upward and negative voltage downward).

to the data could be accomplished.

With respect to the theoretical calculations, the specimen, DS-2, was approximated as being exactly a rectangular parallelepiped with crystal faces whose normals lie along the $[110]$, $[\bar{1}11]$, and $[1\bar{1}2]$ axes. In all graphs, these three sets of Miller indices are used along with the set $[110]$, $[\bar{1}11]$ and $[1\bar{1}3]$ as determined from back-reflection Laue photographs.

Electrical Contacts to the Diamond

Electrical contacts to the diamond were made in essentially the same manner as that described by M. D. Bell and W. J. Leivo (33). Differences in the techniques do warrant a discussion. The diamond was cleaned by heating it in a bath of aqua regia for about ten minutes. To make a probe contact, a small spot of a suspension of titanium hydride in amyl acetate was applied to the surface of the diamond with the point of a fine sewing needle. After the suspension dried, a thin layer of an alloy powder was placed over the titanium hydride. The alloy powder, Incusil 15, size 325 mesh, is a commercial alloy of indium, copper, and silver. A drop of amyl acetate was carefully placed on the diamond surface so as to wet the alloy powder. Before the spot was thoroughly dry, a toothpick was used to clean away any excess powder on the diamond surface and reduce the size of the spot. The diamond was then slowly heated to 800°C for 3 minutes at a pressure of 10^{-4} mm. of mercury. A slow cooling process yielded a mechanically strong and electrically stable contact. After all electrical contacts were put on the diamond, gold wires were attached to the contacts using a nailhead thermocompression tool. To remove the contacts, a

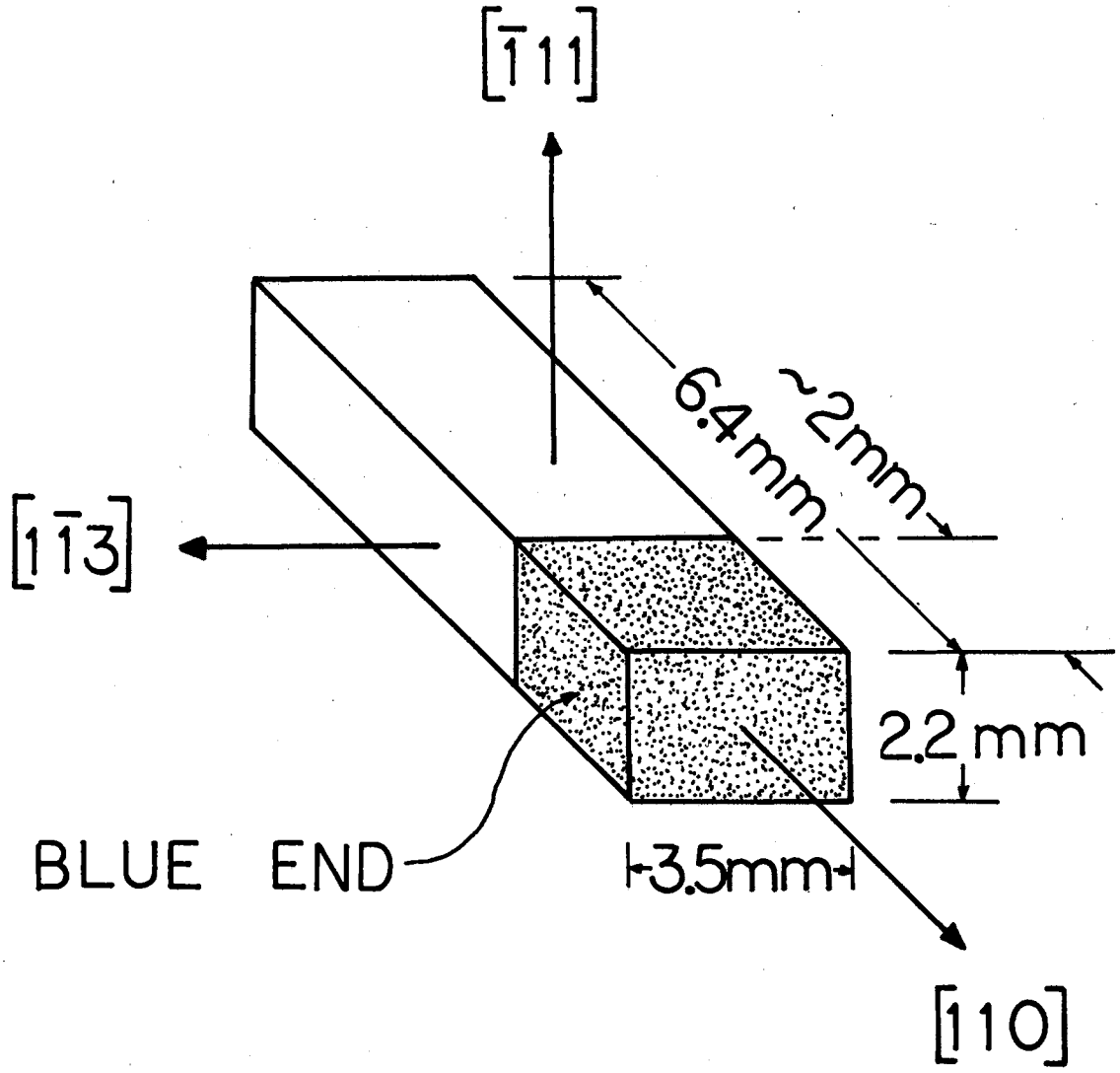

Figure 24. The Specimen DS-2

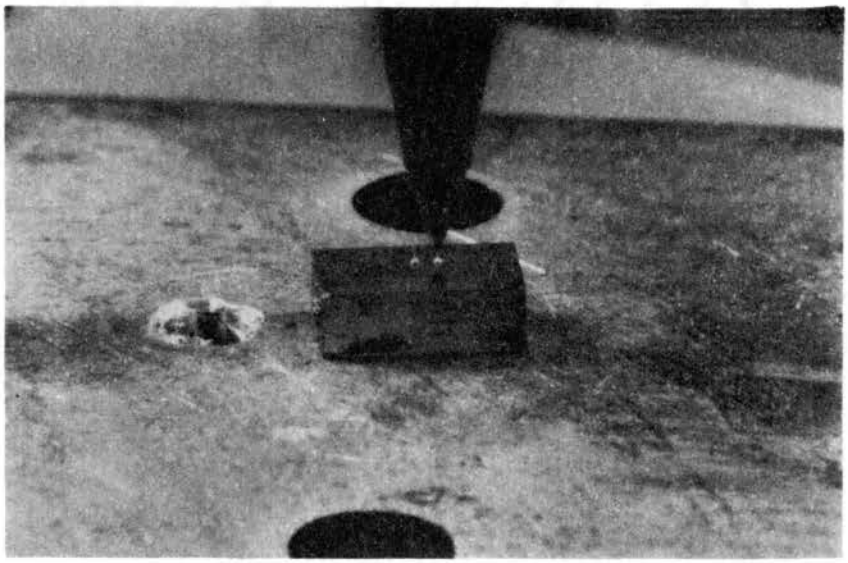

Figure 25. Diamond Specimen DS-2

The upper part of the photograph shows the nail-head thermocompression tool used to attach the gold wire (0.001 inch in diameter) to the electrical contact on the diamond surface.

CHAPTER IV

RESULTS

Magnetoresistance: Magnetic Field Along the $[1\bar{1}0]$ Axis

With the electric current density along the $[1\bar{1}0]$ axis, the two independent measurements of the longitudinal magnetoresistance at 308° K are shown in Figure 26. The single measurement of the longitudinal magnetoresistance at 436°K is shown in Figure 27. This data, as well as all other data presented in this chapter and denoted by the symbols "●" , and "o" , were taken in pulsed magnetic fields. It was shown by K. J. Russell (15) that galvanomagnetic measurements made in low pulsed magnetic fields did smoothly overlap measurements made in steady magnetic fields. The solid line, long-dash-short-dash line, and short-dash line are the results of theoretical calculations of the magnetoresistance and will be discussed in Chapter V. In taking the data symbolized by the black dots in Figure 26, it was noted that the quantity $E_{FIFH} - E^{0}_{FI}$ was negative (opposite to the positive quantity expected), and that the quantity $E_{RIFH} - E^{0}_{RI}$ was positive (opposite to the negative quantity expected); both terms were nearly independent of the magnetic field for fields less than 11 kilogauss. Above 11 kilogauss, the signs of the above terms changed, and the terms became field dependent. Since the $[1\bar{1}0]$ axis is, to a first approximation, perpendicular to the boundary separating the blue and white regions of the

diamond (see Figure 24), a gradient in the density of holes should exist along this axis. The change in sign of the above quantities, as well as the difference between the measurements at 308°K, may result from this gradient in the concentration of holes. Comparing the solid dot data in Figures 26 and 27 indicate that the 128°K rise in temperature reduced the magnetoresistance by a factor of approximately two. The break at 70 kilogauss in the data symbolized by the circles in Figure 26 is correlated with the method of producing the high magnetic fields.

Figures 28 and 29 illustrate respectively the transverse magnetoresistance at 308°K and 436°K for the case of the current along the $[\bar{1}11]$ axis. The data symbolized by the cross "+" were taken by K. J. Russell (15); it is included as another independent measurement of the magnetoresistance at 308°K. The solid dot data were taken using the magnetoresistance probe contacts (contacts #1 and #2 in Figure 19); the circles are data taken with the Hall effect probe contacts (the pair of contacts #1 and #3 in Figure 19 positioned to be sensitive to both the Hall effect and the magnetoresistance). Exceptions to this nomenclature in the case of longitudinal magnetoresistance are understood; exceptions with respect to transverse magnetoresistance will be stated in the text. Notice that the spread between the solid dot and circle data increased with decreasing temperature. This may be associated with the nature of the probe contacts. Roughly, the magnetoresistance at 436°K is one half of its value at 308°K.

The transverse magnetoresistances at 308°K and 436°K for the current density direct along the $[1\bar{1}3]$ axis are shown respectively in Figures 30 and 31. The data symbolized by the circles are not as smooth as that symbolized by the solid dots because the magneto-

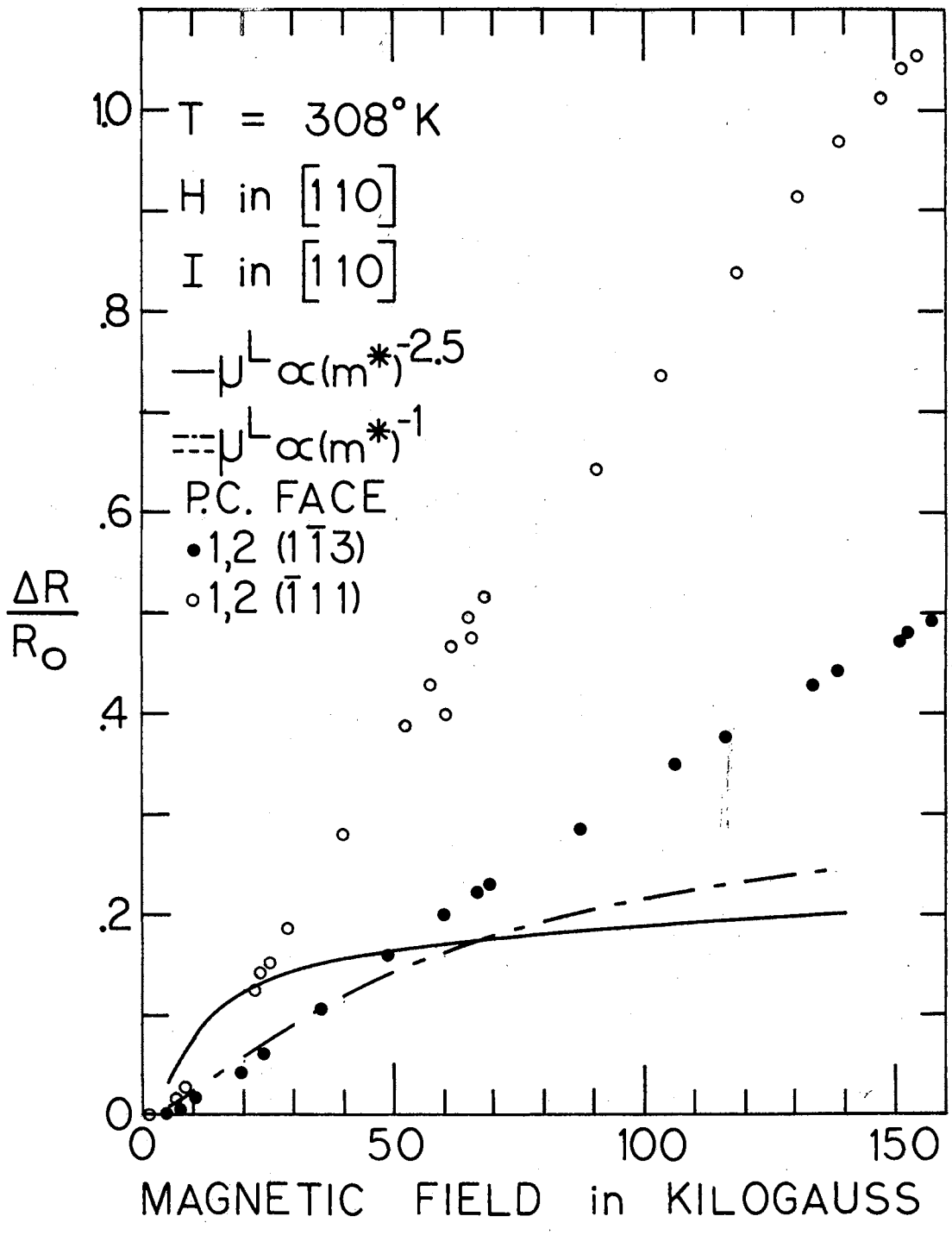

Figure 26. Longitudinal Magnetoresistance of DS-2 at 308°K in the [$\bar{1}$10] Direction

See Table VII for numerical parameters yielding theoretical results and Figure 19 for probe contact (P.C.) position.

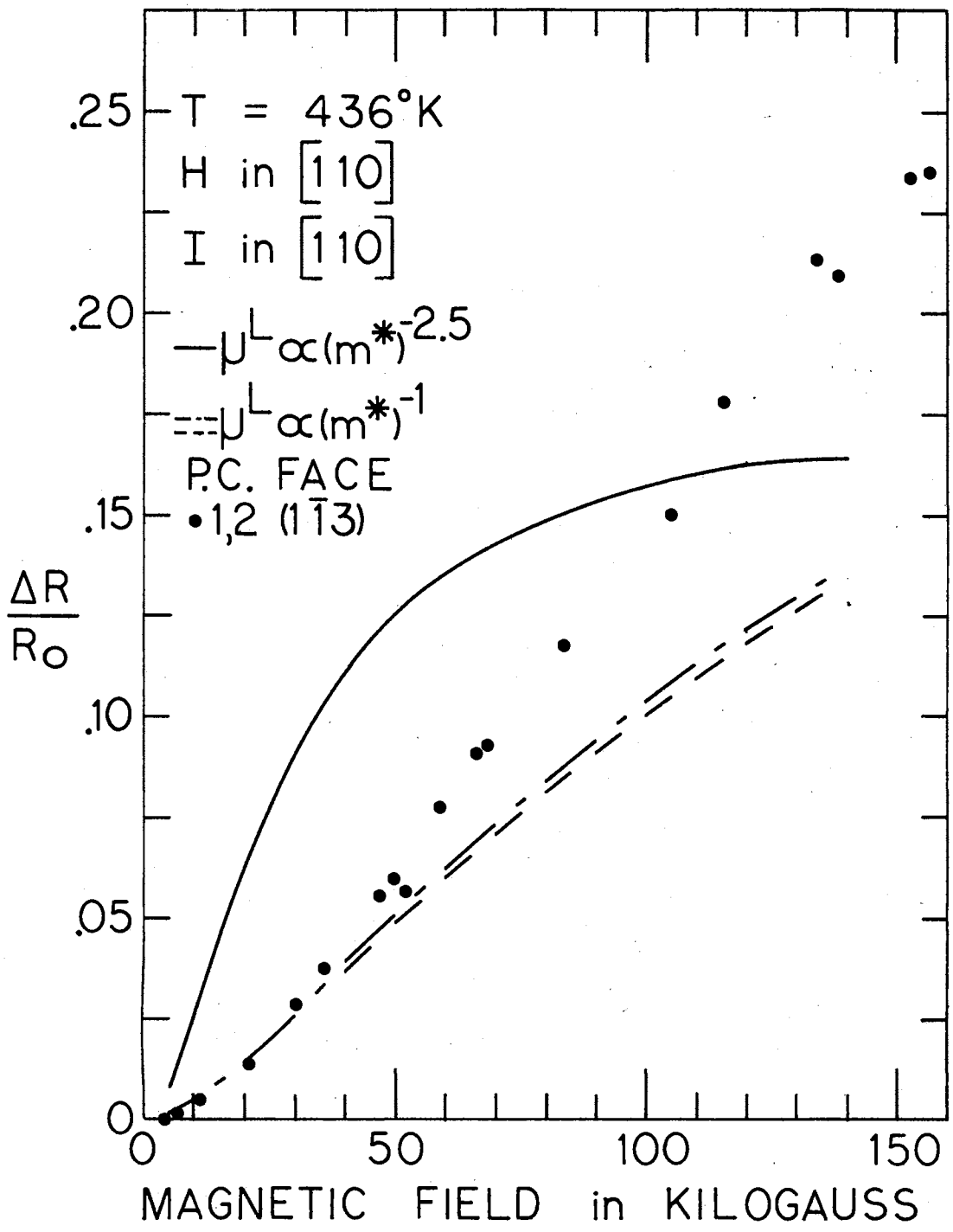

Figure 27. Longitudinal Magnetoresistance of DS-2 at 436°K in the [110] Direction

See Table VII for numerical parameters yielding theoretical results and Figure 19 for probe contact (P.C.) position.

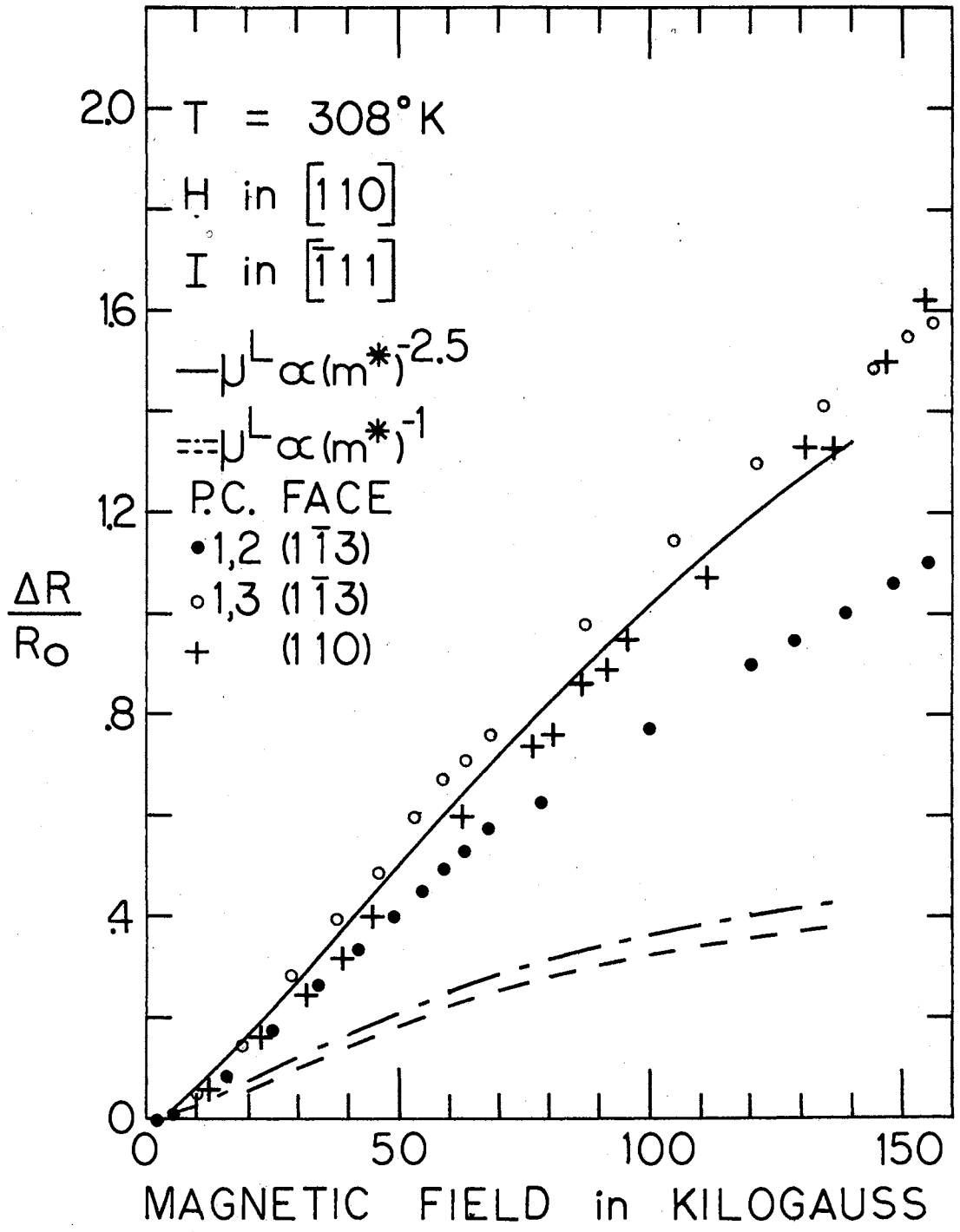

Figure 28. Transverse Magnetoresistance of DS-2 at 308°K with H in the [110] and I in the [1̄11] Directions

See Table VII for numerical parameters yielding theoretical results and Figure 19 for probe contact (P.C.) position.

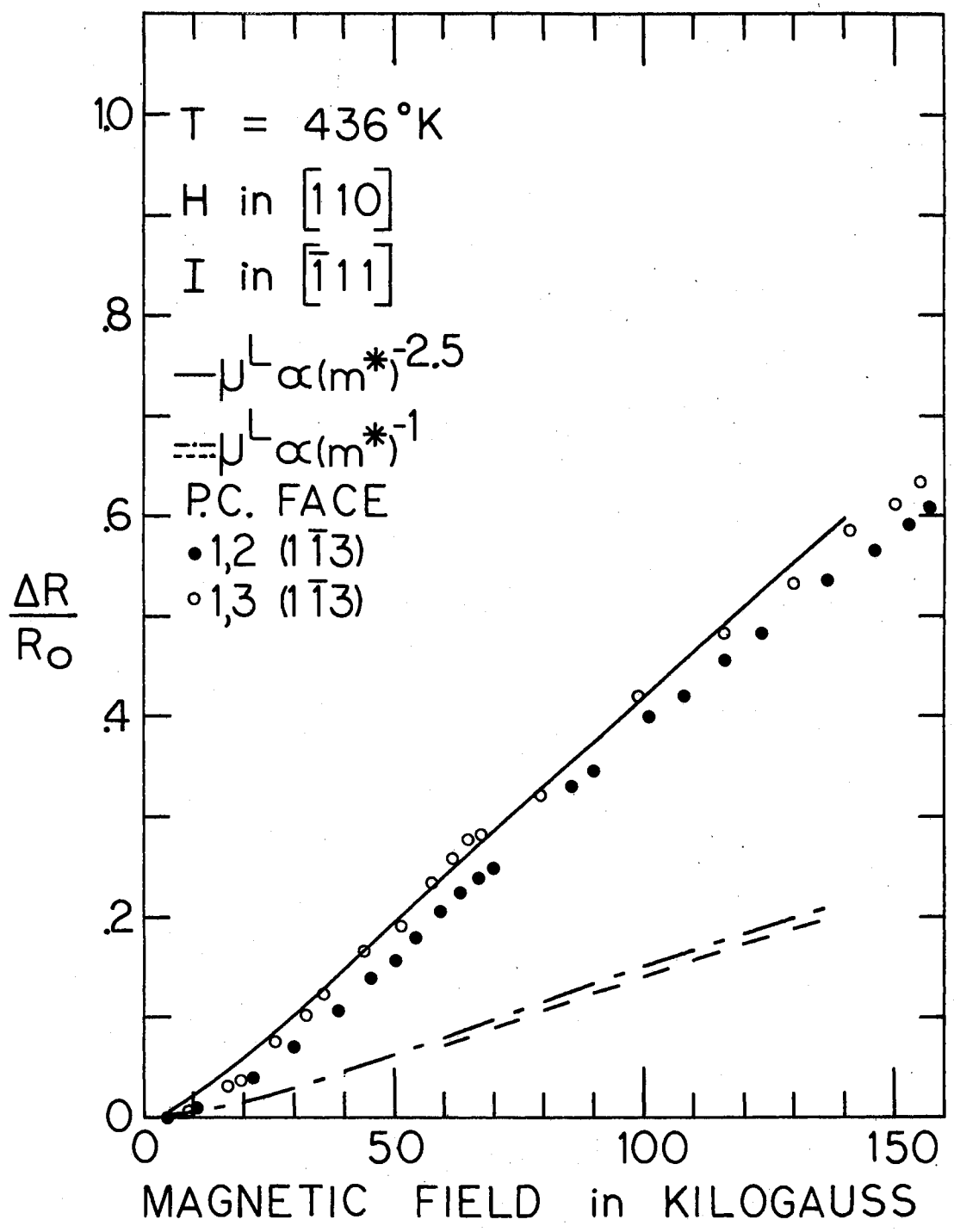

Figure 29. Transverse Magnetoresistance of DS-2 at 436°K with H in the [110] and I in the [$\bar{1}$11] Directions

See Table VII for numerical parameters yielding theoretical results and Figure 19 for probe contact (P.C.) position.

resistance was computed from the difference between the large voltages measured with the Hall effect probe contacts #1 and #3. Note that the spread between the experimental runs symbolized by dots and circles increased with the increase in temperature. The data symbolized by the solid dots are reduced by a factor of approximately 1.7 with the increase in temperature of 128°K between Figures 30 and 31; the circled data are reduced by a factor of nearly three.

Magnetoresistance: Magnetic Field Along the $[\bar{1}11]$ Axis

With the electric current density directed along the $[\bar{1}11]$ axis, the independent measurements of the longitudinal magnetoresistance at 308°K are shown in Figure 32. The single measurement of the longitudinal magnetoresistance at 436°K is shown in Figure 33. Note that the data symbolized by the circles in Figure 32 indicate almost a complete saturation of the magnetoresistance at 150 kilogauss while the solid dot data only indicate a tendency towards saturation. The difference between the two sets of data above 70 kilogauss may be indicative of the nature of the probe contacts in a time varying magnetic field. The increase in temperature of 128°K decreased the longitudinal magnetoresistance by a factor of two. The break at 70 kilogauss in the data at 436°K is correlated with the method of producing the magnetic fields.

Figures 34 and 35 respectively illustrate the transverse magnetoresistance at 308°K and 436°K for the case of the current along the $[110]$ axis. In taking the data symbolized by the solid dots in Figure 34, it was noted that the quantity $E_{FIFH} - E^{0}_{RI}$ was positive for all values of the magnetic field; its dependence on the magnetic field was

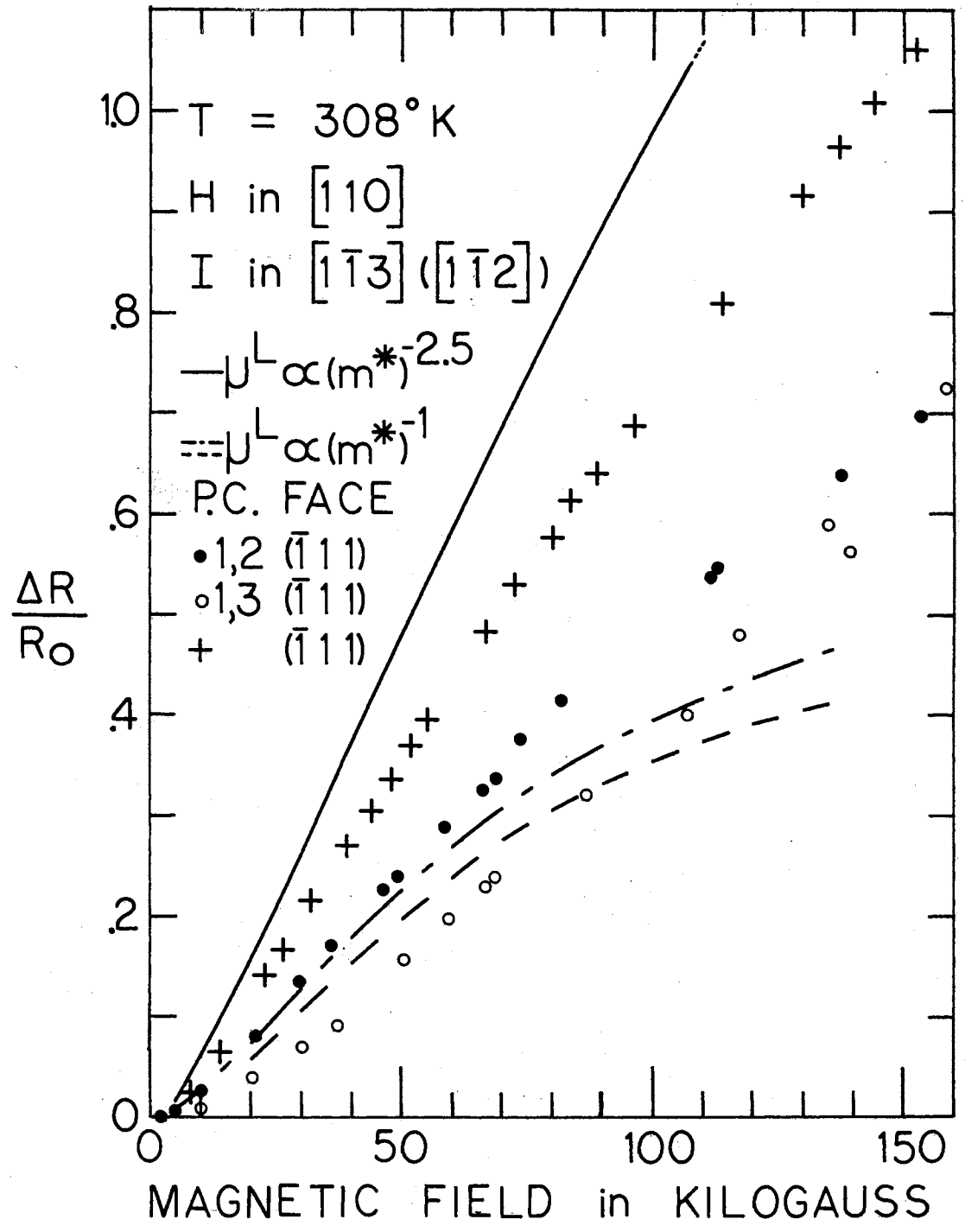

Figure 30. Transverse Magnetoresistance of DS-2 at 308°K with H in the [110] and I in the [1$\bar{1}$3] Directions

See Table VII for numerical parameters yielding theoretical results and Figure 19 for probe contact (P.C.) position.

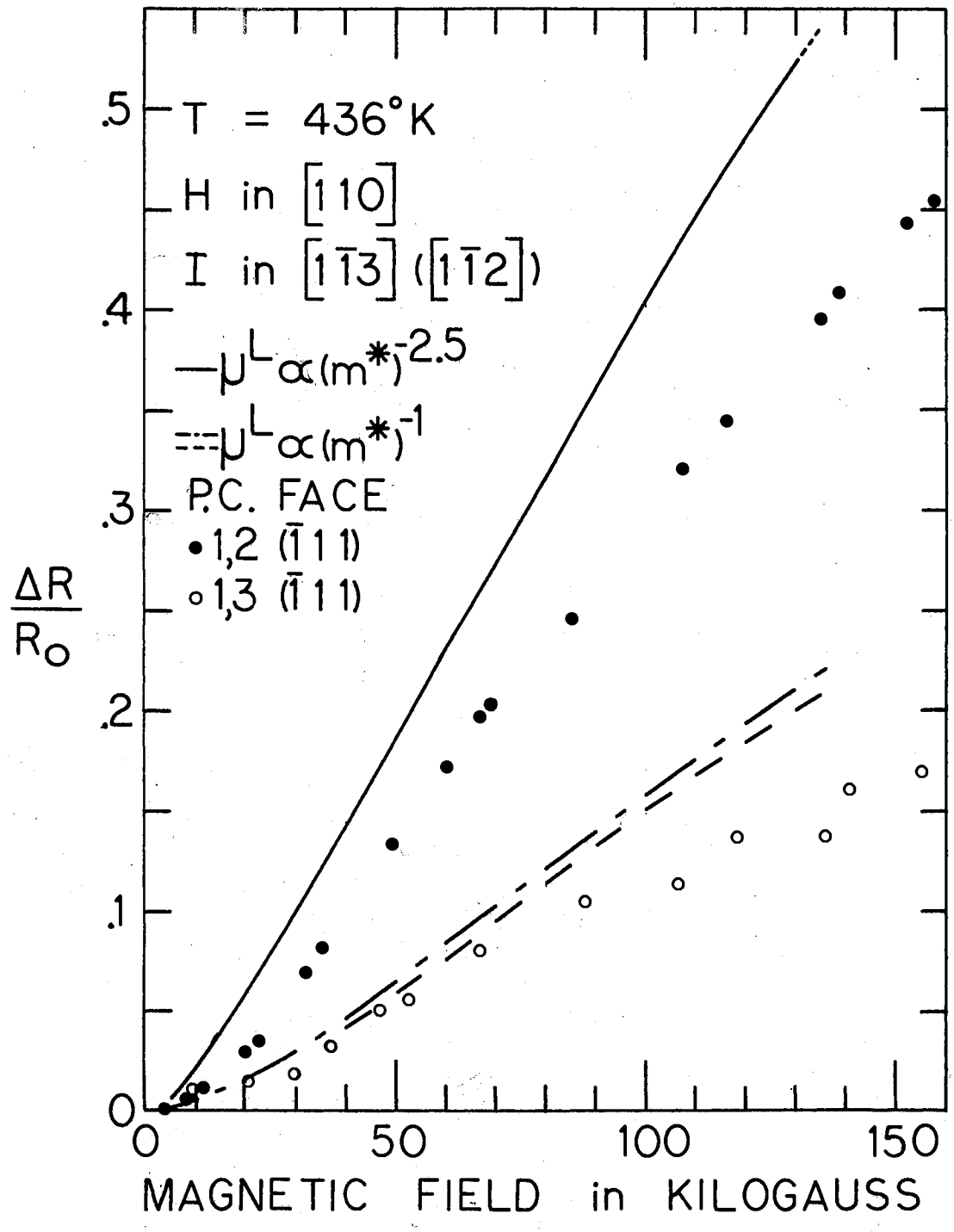

Figure 31. Transverse Magnetoresistance of DS-2 at 436°K with H in the [110] and I in the [1$\bar{1}$3] Directions

See Table VII for numerical parameters yielding theoretical results and Figure 19 for probe contact (P.C.) position.

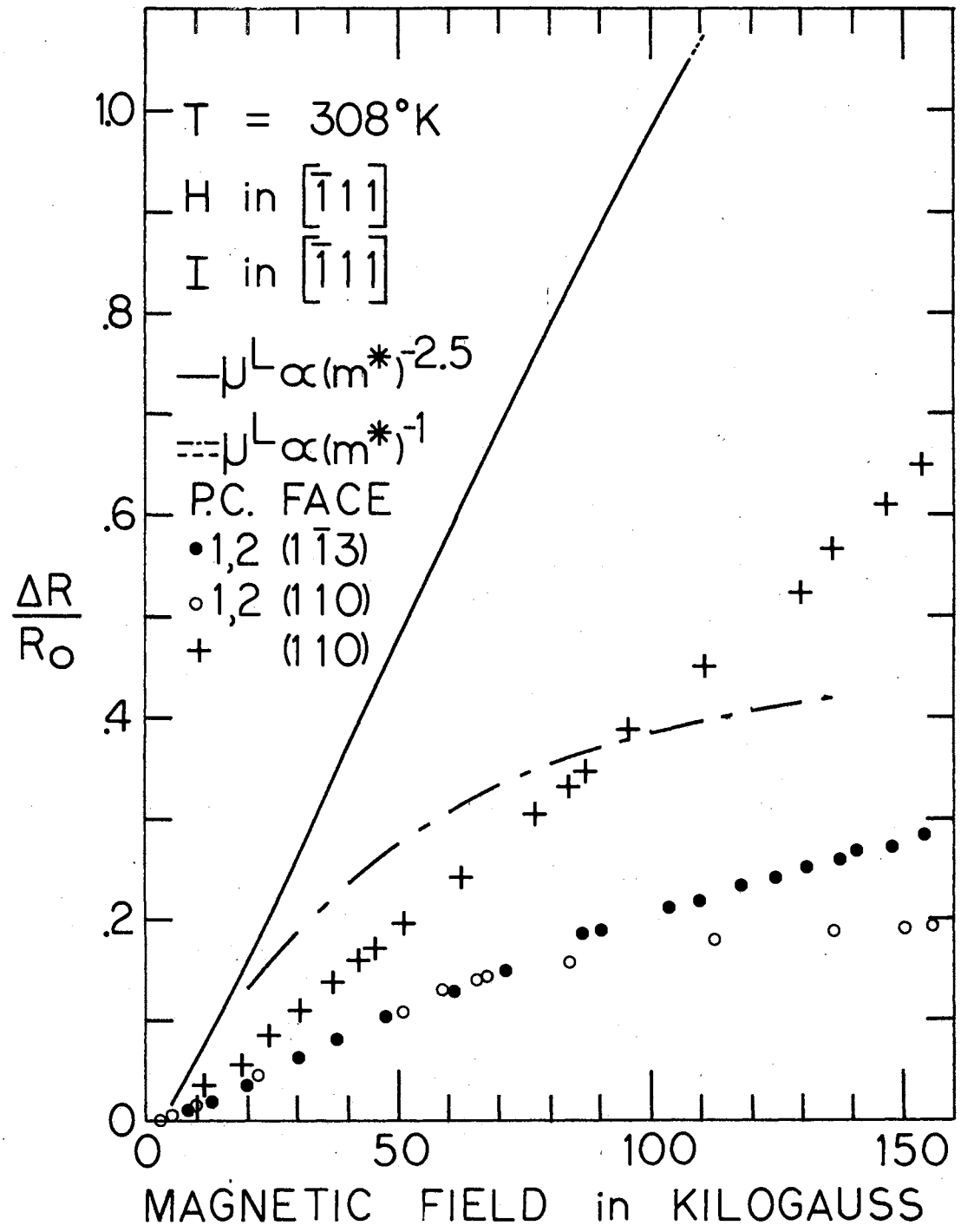

Figure 32. Longitudinal Magnetoresistance of DS-2 at 308°K in the [1̄11] Direction

See Table VII for numerical parameters yielding theoretical results and Figure 19 for probe contact (P.C.) position.

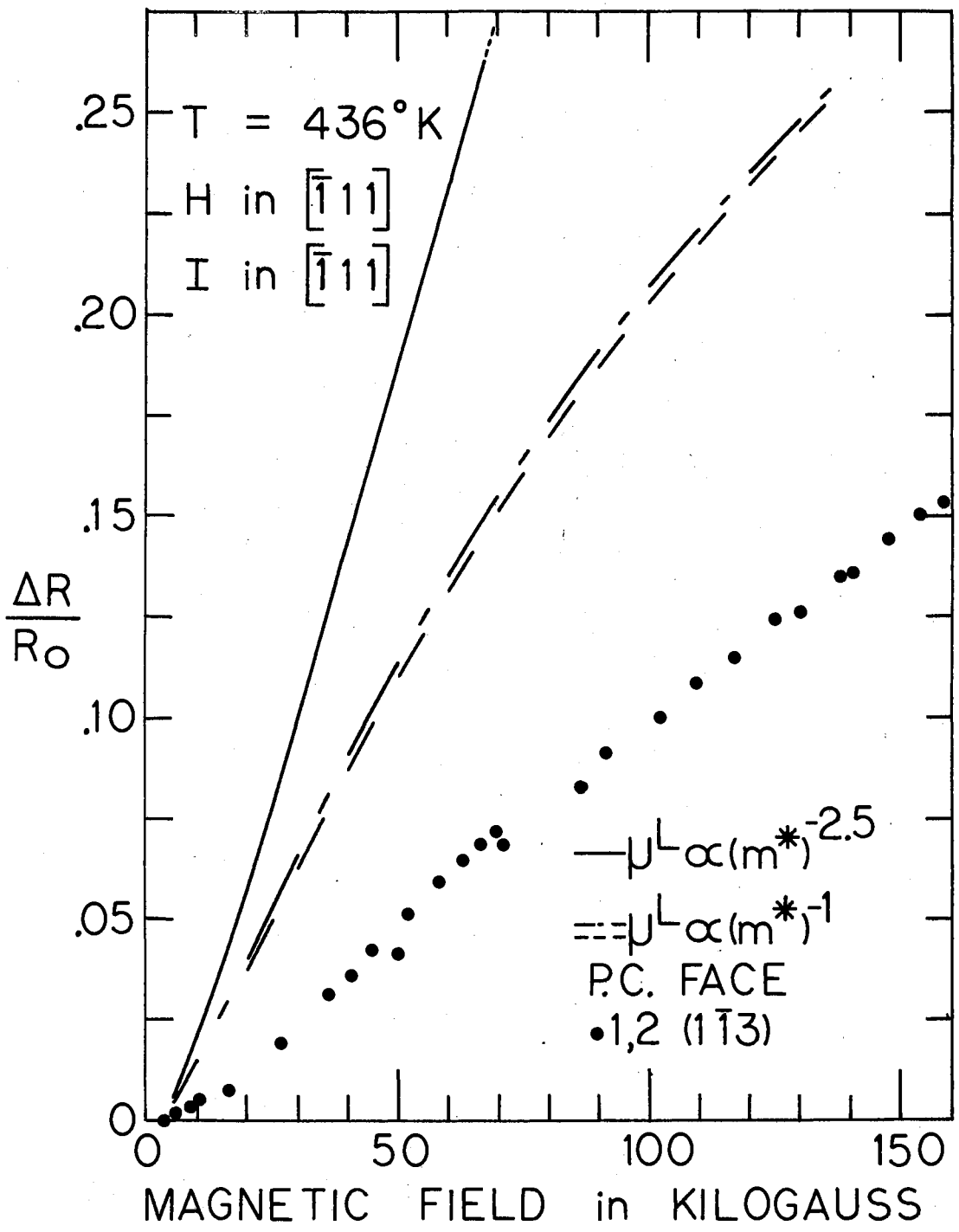

Figure 33. Longitudinal Magnetoresistance of DS-2 at 436°K in the [$\bar{1}$11] Direction

See Table VII for numerical parameters yielding theoretical results and Figure 19 for probe contact (P.C.) position.

weakened (although not constant) for magnetic fields above about 30 kilogauss. In recording the solid dot data at 436°K, it was noted that the quantity $E_{FIFH} - E^{0}_{FI}$ was negative for all magnetic fields, and the quantity $E_{RIFH} - E^{0}_{RI}$ was positive for all fields; the dependence of both quantities on the magnetic field was essentially identical. The increase of 128°K in the temperature reduced the magnetoresistance by a factor of two. Comparing Figures 34 and 28 and comparing Figures 35 and 29 seems to indicate that an interchange in the directions of the magnetic field and current density vectors produces nearly the same transverse magnetoresistance.

The transverse magnetoresistances at 308°K and 436°K for the current density along the $[1\bar{1}3]$ axis are shown respectively in Figures 36 and 37. The independent measurements were both made with two different pairs of magnetoresistance probe contacts (contacts #1 and #2 in Figure 19); however, the data symbolized by circles were taken with the contacts on the $(\bar{1}11)$ face of the diamond, which is perpendicular to the magnetic field. Since the finite area of the probe contacts on the $(\bar{1}11)$ face do short out part of the Hall field, it is expected that the recorded magnetoresistance would be larger than that recorded (solid dot) for the probe contacts on the (110) face (an idealized Hall equipotential plane). This conclusion is supported by the data shown in Figures 36 and 37. The data (+) taken by K. J. Russell (15) was recorded with the probe contacts on the $(\bar{1}11)$ face. Note that the 128°K difference in temperature between the two sets of data reduced the size of the transverse magnetoresistance by about 15%.

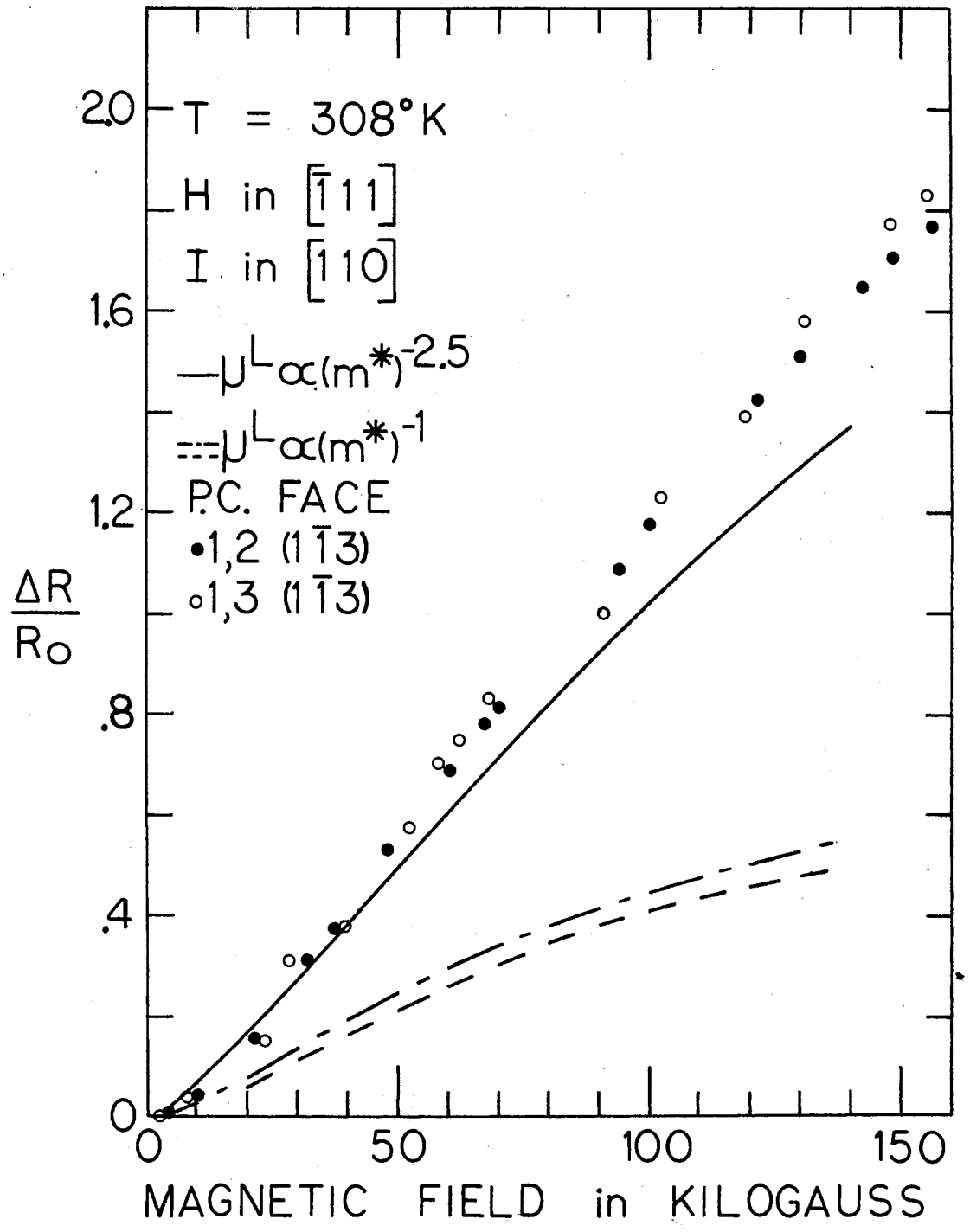

Figure 34. Transverse Magnetoresistance of DS-2 at 308°K with H in the [$\bar{1}$11] and I in the [110] Directions

See Table VII for numerical parameters yielding theoretical results and Figure 19 for probe contact (P.C.) position.

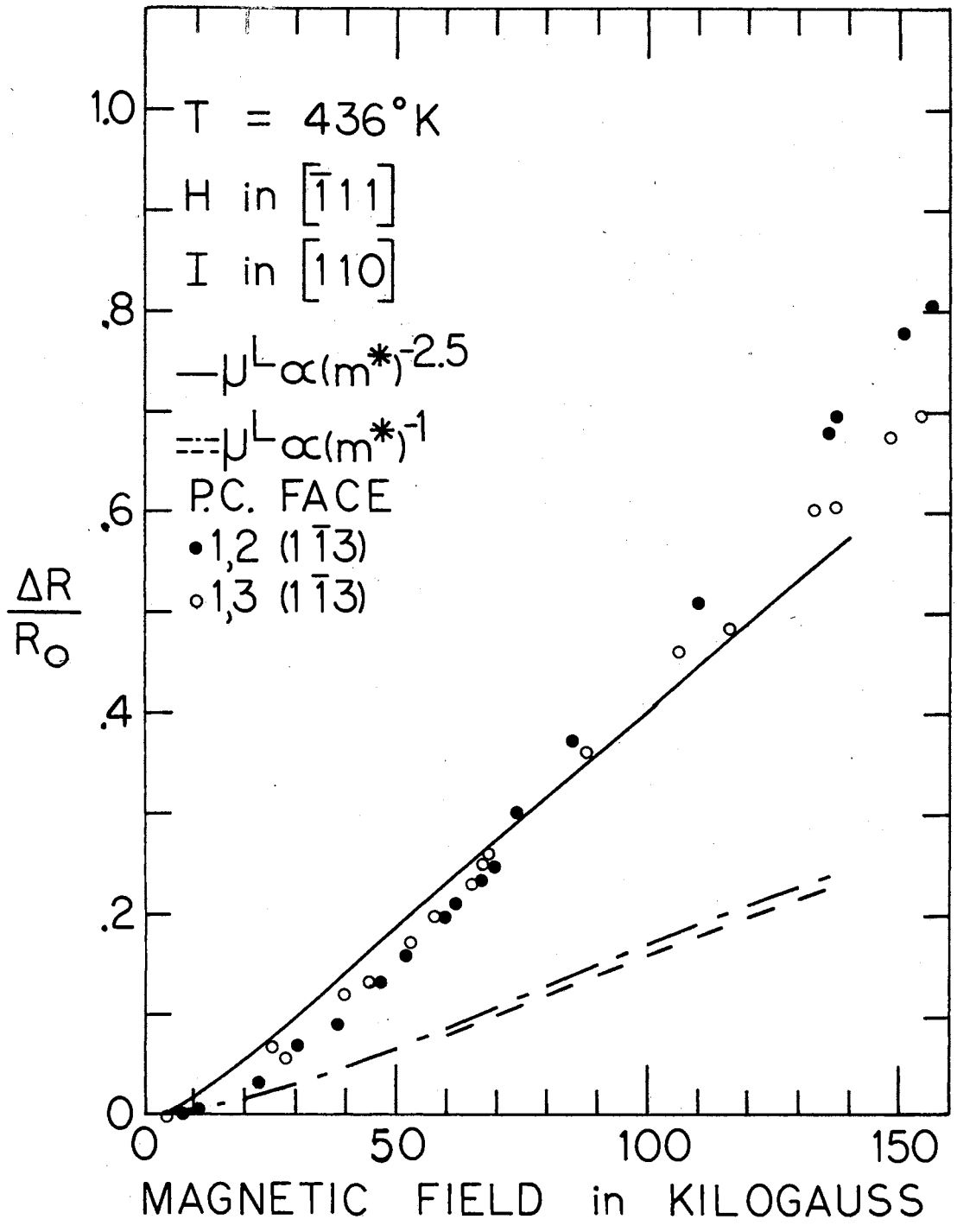

Figure 35. Transverse Magnetoresistance of DS-2 at 436°K with H in the [1̄11] and I in the [110] Directions

See Table VII for numerical parameters yielding theoretical results and Figure 19 for probe contact (P.C.) position.

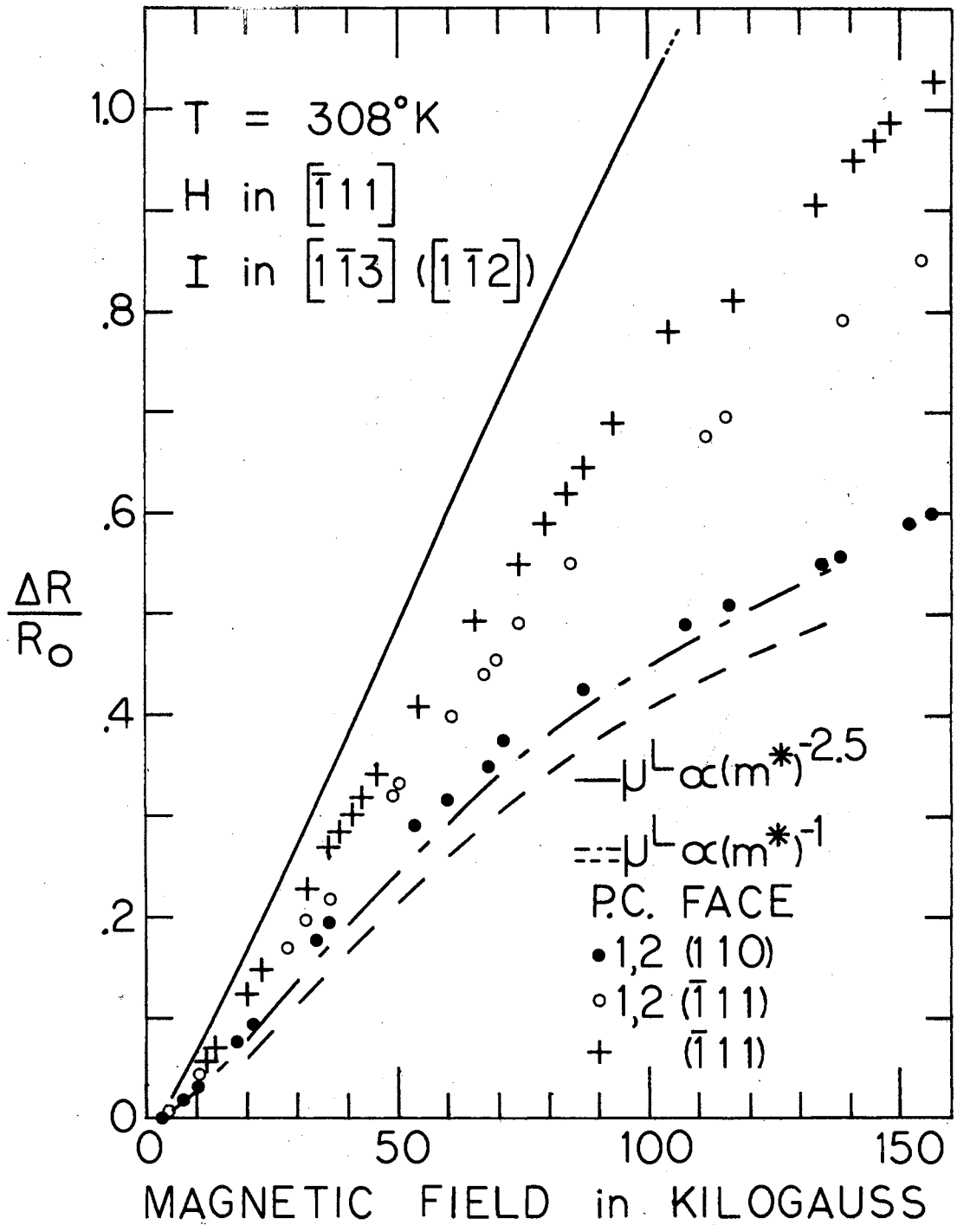

Figure 36. Transverse Magnetoresistance of DS-2 at 308°K with H in the [$\bar{1}$11] and I in the [1$\bar{1}$3] Directions

See Table VII for numerical parameters yielding theoretical results and Figure 19 for probe contact (P.C.) position.

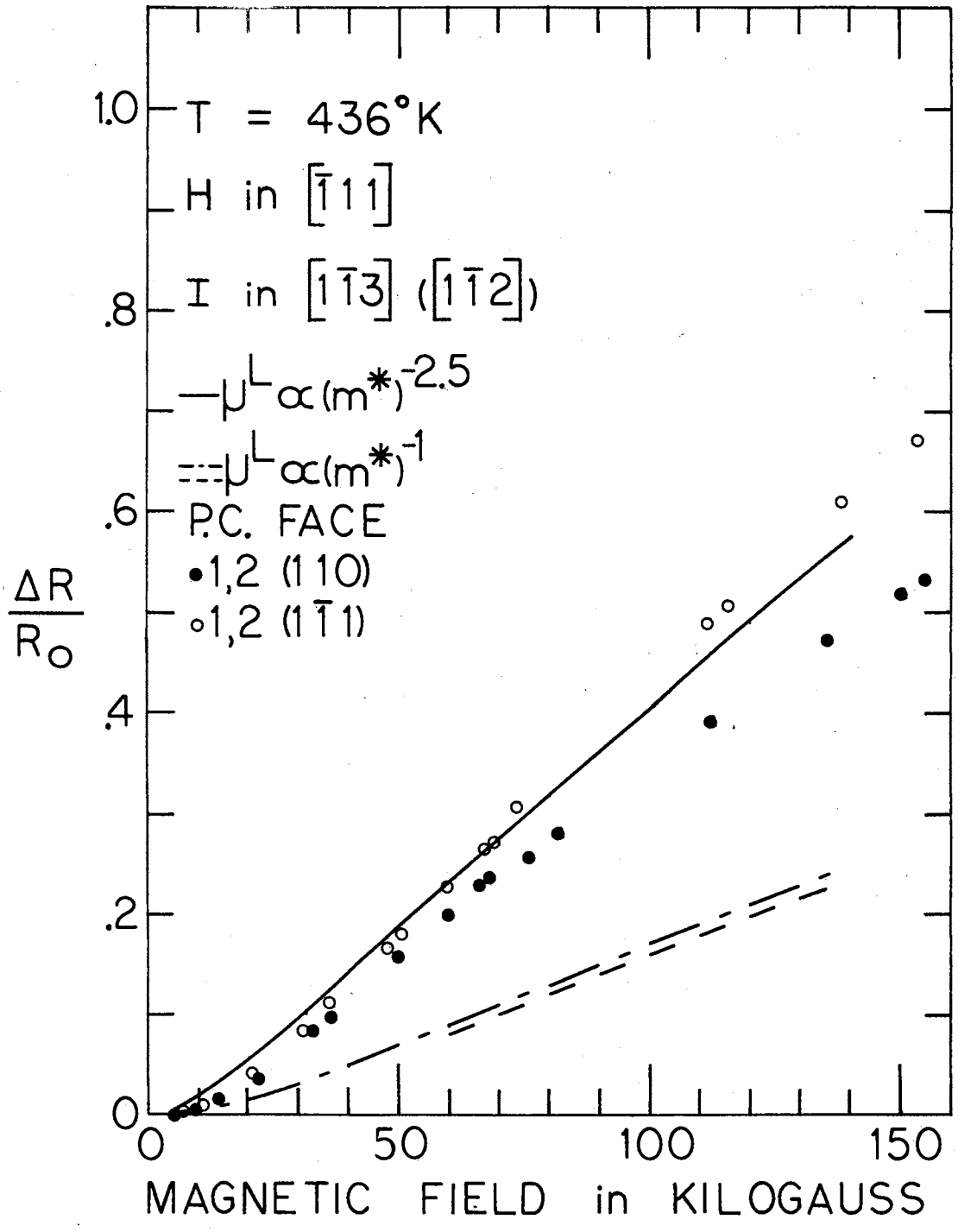

Figure 37. Transverse Magnetoresistance of DS-2 at 436°K with H in the [$\bar{1}$11] and I in the [1$\bar{1}$3] Directions

See Table VII for numerical parameters yielding theoretical results and Figure 19 for probe contact (P.C.) position.

Magnetoresistance: Magnetic Field Along the $[1\bar{1}3]$ Axis

With the electric current density directed along the $[1\bar{1}3]$ axis, the independent measurements of the longitudinal magnetoresistance at 308°K are shown in Figure 38. The single measurement of the longitudinal magnetoresistance at 436°K is shown in Figure 39. The difference between the sets of data in Figure 38 may be indicative of an inhomogeneous distribution of impurity atoms within the blue end of the diamond. The break in the solid dot data in Figure 38 is correlated with the method of producing the magnetic fields. The magnetoresistance is decreased by a factor of approximately 1.3 as the temperature of the diamond is raised from 308°K to 436°K.

Figures 40 and 41 illustrate respectively the transverse magnetoresistance at 308°K and 436°K for the case of the current along the $[1\bar{1}0]$ axis. In taking the data symbolized by the solid dots in Figure 40, it was noted that the quantity $E_{FIRH} - E_{FI}^{0}$ was negative for values of the magnetic field less than approximately 70 kilogauss and positive for higher fields. At the same time, the quantity $E_{RIRH} - E_{RI}^{0}$ was positive for magnetic fields less than approximately 70 kilogauss and negative for higher fields. At the higher temperature, $E_{FIRH} - E_{FI}^{0}$ was negative and field dependent for all values of the magnetic field; $E_{RIRH} - E_{RI}^{0}$ was positive and field dependent for all values of the field. This observation, as for similar observations for the two other orientations of the magnetic field, is associated with the current along the $[110]$ axis, the axis along which there should exist a gradient in the density of holes. Raising the temperature from 308°K to 436°K reduced the magnetoresistance by a factor of approximately 1.5.

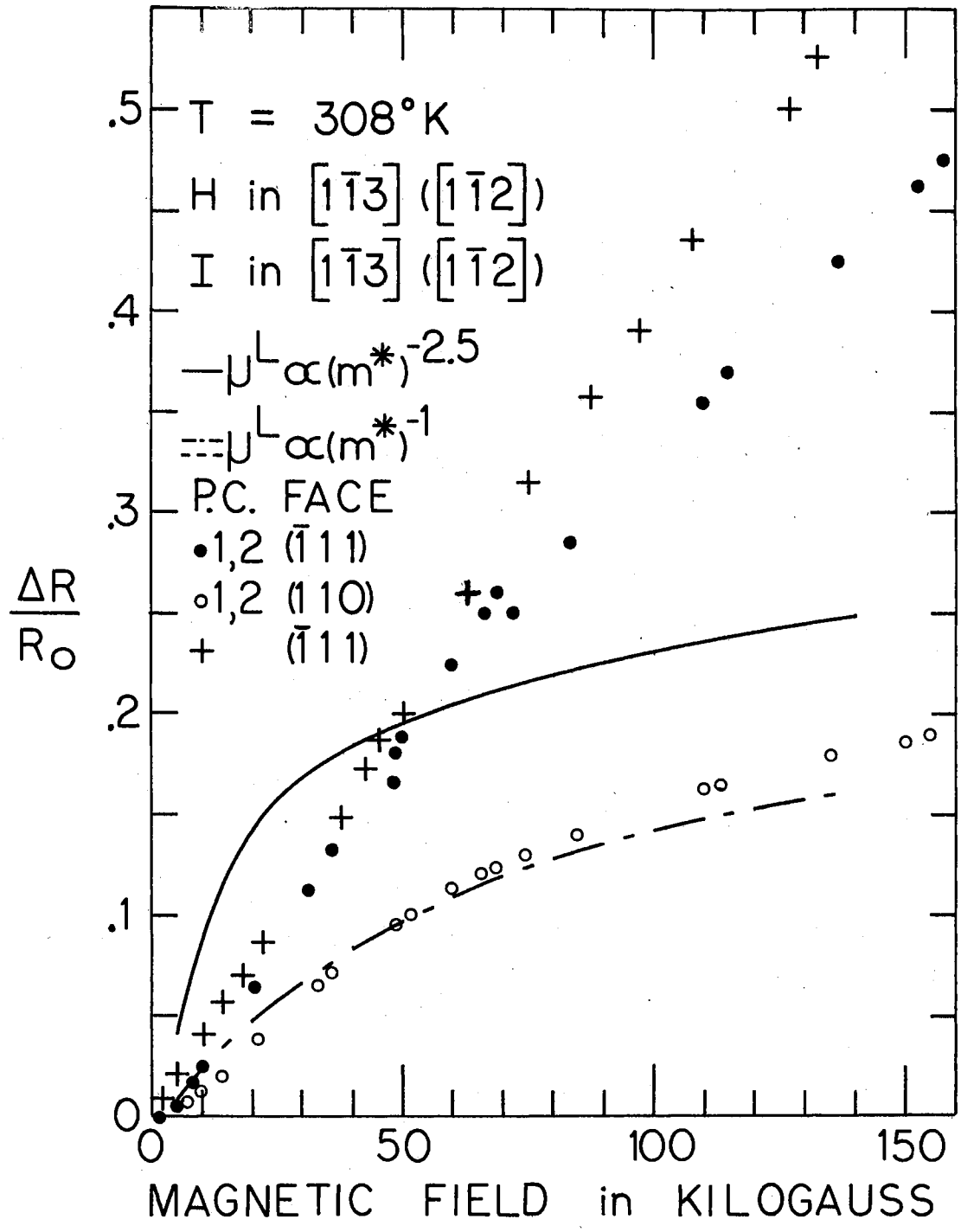

Figure 38. Longitudinal Magnetoresistance of DS-2 at 308°K in the [1$\bar{1}$3] Direction

See Table VII for numerical parameters yielding theoretical results and Figure 19 for probe contact (P.C.) position.

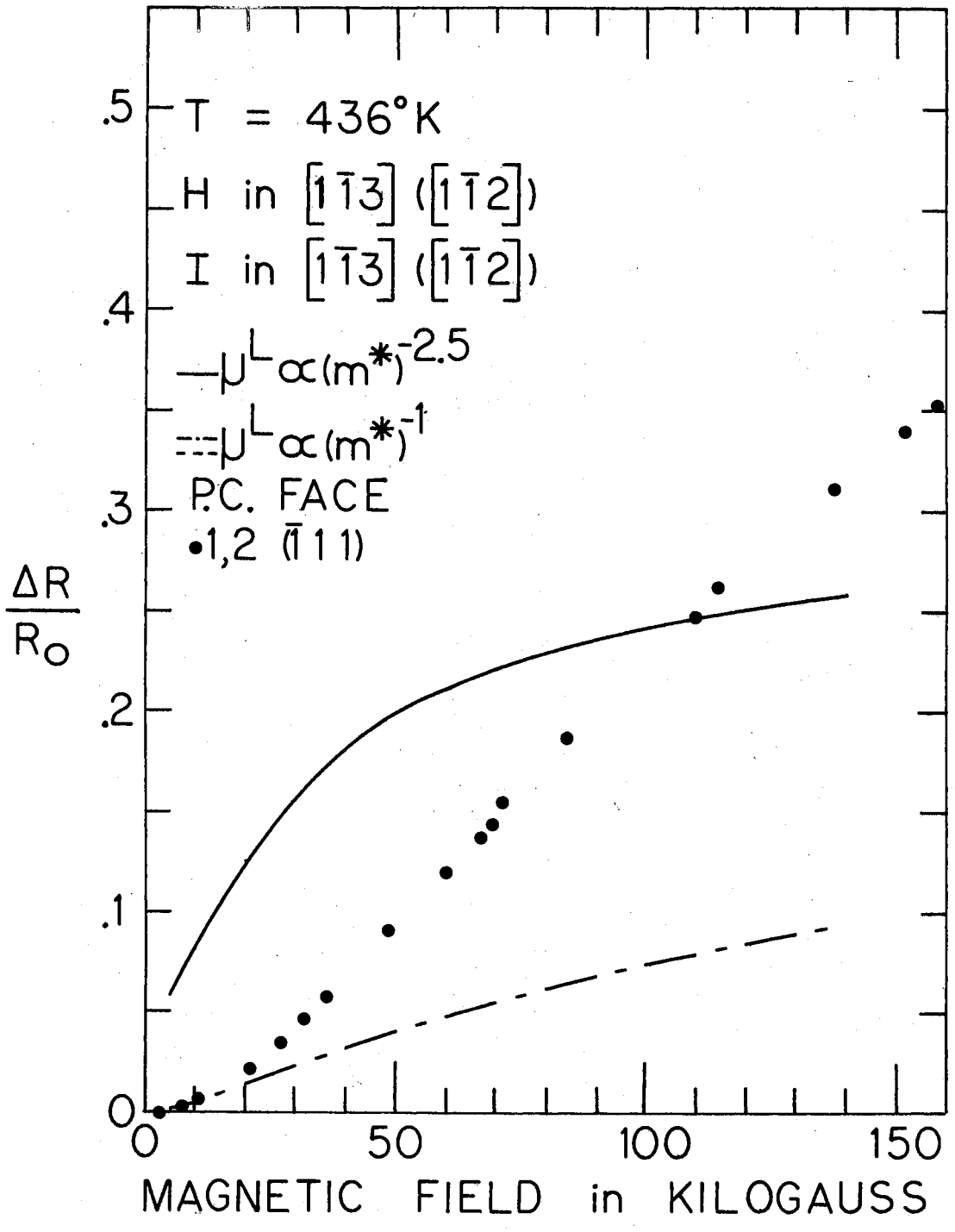

Figure 39. Longitudinal Magnetoresistance of DS-2 at 436°K in the [1 1̄ 3] Direction

See Table VII for numerical parameters yielding theoretical results and Figure 19 for probe contact (P.C.) position.

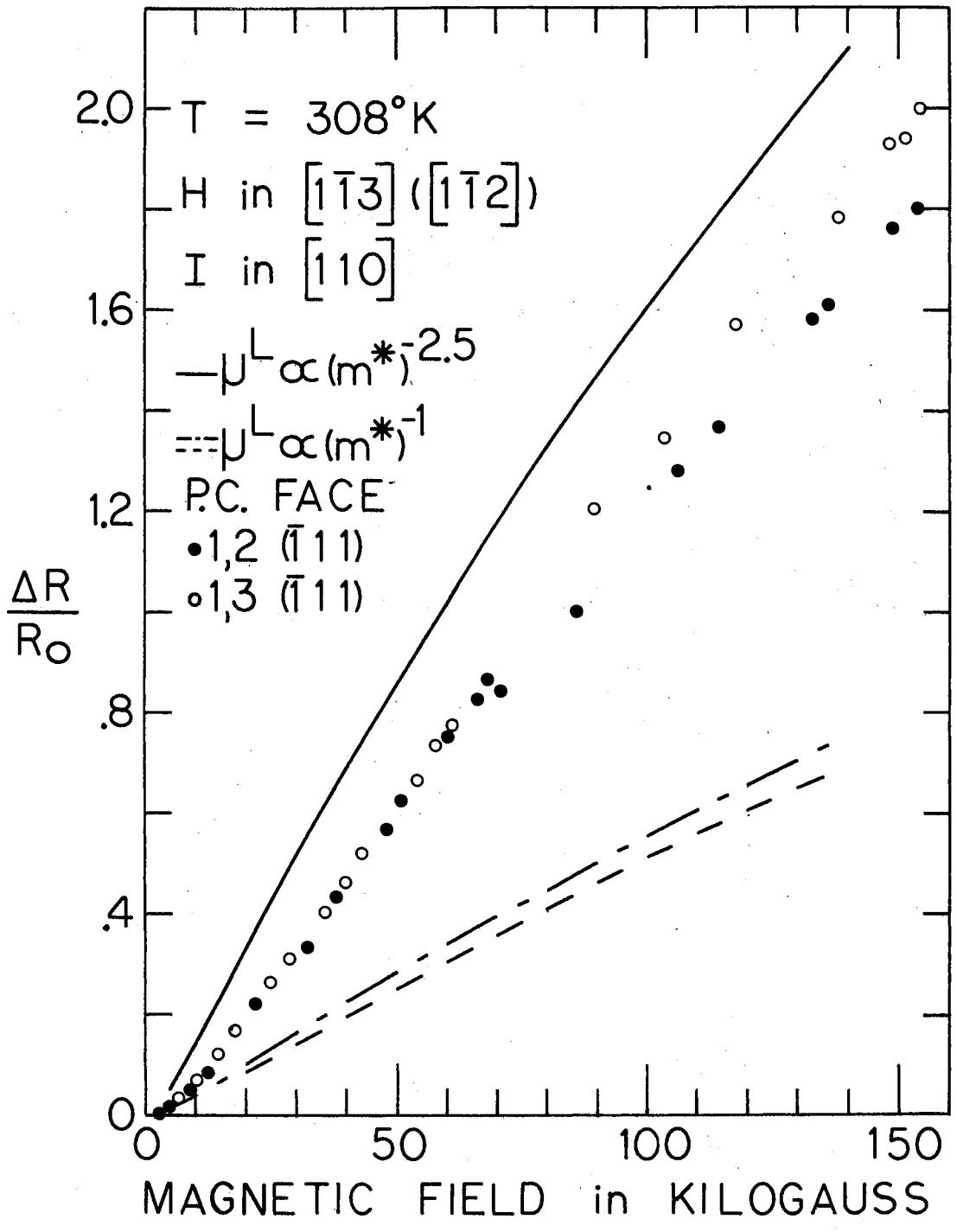

Figure 40. Transverse Magnetoresistance of DS-2 at 308°K with H in the [1$\bar{1}$3] and I in the [110] Directions

See Table VII for numerical parameters yielding theoretical results and Figure 19 for probe contact (P.C.) position.

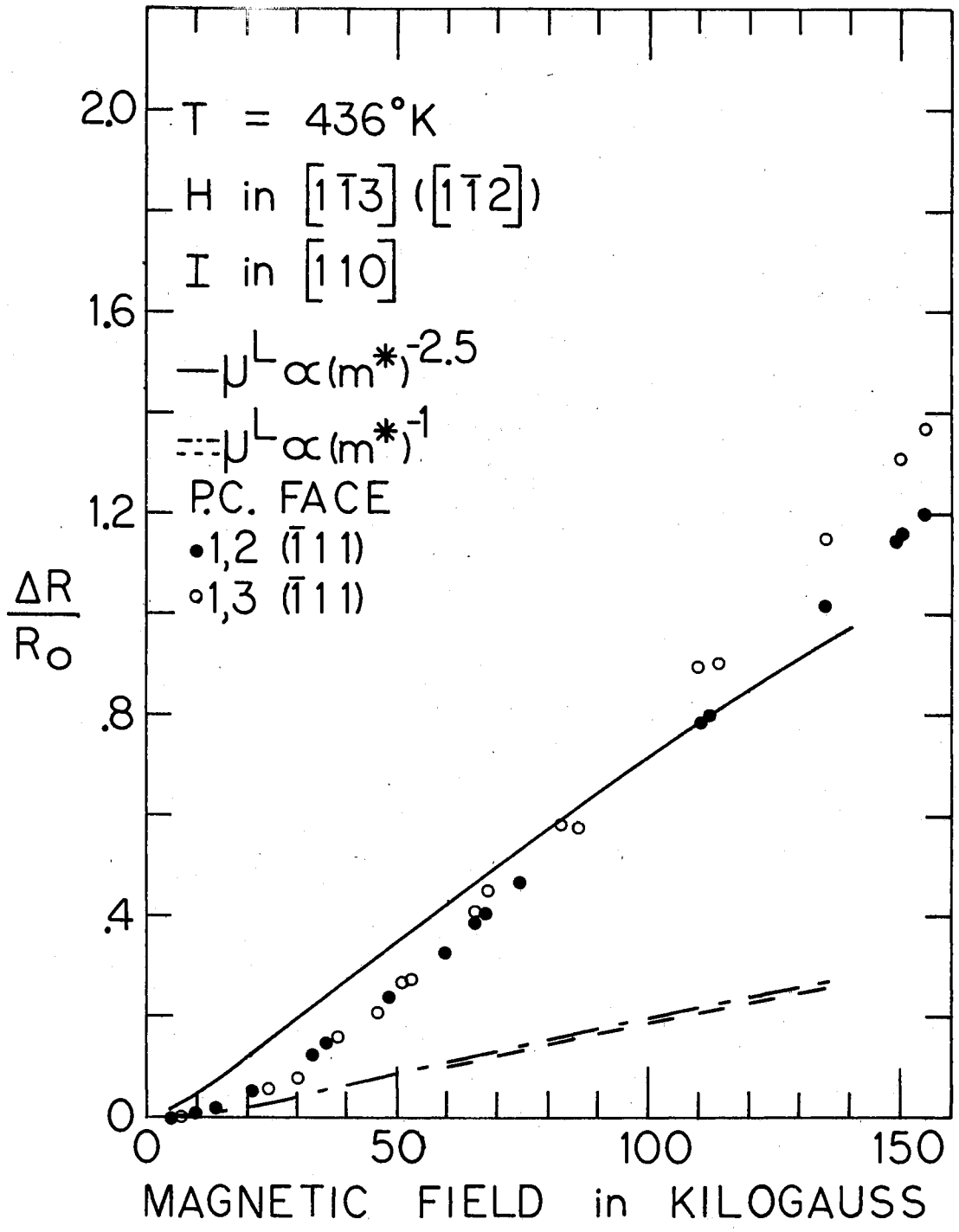

Figure 41. Transverse Magnetoresistance of DS-2 at 436°K with H in the [1$\bar{1}$3] and I in the [110] Directions

See Table VII for numerical parameters yielding theoretical results and Figure 19 for probe contact (P.C.) position.

The transverse magnetoresistances at 308°K and 436°K for the current density along the $[\bar{1}11]$ axis are shown respectively in Figures 42 and 43. The independent measurements were both made with magnetoresistance probe contacts; however, the data symbolized by circles were taken with the contacts on the $(1\bar{1}3)$ face of the diamond, which is perpendicular to the magnetic field. The shorting out of part of the Hall field by the contacts on the $(1\bar{1}3)$ face is reflected in the larger magnetoresistance recorded. The magnetoresistance is reduced by a factor of two in raising the temperature of the diamond from 308°K to 436°K.

A single measurement (solid dots) of the longitudinal magnetoresistance with both the electric current and the magnetic field directed along the $[1\bar{1}3]$ axis is shown in Figure 44. The electromagnet used was that capable of producing a 500 kilogauss magnetic field. As in the previous figures, the symbol "+" represents data taken by K. J. Russell (15). Notice that the magnetoresistance only indicates a tendency towards saturation; complete saturation may require fields on the order of 500 kilogauss.

Hall Effect: Magnetic Field Along the $[1\bar{1}0]$ Axis

In place of presenting the Hall coefficient as a function of the magnetic field, a related quantity called the Hall coefficient factor was calculated. The Hall coefficient factor $\frac{R_H}{R_{140}}$ of the diamond in a magnetic field of strength H is defined as the ratio of the Hall coefficient R_H of the diamond at that field to the Hall coefficient R_{140} of the diamond in a field of 140 kilogauss. The use of the Hall coef-

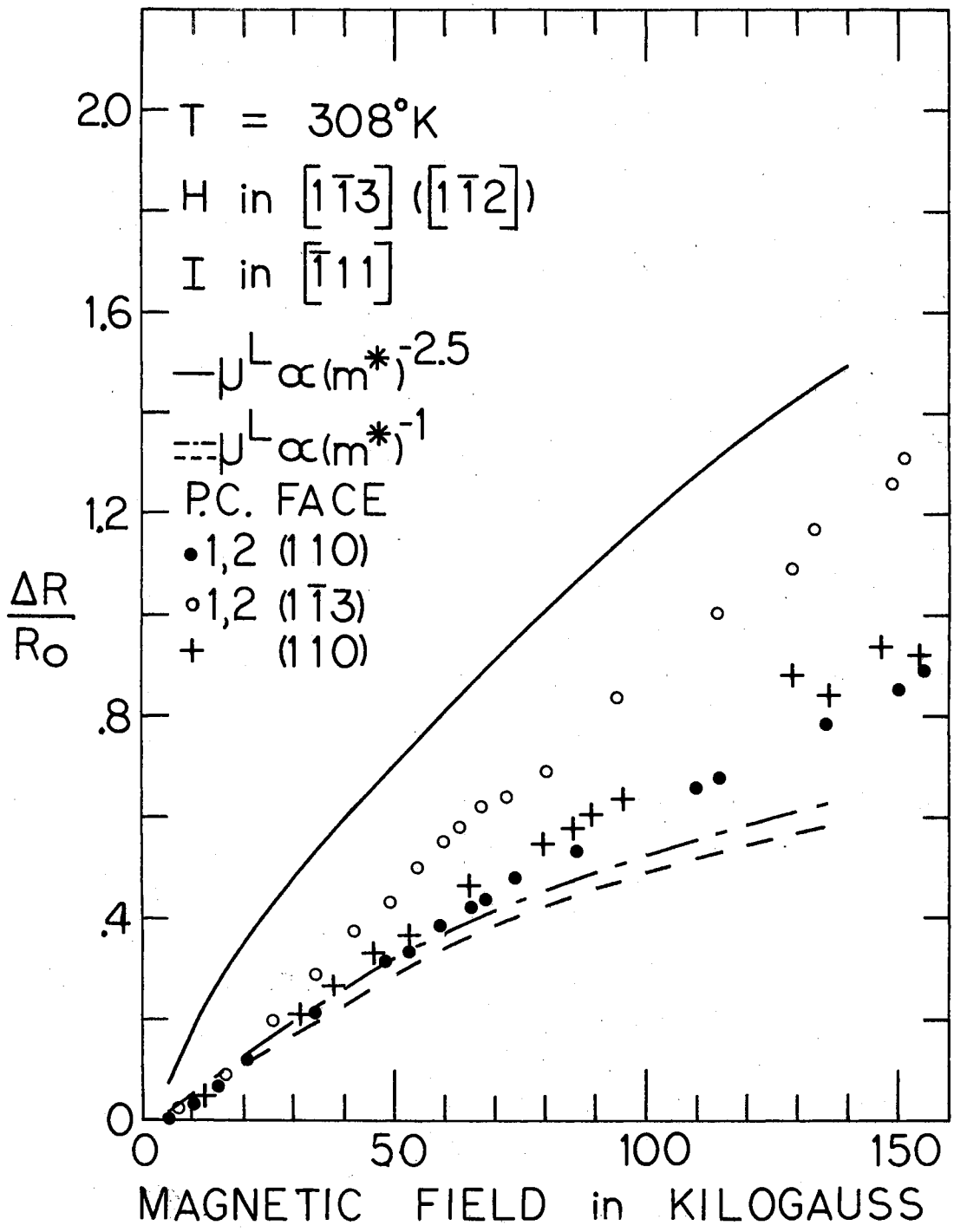

Figure 42. Transverse Magnetoresistance of DS-2 at 308°K with H in the [1$\bar{1}$3] and I in the [$\bar{1}$11] Directions

See Table VII for numerical parameters yielding theoretical results and Figure 19 for probe contact (P.C.) position.

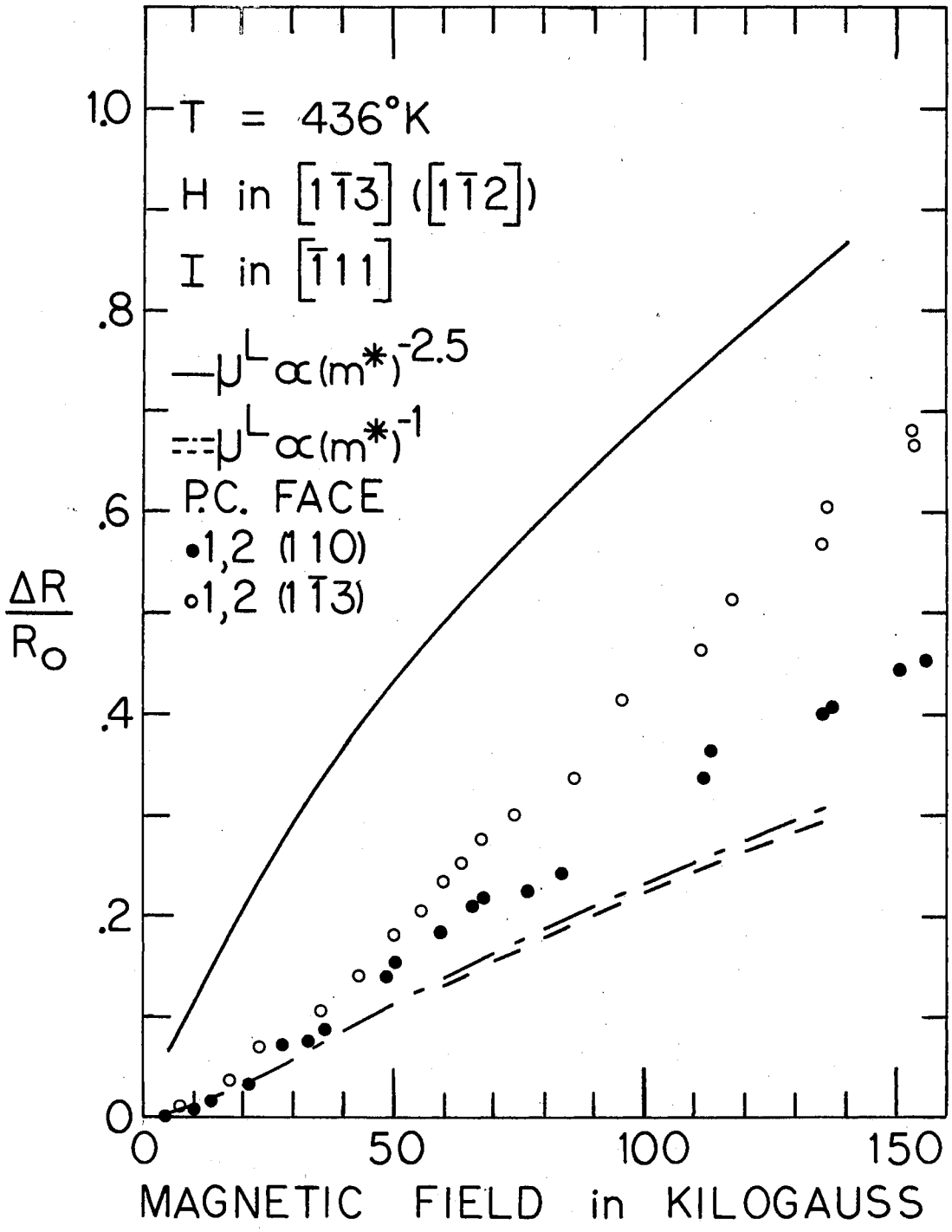

Figure 43. Transverse Magnetoresistance of DS-2 at 436°K with H in the [1$\bar{1}$3] and I in the [$\bar{1}$11] Directions

See Table VII for numerical parameters yielding theoretical results and Figure 19 for probe contact (P.C.) position.

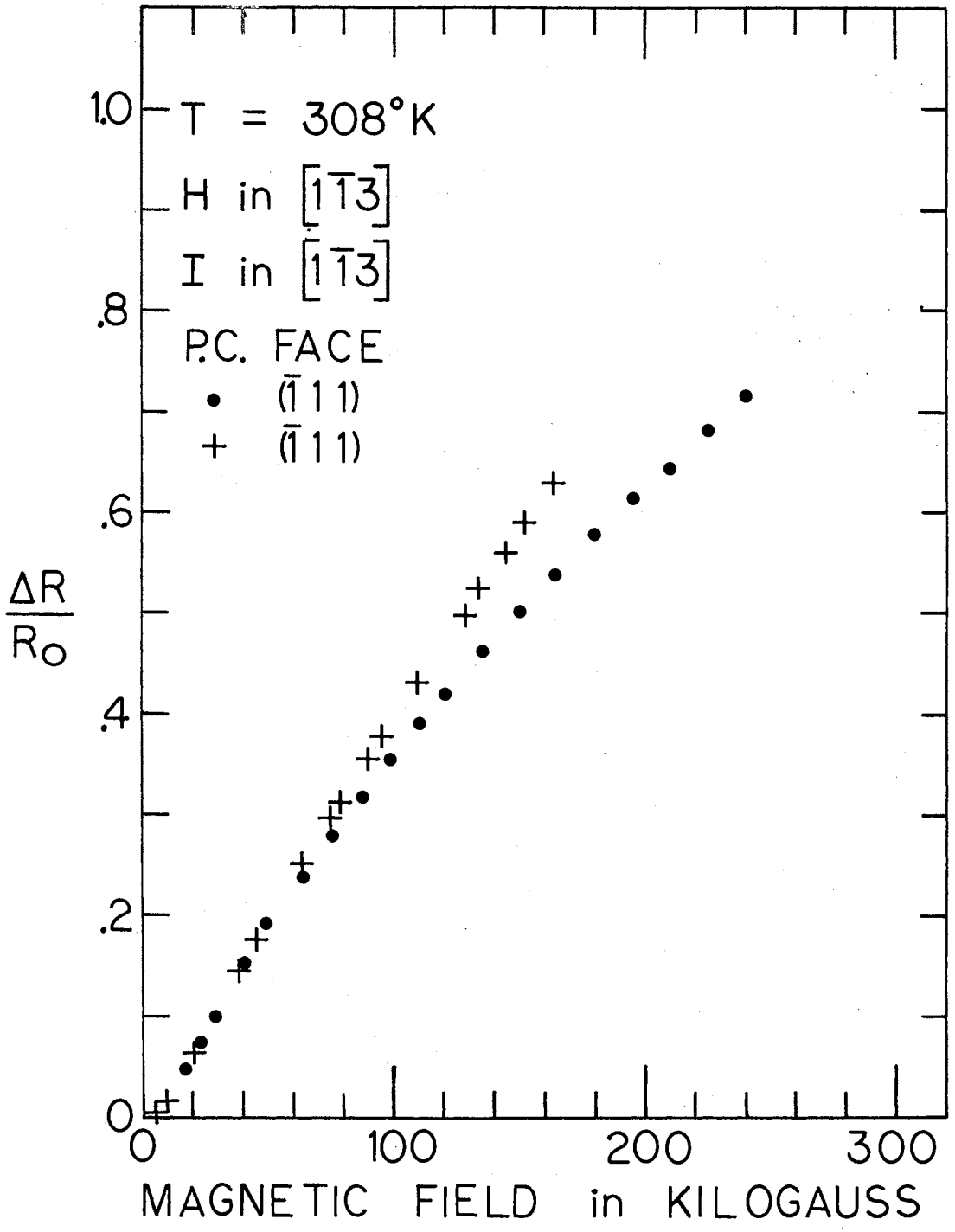

Figure 44. Longitudinal Magnetoresistance of DS-2 at 308°K in the [1$\bar{1}$3] Direction

The probe contact position is denoted by "P.C.".

ficient factor allows the magnetic field dependence of the various experimentally determined Hall coefficients to be emphasized. To compute the actual Hall coefficient, Table III is provided; it gives all of the measured Hall coeffficients at a magnetic field of 140 kilogauss along with the appropriate references to the Figure number and the symbol of the data. In the literature, the Hall coefficient factor in a magnetic field H is defined as the ratio of the Hall coefficient R_H at that field to the estimated saturation value of the Hall coefficient R_∞ in very large magnetic fields. Some of the Hall coefficient factor data of diamond does indicate a saturation value so that the Hall coefficient at 140 kilogauss would correspond to R_∞. No geometrical corrections were made to the data.

With the electric current density along the $[\bar{1}11]$ axis, the two independent measurements of the Hall coefficient factor at 308°K are shown in Figure 45. The single measurement of the Hall (coefficient) factor at 436°K is shown in Figure 46. All Hall factor data in this chapter symbolized by the circles were taken using the pair of Hall effect contacts #1 and #3 of Figure 19 (the pair of contacts positioned such as to be sensitive to both the Hall effect and the magnetoresistance). All Hall factor data show a correlation with the method of producing the magnetic field; this is seen by the breaks in the data at 11 and 70 kilogauss. This correlation makes it impossible to determine the Hall factor in the limit of vanishing magnetic field. Both sets of data in Figure 45 indicate that the Hall coefficient increases with increasing magnetic field and has not saturated even in fields of 160 kilogauss. This type of field dependence was first observed by R. T. Bate and R. K. Willardson (9). They use fields up

TABLE III

HALL COEFFICIENT DATA

R_{140} m^3/coulomb	Data Symbol	Figure
1.24×10^{-1}	dot	45
1.06×10^{-1}	circle	45
3.17×10^{-3}	circle	46
1.30×10^{-1}	dot	47
1.35×10^{-1}	circle	47
5.10×10^{-3}	circle	48
5.66×10^{-2}	dot	49
8.64×10^{-2}	circle	49
2.87×10^{-3}	circle	50
5.28×10^{-2}	dot	51
6.77×10^{-2}	circle	51
3.48×10^{-3}	circle	52

to 20 kilogauss and did not observe a saturation of the Hall coefficient. Since there is a geometrical increase in the Hall coefficient with increasing magnetic field (which becomes more prominent for samples with a length to width ratio less than one) and since the length to width ratio for this particular orientation of DS-2 is less than one, it is possible that the large field behavior of the Hall factor data is a purely geometrical effect. In Figure 46, the Hall factor increases with increasing field and shows almost a complete saturation at 150 kilogauss. The solid line, long-dash-short-dash line, and the short-dash are the results of theoretical calculations which will be discussed in Chapter V.

Figures 47 and 48 respectively illustrate the Hall coefficient factor at 308°K and 436°K for the case of the current along the $[1\bar{1}3]$ axis. The data at 308°K indicate that the Hall coefficient increases with increasing magnetic field (up to about 40 kilogauss), and then decreases for fields larger than 65 kilogauss. At 436°K, the Hall factor increases with increasing magnetic field up to about 100 kilogauss and remains constant for higher fields.

Hall Effect: Magnetic Field Along the $[\bar{1}11]$ Axis

The Hall coefficient factors at 308°K and 436°K for the current density along the [110] axis are shown respectively in Figures 49 and 50. The data symbolized by the solid dots do indicate that the Hall factor increases with increasing field, reaches a maximum between 50 and 70 kilogauss, and decreases with higher magnetic fields. At 436°K, the Hall factor increases with increasing field and saturates at about 80 kilogauss.

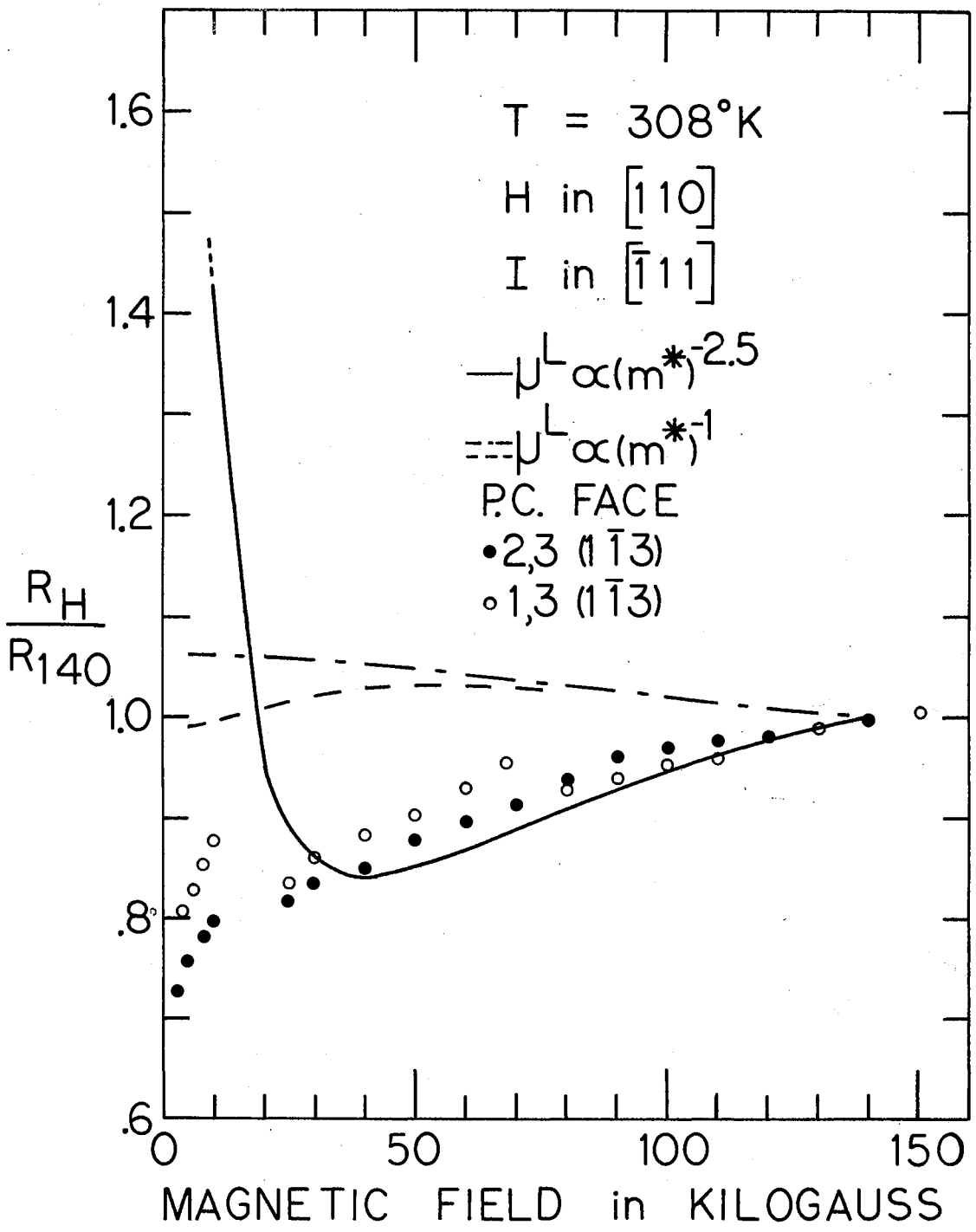

Figure 45. Hall Coefficient Factor of DS-2 at 308°K with H in the [110] and I in the [1̄11] Directions

See Table VII for numerical parameters yielding theoretical results and Figure 19 for probe contact (P.C.) position.

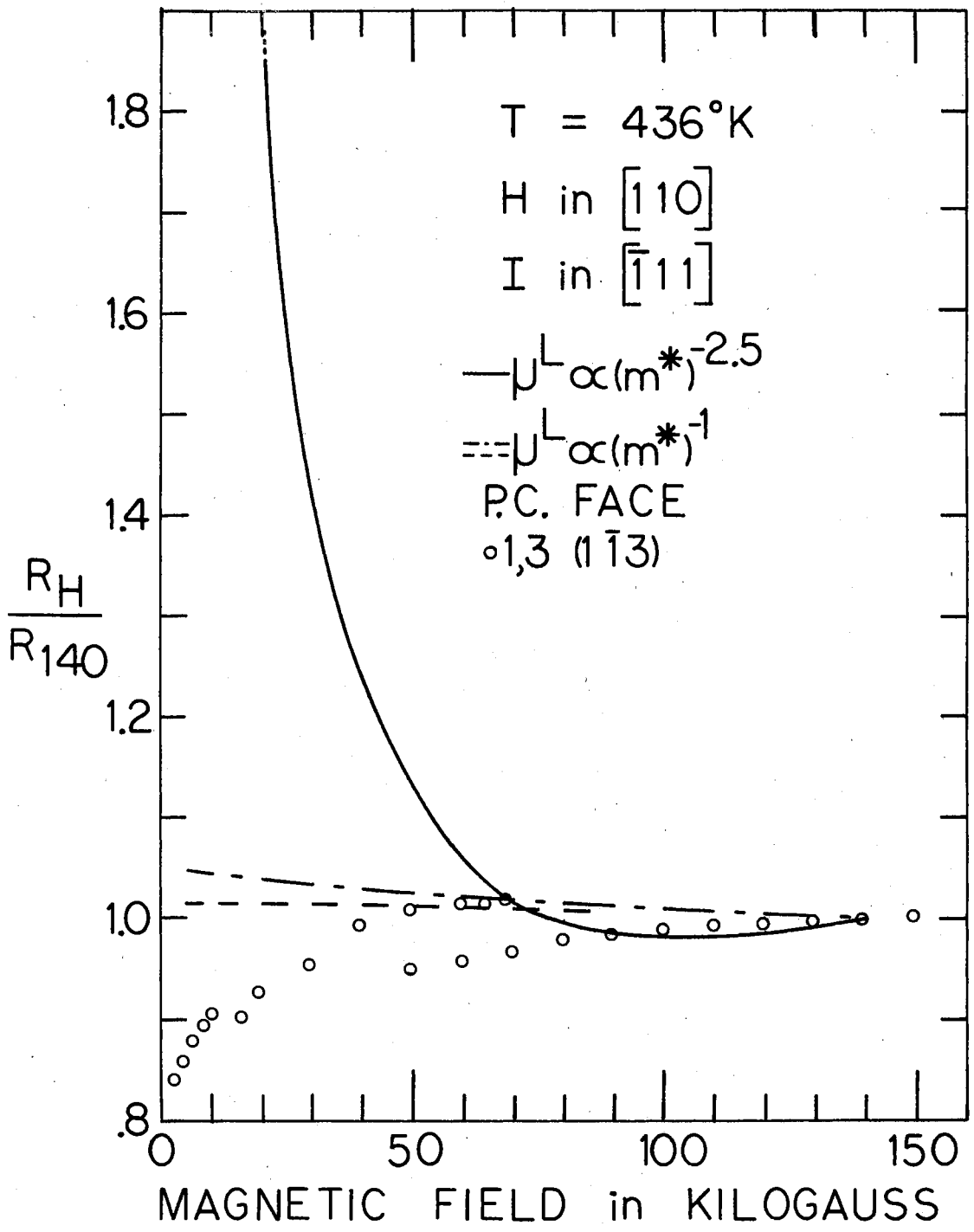

Figure 46. Hall Coefficient Factor of DS-2 at 436°K with H in the [110] and I in the [1̄11] Directions

See Table VII for numerical parameters yielding theoretical results and Figure 19 for probe contact (P.C.) position.

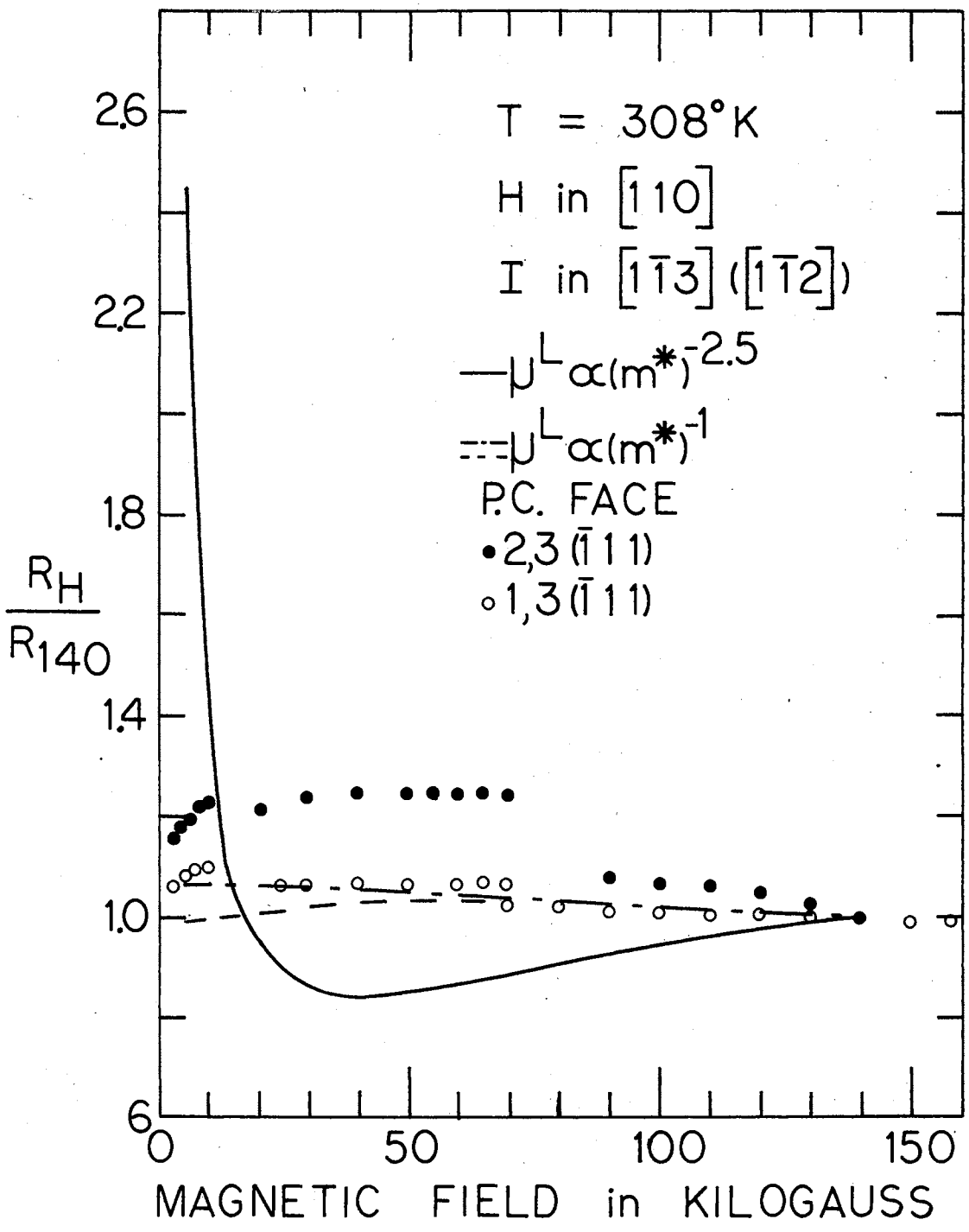

Figure 47. Hall Coefficient Factor of DS-2 at 308°K with H in the [110] and I in the [1$\bar{1}$3] Directions

See Table VII for numerical parameters yielding theoretical results and Figure 19 for probe contact (P.C.) position.

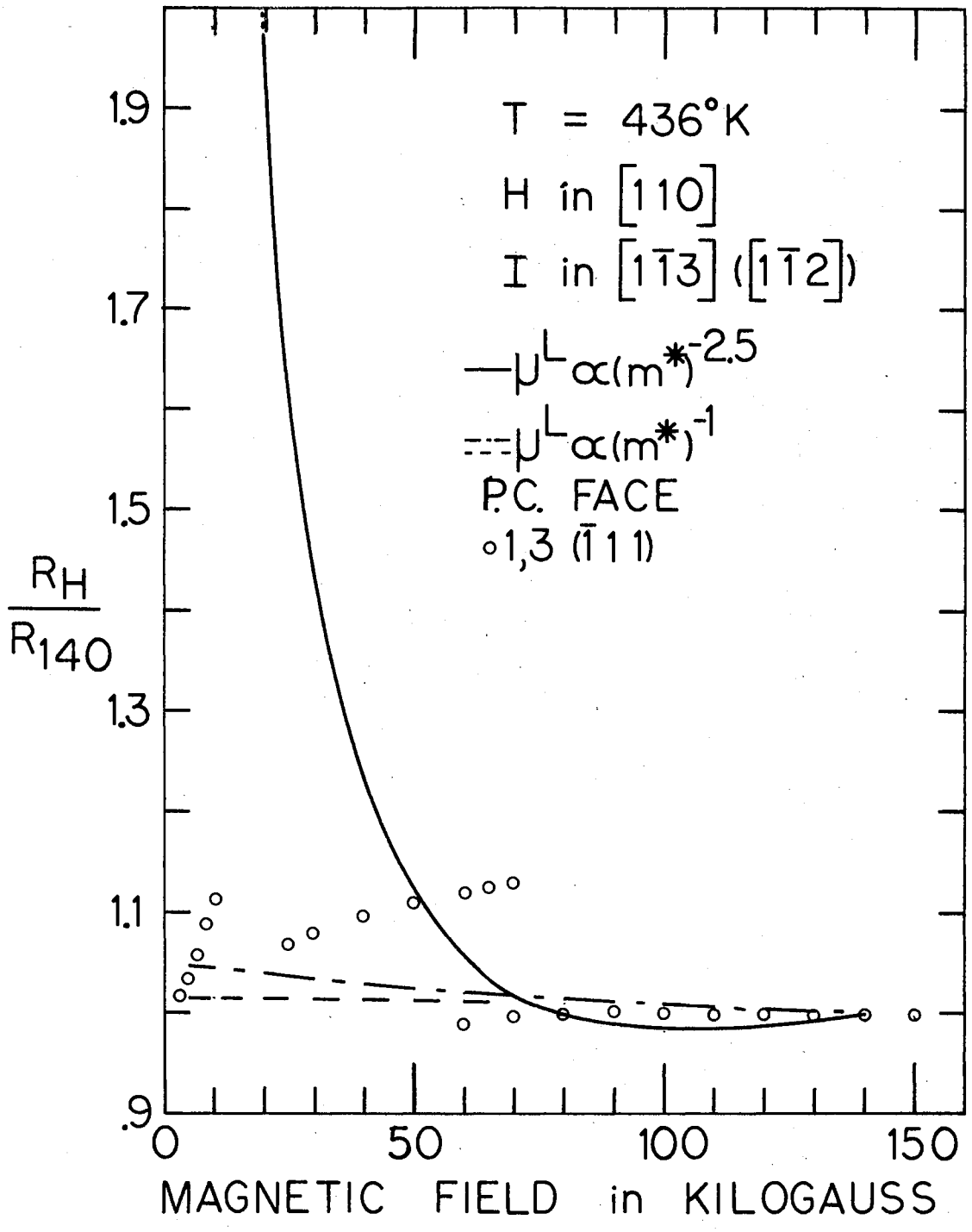

Figure 48. Hall Coefficient Factor of DS-2 at 436°K with H in the [110] and I in the [1$\bar{1}$3] Directions

See Table VII for numerical parameters yielding theoretical results and Figure 19 for probe contact (P.C.) position.

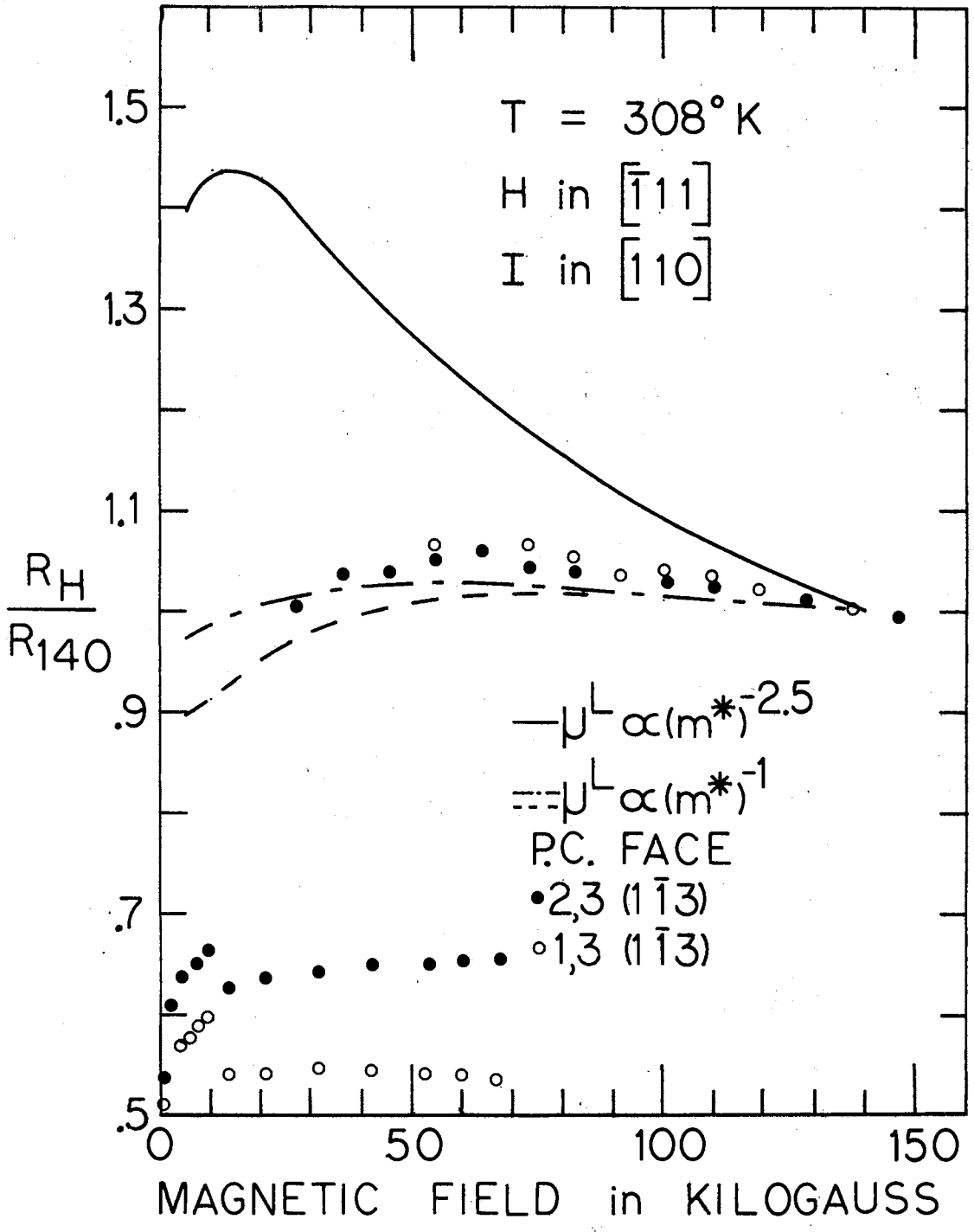

Figure 49. Hall Coefficient Factor of DS-2 at 308°K with H in the [1̄11] and I in the [110] Directions

See Table VII for numerical parameters yielding theoretical results and Figure 19 for probe contact (P.C.) position.

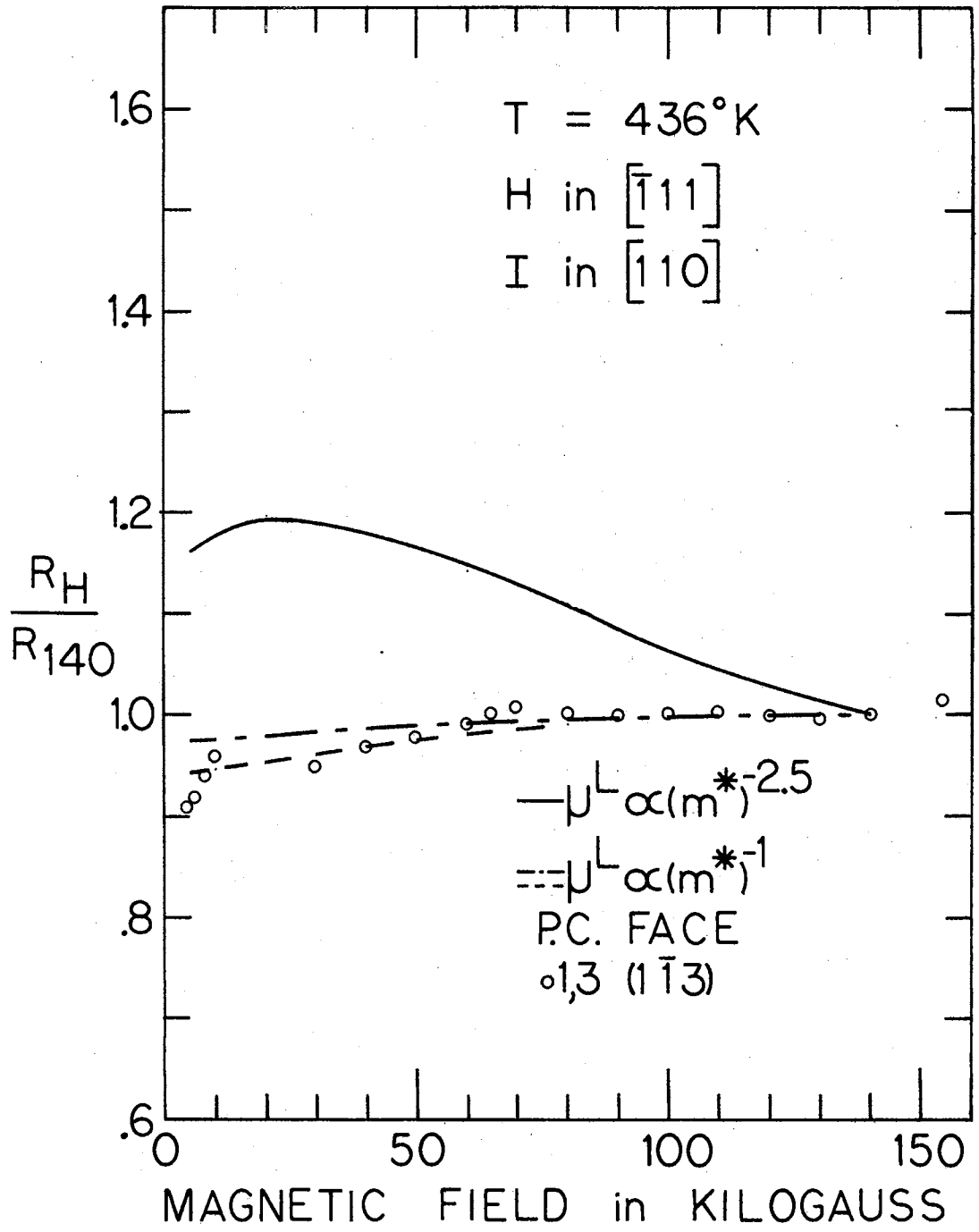

Figure 50. Hall Coefficient Factor of DS-2 at 436°K with H in the [1̄11] and I in the [110] Directions

See Table VII for numerical parameters yielding theoretical results and Figure 19 for probe contact (P.C.) position.

Hall Effect: Magnetic Field Along the [1$\bar{1}$3] Axis

With the electric current density along the [110] axis, the two independent measurements of the Hall coefficient factor at 308°K are shown in Figure 51. The single measurement at 436°K is shown in Figure 52. The data symbolized by the circles in Figure 51 indicate that the Hall factor increases with increasing magnetic field, reaches a maximum between 20 and 30 kilogauss, and then decreases with further increase in field. On the other hand, the data symbolized by the solid dots remain approximately constant for magnetic fields above 70 kilogauss. At 436°K, the Hall factor increases with increasing field and does not appear to saturate in the large magnetic fields.

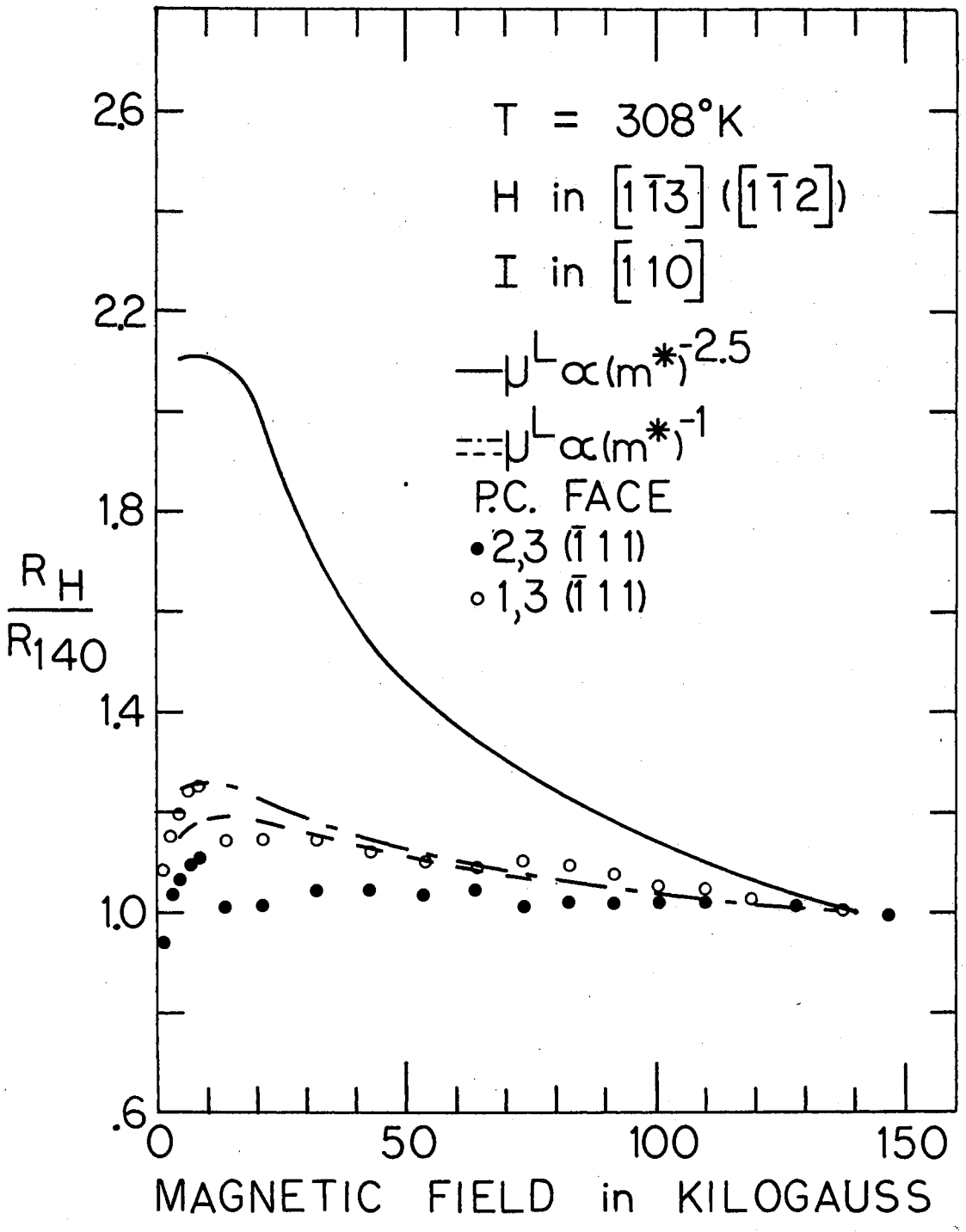

Figure 51. Hall Coefficient Factor of DS-2 at 308°K with H in the [1$\bar{1}$3] and I in the [110] Directions

See Table VII for numerical parameters yielding theoretical results and Figure 19 for probe contact (P.C.) position.

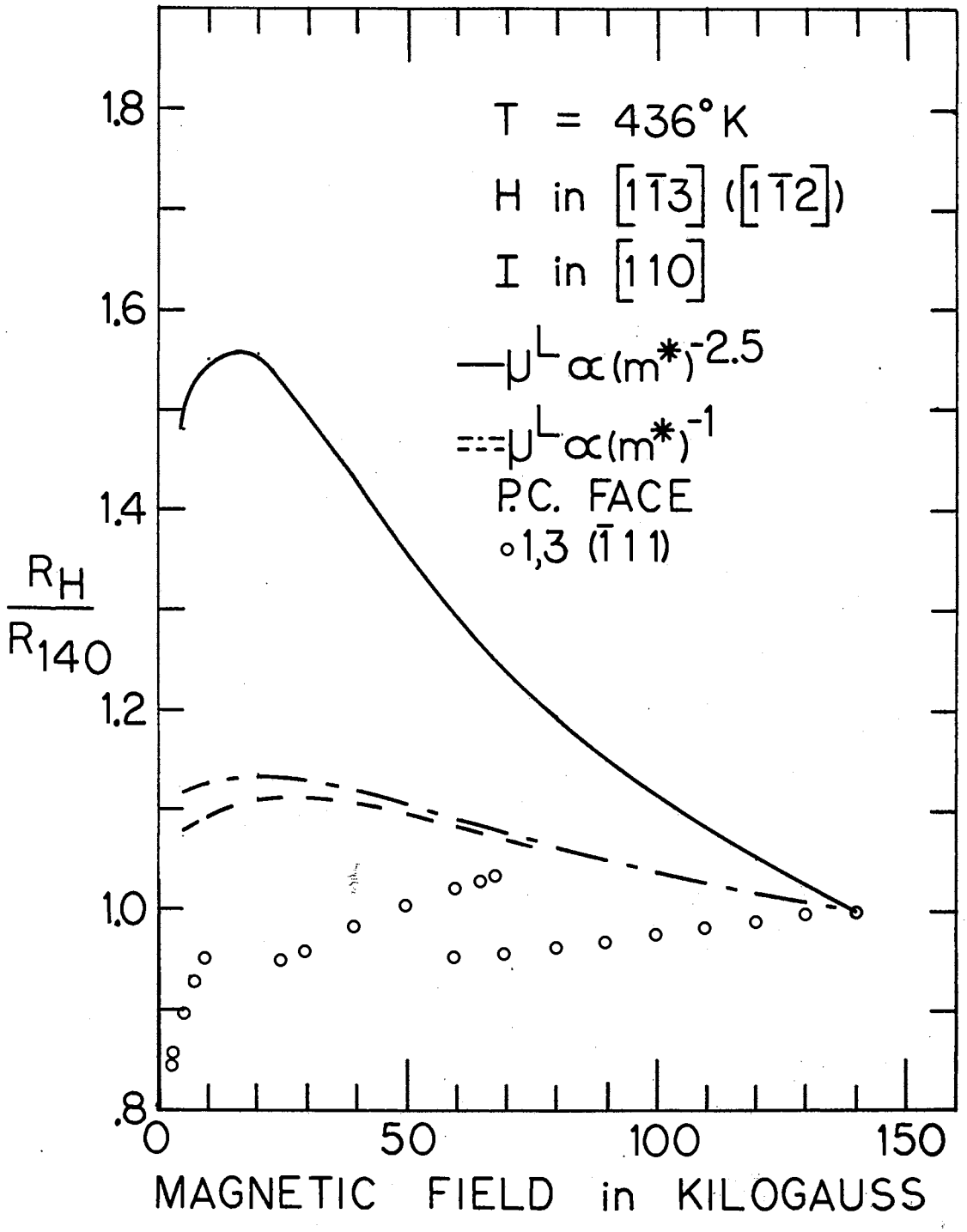

Figure 52. Hall Coefficient Factor of DS-2 at 436°K with H in the [1$\bar{1}$3] and I in the [110] Directions

See Table VII for numerical parameters yielding theoretical results and Figure 19 for probe contact (P.C.) position.

CHAPTER V

INTERPRETATION OF RESULTS

Type of Approach

In determining the magnetoresistance of the blue end of DS-2, the current density in the diamond was forced to be approximately independent of the resistivity of the diamond, and the change in the electric field within the diamond, applied by the external power supply, was detected. Under the same experimental arrangement, the Hall field due to the redistribution of the electrical charge within the diamond was detected by the Hall effect probe contacts, and the Hall coefficient was computed. These statements illustrate that the measured quantities are related to the elements of the resistivity tensor.

In contrast to this, it is easier, from a theoretical viewpoint, to determine the change in the current density in the diamond for a constant electric field between the current electrodes. The computed quantities are the elements of the magnetoconductivity tensor. Since the conductivity and resistivity tensors are the inverses of one another, it is a simple matter to express the magnetoresistance and the Hall coefficient of the diamond in terms of the components of the magnetoconductivity tensor. The parameters describing the transport of holes in the diamond lattice environment and used in determining the components of the magnetoconductivity tensor are not related to the measured galvanomagnetic properties by simple expressions. As a result,

the experimental data is not extensively used in directly determining the transport properties of the holes but principally serves as a testing ground for the assumptions which must be made.

The positive sign of the Hall coefficient is indicative that conduction in DS-2 is primarily due to holes. The assumption that conduction is due to three types of holes in which each type is associated with one of the three uppermost valence energy bands of diamond, and that the energy bands are uncoupled is reflected in the three uncoupled Boltzmann transport equations which were solved. The solution of the Boltzmann transport equation is simplified if the concept of a relaxation time is applicable; assumptions implied by this approximation are delineated in an article written by M. Dresden (34). The elements of the magnetoconductivity tensor are expressed in a form developed by J. W. McClure (35): the contribution to the conductivity from a surface of constant energy was expressed in a Fourier series in harmonics of the cyclotron motion of the charge carriers about hodographs in the energy surface. This required that specific shapes be assumed for the constant energy surfaces associated with the energy near the tops of the valence bands. The constant energy surfaces of the heavy hole valence band (valence band associated with the largest average effective mass) were cubes, that of the light hole valence band (associated with the smallest average effective mass) were octahedrons, and the split-off valence band was composed of spherical energy surfaces. The effective masses of the holes were taken to be $m_H = 2.12\ m_0$ (H for heavy hole), $m_L = 0.7\ m_0$ (L for light hole), and $m_S = 1.06\ m_0$ (S for split-off hole) as determined by C. J. Rauch (36), where m_0 is the mass of a free electron. The heavy and light holes are assumed to belong to

the two valence bands which are degenerate at the center of the Brillouin zone. The split-off hole is assumed to belong to the valence band whose degeneracy at the center of the Brillouin zone is removed by the inclusion of spin-orbit interaction. This energy band is called the split-off band, and the spin-orbit splitting is taken to be 0.006 electron volts (36). The relaxation time of the holes was assumed to be dependent only on the energy of the charge carriers and was composed of the independent contributions of the longitudinal acoustical vibrations of the diamond lattice and ionized impurities within the diamond. The strength of the ionized impurity scattering as compared to the phonon scattering was determined for each band by the mixed scattering parameter β; several values of this parameter were used. The resulting explicit expressions for the elements of the magnetoconductivity tensor were combined to yield the various magnetoresistivities and Hall coefficient factors. The results of the calculations were plotted along with the data.

Development of the Magnetoconductivity Tensor

J. W. McClure (35) developed an expression for the magnetoconductivity tensor assuming the applicability of the Boltzmann transport equation, the existence of a relaxation time, and the dependence of the relaxation time only on the energy of the charge carriers. The essence of the development is the recognition that in the presence of an externally applied magnetic field, and in the absence of an externally applied electric field, the component of the crystal momentum of the charge carrier in the direction of the magnetic field (z-axis) and the energy of the charge carrier are conserved. In the absence of scatter-

ing, the curve in momentum space traced out by the wave vector of the carrier is a closed path determined by the intersection of the plane normal to the magnetic field with a constant energy surface. This closed path is called a hodograph. An externally applied electric field will distort the trajectory of the hole from that of a closed path lying in a plane; however, for weak electric fields, M. Dresden (34) has shown that it is a good approximation to consider the trajectory as closed (the approximation is better as the strength of the magnetic field increases).

Recognizing that the motion of the crystal momentum along the hodograph was a periodic function of time with the cyclotron frequency ω, the group velocity of the wave packet associated with the hole (velocity of the hole) was expanded in a Fourier series in harmonics of ω. After assuming that the relaxation time τ was only dependent on energy, a single valued solution of the linearized Boltzmann equation (linearly dependent on the electric field) was found (35). This solution is the distribution function of the holes associated with a particular valence band and immediately leads to the following expression for $\sigma_{ij}(H)$, the ij th component of the magnetoconductivity tensor:

$$\sigma_{ij}(H) = 2\left(\frac{1}{2\pi}\right)^3 \int_{B.Z.} e^2\left[-\frac{\partial}{\partial \mathcal{E}} f_0(\mathcal{E})\right] \tau S_{ij} \vec{dk} \qquad \begin{matrix} i = 1,2,3 \\ j = 1,2,3 \end{matrix} \tag{9}$$

The electrical charge e of the hole is $+1.6 \times 10^{-19}$ coulomb; the energy of the hole $\mathcal{E}$ is measured downward from the top of the valence band; τ is the relaxation time; and the integral is to be taken over the first Brillouin zone (B.Z.) of reciprocal space. The equilibrium

distribution function of the hole $f_0(\mathcal{E})$ is approximated by the classical distribution function. The components of the tensor S are

$$S_{ii} = \left|V_i(0)\right|^2 + 2\sum_{m=1}^{\infty} \frac{\left|V_i(m)\right|^2}{1 + m^2\omega^2\tau^2} \qquad i = 1,2,3 \ , \tag{10}$$

and

$$S_{ij} = \sum_{m=0}^{\infty} \frac{V_i(m)V_j(-m) + V_i(-m)V_j(m)}{1 + m^2\omega^2\tau^2} + im\omega\tau \frac{V_i(-m)V_j(m) - V_i(m)V_j(-m)}{1 + m^2\omega^2\tau^2} \qquad \begin{matrix} i = 1,2,3 \\ j = 1,2,3 \\ i \neq j \end{matrix} \ . \tag{11}$$

The quantity $V_i(m)$ is the i th component of the m th Fourier coefficient in the expansion of the velocity of the hole V in a Fourier series in harmonics of the cyclotron frequency. The frequency ω is determined from its basic definition in terms of a line integral along the hodograph:

$$\frac{1}{\omega} = \frac{\hbar c}{2\pi eH} \oint \frac{\hat{dk}}{V_\perp} \ . \tag{12}$$

Planck's constant divided by 2π is symbolized by $\hbar$; c is the speed of light; and $\hat{dk}$ is the element of arc length along the hodograph. The speed of the hole in the plane of the hodograph at the point where the line integral is being evaluated is denoted by $V_\perp$.

Thus, to compute the components of the magnetoconductivity tensor, both the energy dependence of the relaxation time and the components of the tensor S must be known. For this reason, the shapes of the constant energy surfaces of diamond and particular mechanisms to scatter the holes had to be assumed.

The author's choice of representing the surfaces of constant

energy by plane faced surfaces is based upon several thoughts. Plane faced energy surfaces lend themselves to easy visualization; the velocity of the holes at all points of the surface (except edges and corners) is known. The ease with which the geometrical details of the hodographs can be mathematically described aids the computations of the Fourier coefficients of the velocity of the charge carrier $\vec{V}(m)$, the cyclotron frequency, and the components of the tensor S. The specific choice of representing the surfaces of the heavy hole band by cubes, the light hole band by octahedrons, and the split-off band by spheres is based on a study of the well known mathematical description of the constant energy surfaces of the diamond-like materials germanium and silicon. G. Dresselhaus, A. F. Kip, and C. Kittel (37) have shown that at temperatures around $4^{o}K$ and for energies not too far from the center of the Brillouin zone the surfaces of constant energy satisfy the relations

$$\mathcal{E}(k) = Ak^2 \pm \left[B^2k^4 + C^2(k_x^2k_y^2 + k_y^2k_z^2 + k_z^2k_x^2)\right]^{\frac{1}{2}} ,$$

and

$$\mathcal{E}(k) = -\delta + Ak^2 .$$

The constants A, B, and C are determined by cyclotron experiments; the spin-orbit splitting is δ. With the minus sign in the first relation, the heavy hole constant energy surface is described; a cross sectional view in the (001) plane is almost a square and a cross sectional view in the (110) plane is almost a rectangle. Thus, a cube was chosen as a first approximation to represent this type of surface. With the plus sign in the first relation, the light hole constant energy surfaces are described; cross sectional views in the (001) and (110) planes are

almost diamond-like. Thus, the choice of a set of octahedrons was made. The second relation describes the split-off hole constant energy surfaces as spheres. The assumption of these simple shapes is not foreign to the study of transport phenomena in diamond-like materials (38,39,40).

There are several undesirable features associated with plane faced energy surfaces. For certain orientations of the magnetic field, infinite cyclotron frequencies are encountered. This is due to the fact that the speed of a hole in the plane of a hodograph does not approach zero as the arc length of a hodograph approaches zero. This necessitated averaging the elements of the tensor S over the range of cyclotron frequencies. The density of charge carriers contributing to the magnetoconductivity tensor of each valence band must be correctly computed. For example, with the magnetic field along the [001] axis of the heavy hole valence band, only 2/3 of the charge carriers on each energy surface contribute to the transverse magnetoconductivity (38). In fact, cube energy surfaces exhibit a zero longitudinal magnetoresistance when the magnetic field is along the [001] axis.

For the heavy hole cubic energy surface, the types of hodographs resulting from the orientation of the magnetic field along the [110] , [$\bar{1}$11], and [1$\bar{1}$2] axes are geometrically described in Figures 53 to 55. Note that the [1$\bar{1}$3] axis of DS-2 has been approximated as a [1$\bar{1}$2] axis. With the magnetic field along the [110] axis, the hodograph is a rectangle as shown in Figure 53. The height of the rectangle is a constant R ; the width depends on the parameter t, which measures the distance along the edge of the cube of edge length R. The speed of the heavy hole anywhere on the cube surface is V; its velocity on the

particular surface containing a side of the hodograph is written in the form V[a b c] where a, b, and c are direction cosines. The velocity V[a b c] is drawn perpendicular to the associated side of the hodograph only for convenience. The cyclotron frequency is given; it usually depends on the parameter t and was computed from the following relationship analogous to that satisfied by spherical energy surfaces:

$$\frac{\langle p \rangle}{m_H} = \frac{\hbar \frac{R}{2}}{m_H} = V .$$

The heavy hole has an effective mass m_H and a momentum $\hbar R/2$ along the direction of the velocity. The average contribution to the magnetoconductivity tensor was found by taking the parameter t as ½. With the magnetic field along the $[\bar{1}11]$ axis, both the complete and the truncated equilateral triangular hodographs shown in Figure 54 are found. Equal contributions from each type of hodograph to the magnetoconductivity tensor was assumed; the parameter t was taken to be ½ in each case. Figure 55 illustrates the two types of hodographs encountered with the magnetic field along the $[1\bar{1}2]$ axis. The origin of the coordinate system needed for expanding the velocity in a Fourier series was taken to be the intersection of the $[\bar{1}11]$ axis with the plane of the hodograph. Equal contributions from each type of hodograph to the magnetoconductivity tensor was assumed; the parameter t was taken to be ½ for the upper hodograph in Figure 55 and 3/2 for the lower hodograph.

For the light hole octahedral energy surface, the types of hodographs resulting from the orientation of the magnetic field along the [110] , $[\bar{1}11]$, and $[1\bar{1}2]$ axes are geometrically described in Figures 56 and 57. With the magnetic field along the [110] axis, the hodograph is the six-sided figure shown in part (a) of Figure 56. The

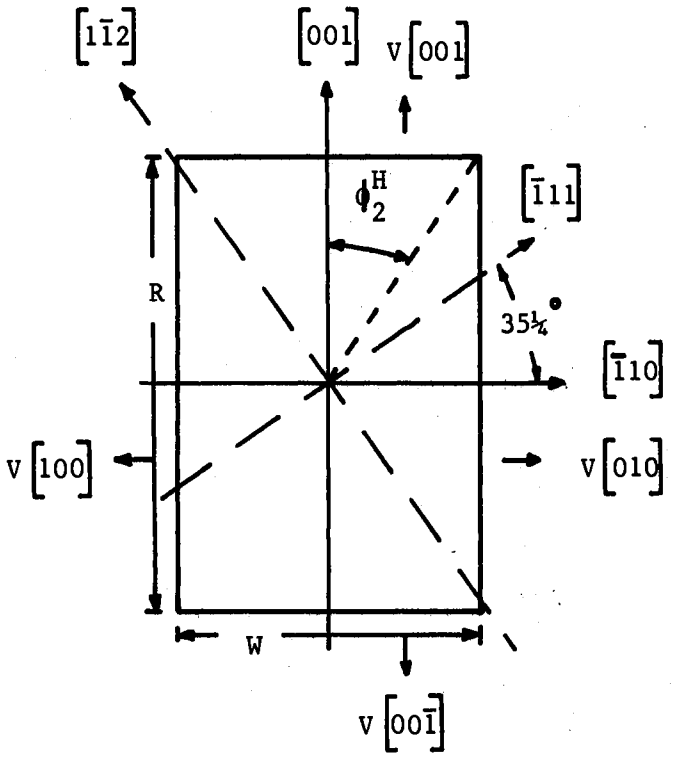

$$W = \sqrt{2}\ tR$$

$$0 \leqslant t \leqslant 1$$

$$\omega = \frac{\pi}{2\sqrt{2}} \cdot \frac{eH}{m_H c} \cdot \frac{1}{1+t}$$

Figure 53. Hodograph in Cubic Energy Surface with H along the [110] Axis

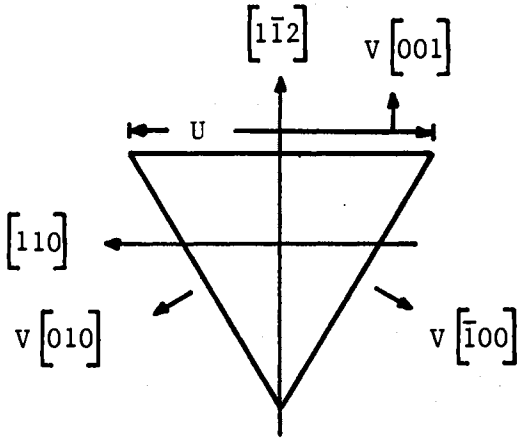

$$U = \sqrt{2}\ tR$$

$$0 \leqslant t \leqslant 1$$

$$\omega = \frac{\pi}{3\sqrt{3}} \cdot \frac{eH}{m_H c} \cdot \frac{1}{t}$$

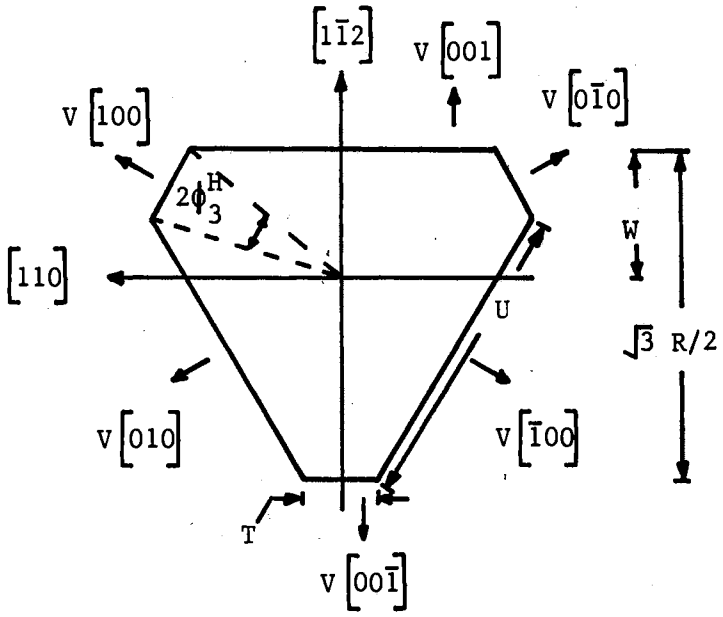

$$T = \sqrt{2}\ tR$$

$$U = \sqrt{2}\ (1-t)R$$

$$W = (1+t)R/\sqrt{6}$$

$$0 \leqslant t \leqslant 1$$

$$\omega = \frac{\pi}{3\sqrt{3}} \cdot \frac{eH}{m_H c}$$

Figure 54. Hodographs in Cubic Energy Surface with H along the [$\bar{1}$11] Axis

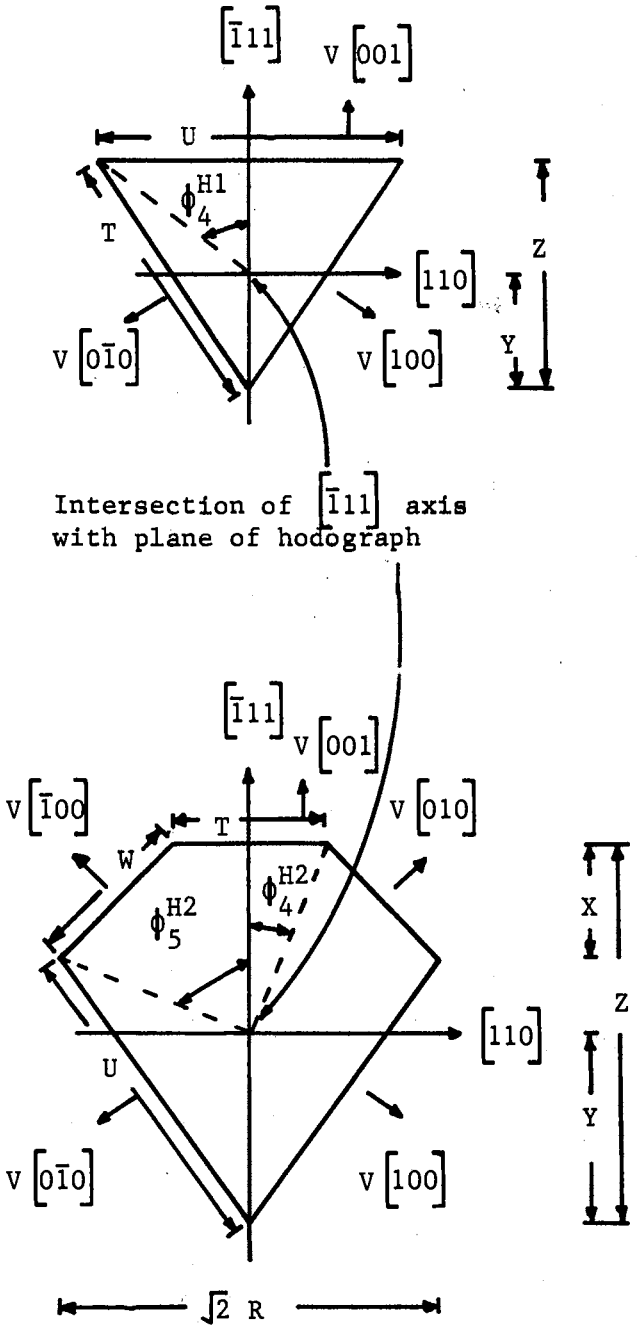

$U = \sqrt{2}\ tR$

$T = \sqrt{5}\ tR/2$

$Z = \sqrt{3}\ tR/2$

$Y = Z/2$

$0 \leqslant t \leqslant 1$

$$\omega = \frac{\pi}{2\sqrt{6}} \cdot \frac{eH}{m_H c} \cdot \frac{1}{t}$$

$T = \sqrt{2}\ (2-t)R$

$W = \sqrt{5}\ (t-1)R/2$

$U = \sqrt{5}\ R/2$

$Z = \sqrt{3}\ tR/2$

$Y = Z/2$

$X = \sqrt{3}\ (t-1)R/2$

$1 \leqslant t \leqslant 2$

$$\omega = \frac{\pi}{2\sqrt{6}} \cdot \frac{eH}{m_H c}$$

Figure 55. Hodographs in Cubic Energy Surface with H along the [1$\bar{1}$2] Axis

parameter t measures the distance along the edge of the octahedron of edge length R. The speed of the light hole anywhere on the octahedral surface is V; its velocity on the particular surface containing a side of the hodograph is written as described for the cubic surfaces. In the computation of the cyclotron frequency, the following relationship analogous to that satisfied by spherical energy surfaces was used:

$$\frac{\langle p \rangle}{m_L} = \frac{\hbar R/\sqrt{6}}{m_L} = V .$$

The light hole has an effective mass m_L and a momentum $\hbar R/\sqrt{6}$ along the direction of the velocity. The average contribution to the magnetoconductivity tensor was found by taking the parameter t as ½. With the magnetic field along the $[\bar{1}11]$ axis, the truncated equilateral triangular hodograph shown in part (b) of Figure 56 was encountered. The cyclotron frequency was independent of the parameter t, and the average contribution to the magnetoconductivity tensor was taken with the parameter t equal to ½. Figure 57 illustrates the two types of hodographs encountered with the magnetic field along the $[1\bar{1}2]$ axis. The origin of the coordinate system needed for expanding the velocity in a Fourier series was taken to be the intersection of the [001] axis with the plane of the hodograph. Equal contributions from each type of hodograph to the magnetoconductivity tensor was assumed; the parameter t was taken to be 1/6 for the upper hodograph in Figure 57 and 2/3 for the lower hodograph.

For the split-off hole spherical energy surfaces, all hodographs are circles. The cyclotron frequency is $eH/m_S c$, where m_S is the effective mass; the frequency is independent of the orientation of the magnetic field and the size of the hodograph.

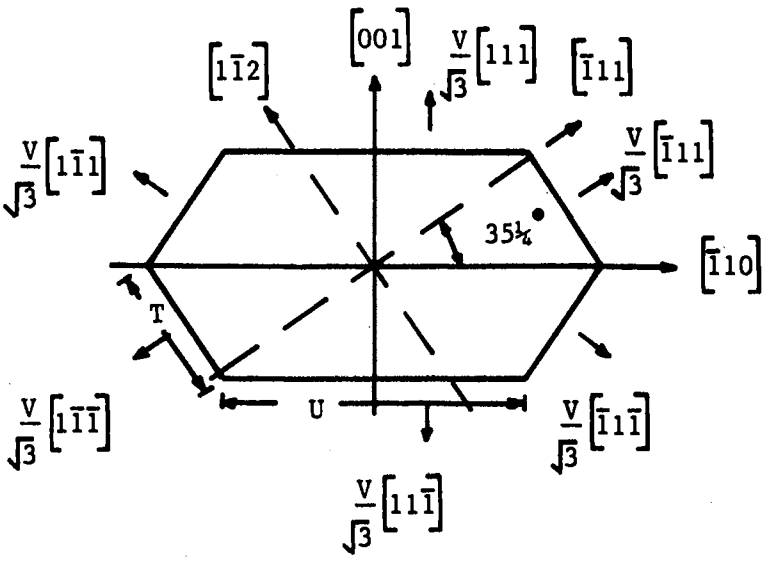

(a) H along the [110] Axis

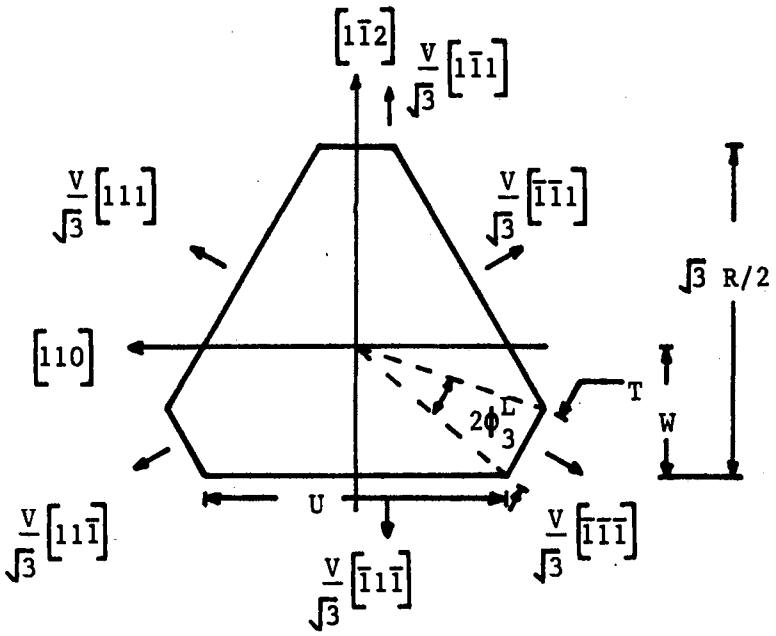

(b) H along the $[\bar{1}11]$ Axis

Figure 56. Hodographs in Octahedral Energy Surface

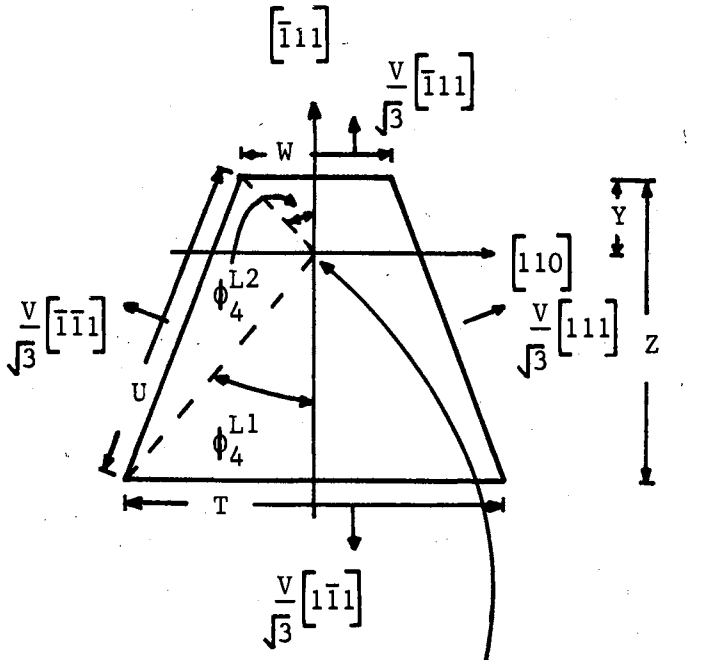

$W = tR$

$U = \sqrt{7}\ tR$

$T = 3tR$

$Z = \sqrt{6}\ tR$

$Y = Z/4$

$0 \leqslant t \leqslant 1/3$

$$\omega = \frac{\pi}{8\sqrt{6}} \cdot \frac{eH}{m_L c} \cdot \frac{1}{t}$$

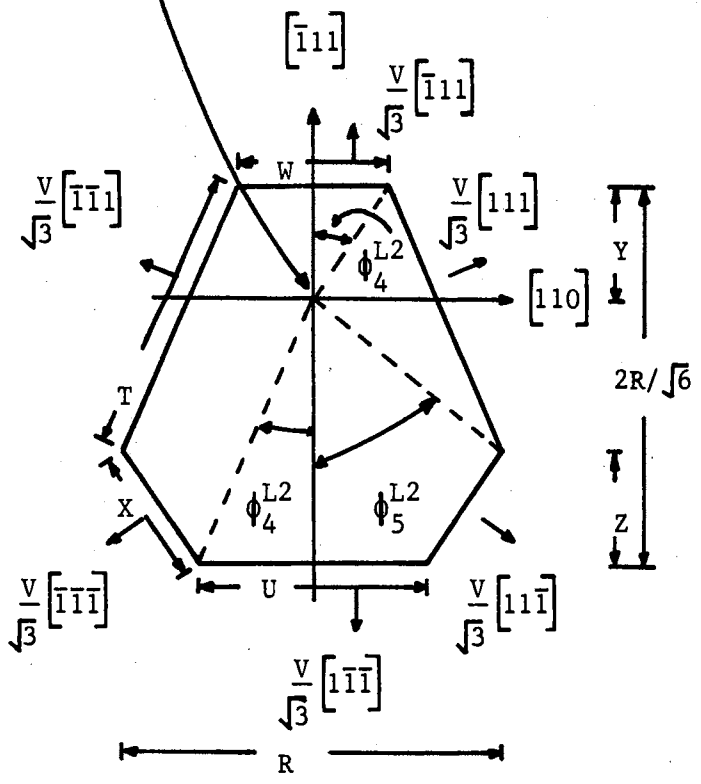

$W = tR$

$T = \sqrt{7}\ (1-t)R/2$

$U = (4-3t)R/3$

$X = \sqrt{7}\ (3t-1\ R/6$

$Y = \sqrt{6}\ tR/4$

$Z = (3t-1)R/\sqrt{6}$

$1/3 \leqslant t \leqslant 1$

$$\omega = \frac{\sqrt{3}\,\pi}{5\sqrt{2}} \cdot \frac{eH}{m_L c}$$

Figure 57. Hodographs in Octahedral Energy Surface with H along the [1$\bar{1}$2] Axis

A detailed account of the theory of scattering mechanisms in the diamond-like material germanium is given in the article written by E. G. S. Paige (41). The interaction between holes and the vibrating diamond lattice is assumed to be of a simple form in which the hole is scattered from one state to another via the emission or absorption of a single longitudinal acoustical phonon. The relaxation time, which can be derived from a deformation potential calculation for an energy band of standard form, is

$$\tau_L = \tau_L^o \, x^{-\frac{1}{2}}$$

The subscript L in this case stands for "lattice"; τ_L^o is a constant to be experimentally determined; and x is the energy of the hole divided by kT (k, when used in the expression kT, is Boltzmann's constant). The interaction of the hole with an ionized impurity in the diamond yields the relaxation time

$$\tau_I = \frac{\tau_I^o \, x^{3/2}}{g(n^*,T,x)} \quad .$$

The subscript I stands for "ionized impurity"; τ_I^o is a constant to be determined; and $g(n^*, T, x)$ is a slowly varying function of energy, temperature, number of ionized impurities, and the degree of compensation within the diamond. When both of these scattering mechanisms occur independently of one another, the net scattering probability $1/\tau$ is the simple sum of the scattering probability due to each scattering mechanism:

$$\frac{1}{\tau} = \frac{1}{\tau_I} + \frac{1}{\tau_L} \quad ,$$

or

$$\tau = \frac{\tau_L^o \, x^{3/2}}{\beta + x^2} \quad . \tag{13}$$

The parameter β describes the degree of impurity scattering compared to lattice scattering (for each type of hole); it is approximated as

$$\beta \approx 6 \frac{\mu_o^L}{\mu_o^I} \quad . \tag{14}$$

The mobility of a charge carrier in the case of negligible scattering by ionized impurities is μ_o^L, and μ_o^I is the mobility of a charge carrier in the limit of negligible scattering by lattice vibrations. This approximation is discussed in the article written by A. C. Beer (42).

Scattering by such mechanisms as neutral impurity atoms, dislocations, transverse acoustical lattice vibrations, and acoustical and longitudinal optical lattice vibrations are neglected. Success in neglecting these types of scattering mechanisms when studying the magnetic field dependence of the transverse magnetoresistance and Hall coefficient of p-type germanium is presented in a paper by A. C. Beer and R. K. Willardson (43).

Having developed the elements of the tensor S (one tensor for each type of hole) from the Fourier analysis of the hodographs (the particular hodographs associated with the selected values of the parameter t), and having chosen a mixed scattering mechanism for each type of hole, the elements of the magnetoconductivity tensor were computed from equation (9). The elements of the magnetoconductivity tensor of the diamond is the simple sum of the corresponding elements of the tensor associated with each valence band. With the magnetic field along the [110] axis,

the elements $\sigma_{11}, \sigma_{22}, \sigma_{33}$, and σ_{12}, necessary in computing the magnetoresistance and Hall coefficient factors, is given in Table IV. The symbol "H" stands for "heavy hole"; the lattice scattering mobility in the limit of vanishing magnetic field is μ_H^{0L} (superscript L for lattice); particle density p_H is associated with a band composed of spherical constant energy surfaces characterized by an effective mass m_H and the mixed scattering parameter is β_H. Quantities with the subscript L are associated with the light hole, and subscripted S quantities are associated with the split-off holes. The transport integrals $k(\beta,\gamma)$ and $L(\beta,\gamma)$ have been numerically evaluated by A. C. Beer, J. A. Armstrong, and I. N. Greenberg (44):

$$K(\beta,\gamma) = \int_0^\infty \frac{e^{-x}\,(x^2+\beta)\,x^3}{(x^2+\beta)^2+\gamma x^3}\,dx \quad , \tag{15}$$

and

$$L(\beta,\gamma) = \frac{2}{\sqrt{\pi}}\int_0^\infty \frac{e^{-x}\,x^{9/2}}{(x^2+\beta)^2+\gamma x^3}\,dx \tag{16}$$

In Table IV, the quantity γ is given an integer subscript which identifies it with a particular term of the infinite series and an alphabetic superscript associating it with a particular energy band. It is proportional to the square of the product of the zero field lattice scattering mobility of the associated type of hole and the magnetic field H. Special symbols relative to the [110] orientation of the magnetic field are defined at the end of the table.

With the magnetic field along the [$\bar{1}$11] axis, the necessary elements of the magnetoconductivity tensor are given in Table V. In this case, an additional numerical superscript (2 is read as two) had

to be placed on γ. The summation index n, the special integers m, and other necessary symbols are also defined in the table.

With the magnetic field along the $[1\bar{1}2]$ axis, the six necessary elements of the magnetoconductivity tensor are given in Table VI. An additional numerical superscript was again placed on γ. The definition of special symbols and the interpretation of the summation indices are also given in the table.

Application to Galvanomagnetic Measurements

The diamond DS-2 was treated as an anisotropic, isothermal solid. In relating the magnetoresistance and Hall coefficient of an anisotropic solid to the elements of the resistivity tensor, the suggestive definitions given by A. C. Beer (45) were used. As a result, the magnetoresistance effect when the magnetic field is directed along the 3-axis (z-axis) and the electric current density is directed along the j-axis (j = 1,2,3) is

$$\frac{\Delta\rho}{\rho_0} = \tfrac{1}{2}\,\frac{\rho_{jj}(\vec{H}) + \rho_{jj}(-\vec{H})}{\rho_{jj}(H=0)} - 1 \,. \tag{17}$$

The element of the resistivity tensor $\rho_{jj}(\vec{H})$ is a function of the size and the direction of the magnetic field. The Hall coefficient factor is defined as the ratio of the Hall coefficient at a magnetic field H to that in the arbitrary field of 140 kilogauss:

$$\frac{R_H}{R_{140}} = \frac{\rho_{ij}(-\vec{H}) - \rho_{ij}(\vec{H})}{\rho_{ij}(-\vec{H} = -140) - \rho_{ij}(\vec{H} = 140)} \cdot \frac{140}{H} \tag{18}$$

The ij th element of the resistivity is $\rho_{ij}(H)$ $(i \neq j,\ i \neq 3,\ j \neq 3)$. When the electric current is directed along the 1-axis (x-axis), the

TABLE IV

MAGNETOCONDUCTIVITY TENSOR ELEMENTS FOR

MAGNETIC FIELD ALONG [110] AXIS

$$\frac{\pi^2}{e\mu_H^{OL} p_H}\sigma_{11} = 8 \sum_{n \text{ odd} \geq 1} n^{-2} K(\beta_H, \gamma_n^H) +$$

$$+ 8 \frac{\mu_L^{OL}}{\mu_H^{OL}} \frac{p_L}{p_H} \sum_{n \text{ odd} \geq 1} n^{-2} K(\beta_L, \gamma_n^L) +$$

$$+ \pi^2 \frac{\mu_S^{OL}}{\mu_H^{OL}} \frac{p_S}{p_H} K(\beta_S, \gamma_1^S)$$

$$\frac{\pi^2}{e\mu_H^{OL} p_H}\sigma_{22} = 4 \sum_{n \text{ odd} \geq 1} n^{-2} \left[1 + 3\sin(n\phi_2^H)\right] K(\beta_H, \gamma_n^H) +$$

$$+ 8 \frac{\mu_L^{OL}}{\mu_H^{OL}} \frac{p_L}{p_H} \sum_{n \text{ odd} \geq 1} n^{-2} K(\beta_L, \gamma_n^L) +$$

$$+ \pi^2 \frac{\mu_S^{OL}}{\mu_H^{OL}} \frac{p_S}{p_H} K(\beta_S, \gamma_1^S)$$

$$\frac{\pi^2}{e\mu_H^{OL} p_H}\sigma_{33} = 12\left\{ \frac{(\pi - 2\phi_2^H)^2}{8} K(\beta_H, 0) + \sum_{n \text{ even} \geq 1} n^{-2} \sin^2(n\phi_2^H) K(\beta_H, \gamma_n^H)\right\}$$

$$+ 8 \frac{\mu_L^{OL}}{\mu_H^{OL}} \frac{p_L}{p_H} \left\{ \frac{\pi^2}{12} K(\beta_L, 0) + \sum_{n \text{ even} \geq 1} n^{-2} K(\beta_L, \gamma_n^L)\right\} +$$

$$+ \pi^2 \frac{\mu_S^{OL}}{\mu_H^{OL}} \frac{p_S}{p_H} K(\beta_S, 0)$$

TABLE IV

(continued)

$$\frac{\pi^2}{e\mu_H^{OL} p_H}\sigma_{12} = \frac{8}{2^{\frac{1}{2}}} \sum_{n\ \text{odd} \geq 1} \left\{ n^{-2}\left[3\sin^2(n\phi_2^H) - 1\right] K(\beta_H, \gamma_n^H) + \right.$$

$$\left. + 1.5\, n^{-2} \sin(2n\phi_2^H) \frac{\pi^{\frac{1}{2}}}{2} (\gamma_n^H)^{\frac{1}{2}} L(\beta_H, \gamma_n^L) \right\} +$$

$$+ \frac{32}{2^{\frac{1}{2}}\pi} \frac{\mu_L^{OL}}{\mu_H^{OL}} \frac{p_L}{p_H} \sum_{n\ \text{odd} \geq 1} n^{-3} \frac{\pi^{\frac{1}{2}}}{2} (\gamma_n^L)^{\frac{1}{2}} L(\beta_L, \gamma_n^L) +$$

$$+ \pi^2 \frac{\mu_S^{OL}}{\mu_H^{OL}} \frac{p_S}{p_H} \frac{\pi^{\frac{1}{2}}}{2} (\gamma_1^S)^{\frac{1}{2}} L(\beta_S, \gamma_1^S)$$

$$(\gamma_n^H)^{\frac{1}{2}} = 0.984\, n\, \mu_H^{OL}\ H \times 10^{-8}$$

$$(\gamma_n^L)^{\frac{1}{2}} = 0.984\, n\, \mu_L^{OL}\ H \times 10^{-8}$$

$$(\gamma_1^S)^{\frac{1}{2}} = 1.329\, \mu_S^{OL}\ H \times 10^{-8}$$

$$\phi_2^H = 35\tfrac{1}{4}^{\circ}$$

n is an integer ≥ 1

n odd means that n is an odd integer

n even means that n is an even integer

TABLE V

MAGNETOCONDUCTIVITY TENSOR ELEMENTS FOR

MAGNETIC FIELD ALONG $[\bar{1}11]$ AXIS

$$\frac{\pi^2}{e\mu_H^{OL} p_H}\sigma_{11} = \frac{27}{8}\sum_{n\geq 1\neq 3m} n^{-2}\,K(\beta_H,\gamma_n^{H1}) +$$

$$+ 1.5\sum_{n\geq 1\neq 3m} n^{-2}\left\{3\cos(n\tfrac{\pi}{3})\cos(n\phi_3^H) + \sin(n\tfrac{\pi}{3})\sin(n\phi_3^H)\right\}^2 K(\beta_H,\gamma_n^{H2})$$

$$+ 3\frac{\mu_L^{OL}}{\mu_H^{OL}}\frac{p_L}{p_H}\sum_{n\geq 1\neq 3m} n^{-2}\left\{3\cos(n\tfrac{\pi}{3})\cos(n\phi_3^L) + \right.$$

$$\left. + \sin(n\tfrac{\pi}{3})\sin(n\phi_3^L)\right\}^2 K(\beta_L,\gamma_n^L) +$$

$$+ \pi^2\frac{\mu_S^{OL}}{\mu_H^{OL}}\frac{p_S}{p_H}K(\beta_S,\gamma_1^S)$$

$$\frac{\pi^2}{e\mu_H^{OL} p_H}\sigma_{22} = \frac{27}{8}\sum_{n\geq 1\neq 3m} n^{-2}\,K(\beta_H,\gamma_n^{H1}) +$$

$$+ 4.5\sum_{n\geq 1\neq 3m} n^{-2}\sin^2\left[n(\tfrac{\pi}{3} + \phi_3^H)\right]K(\beta_H,\gamma_n^{H2}) +$$

$$+ 9\frac{\mu_L^{OL}}{\mu_H^{OL}}\frac{p_L}{p_H}\sum_{n\geq 1\neq 3m} n^{-2}\sin^2\left[n(\tfrac{\pi}{3} + \phi_3^L)\right]K(\beta_L,\gamma_n^L) +$$

$$+ \pi^2\frac{\mu_S^{OL}}{\mu_H^{OL}}\frac{p_S}{p_H}K(\beta_S,\gamma_1^S)$$

TABLE V

(continued)

$$\frac{\pi^2}{e\mu_H^{OL} p_H}\sigma_{33} = \tfrac{1}{2} K(\beta_H,0) + \pi^2 \frac{\mu_S^{OL}}{\mu_H^{OL}} \frac{p_S}{p_H} K(\beta_S,0) +$$

$$+ 36\left\{ \frac{(\pi - 6\phi_3^L)^2}{72} K(\beta_H,0) + \sum_{n \geq 1 \neq 3m} n^{-2} \sin^2(n\phi_3^H) K(\beta_H,\gamma_n^{H2}) + \right.$$

$$+ 24 \frac{\mu_L^{OL}}{\mu_H^{OL}} \frac{p_L}{p_H} \frac{(\pi - 6\phi_3^L)^2}{72} K(\beta_L,0) + \sum_{n \geq 1 \neq 3m} n^{-2} \sin^2(n\phi_3^L) K(\beta_L,\gamma_n^L)$$

$$\frac{\pi^2}{e\mu_H^{OL} p_H}\sigma_{12} = \frac{27}{8} \sum_{n \geq 1 \neq 3m} (-1)^{N-1} n^{-2} \frac{\pi^{\frac{1}{2}}}{2} (\gamma_n^{H1})^{\frac{1}{2}} L(\beta_H,\gamma_n^{H1}) +$$

$$+ \frac{3(3)^{\frac{1}{2}}}{2} \sum_{n \geq 1 \neq 3m} n^{-2} \sin\left[n\left(\frac{\pi}{3} + \phi_3^H\right)\right]\left\{ 3 \cos\left(n\frac{\pi}{3}\right) \cos(n\phi_3^H) + \right.$$

$$\left. + \sin\left(n\frac{\pi}{3}\right) \sin(n\phi_3^H) \right\} \frac{\pi^{\frac{1}{2}}}{2} (\gamma_n^{H2})^{\frac{1}{2}} L(\beta_H,\gamma_n^{H2}) +$$

$$+ 3(3)^{\frac{1}{2}} \frac{\mu_L^{OL}}{\mu_H^{OL}} \frac{p_L}{p_H} \sum_{n \geq 1 \neq 3m} n^{-2} \sin\left[n\left(\frac{\pi}{3} + \phi_3^L\right)\right]\left\{ 3\cos\left(n\frac{\pi}{3}\right) \cos(n\phi_3^L) + \right.$$

$$\left. + \sin\left(n\frac{\pi}{3}\right) \sin(n\phi_3^L) \right\} \frac{\pi^{\frac{1}{2}}}{2} (\gamma_n^L)^{\frac{1}{2}} L(\beta_L,\gamma_n^L) +$$

$$+ \pi^2 \frac{\gamma_S^{OL}}{\gamma_H^{OL}} \frac{p_S}{p_H} \frac{\pi^{\frac{1}{2}}}{2} (\gamma_1^S)^{\frac{1}{2}} L(\beta_S,\gamma_1^S)$$

TABLE V

(continued)

$(\gamma_n^{H1})^{\frac{1}{2}} = 1.607\ n\ \mu_H^{OL}\ H\ X10^{-8}$

$(\gamma_n^{H2})^{\frac{1}{2}} = 0.804\ n\ \mu_H^{OL}\ H\ X10^{-8}$

$(\gamma_n^{L})^{\frac{1}{2}} = 1.072\ n\ \mu_L^{OL}\ H\ X10^{-8}$

$(\gamma_1^{S})^{\frac{1}{2}} = 1.329\ \mu_S^{OL}\ H\ X10^{-8}$

$\phi_3^H = 14^o$

$\phi_3^L = 14^o$

n is an integer

$n \geqslant 1 \neq 3m$ means n is an integer $\geqslant 1$ but not a multiple of 3

$n \geqslant 1 = 3m$ means n is an integer $\geqslant 1$ and only a multiple of 3

N is the number of the term in the infinite series

TABLE VI

MAGNETOCONDUCTIVITY TENSOR ELEMENTS FOR

MAGNETIC FIELD ALONG $[1\bar{1}2]$ AXIS

$$\frac{\pi^2}{e\mu_H^{0L} p_H}\sigma_{11} = 1.5 \sum_{n\geq 1} n^{-2}\left\{1 - (-1)^n \cos(n\phi_4^{H1})\right\}^2 K(\beta_H,\gamma_n^{H1}) +$$

$$+ 1.5 \sum_{n\geq 1} n^{-2}\left\{1 - (-1)^n \cos(n\phi_4^{H2})\right\}^2 K(\beta_H,\gamma_n^{H2}) +$$

$$+ 8\frac{\mu_L^{0L}}{\mu_H^{0L}}\frac{p_L}{p_H} \sum_{n\ \text{odd}\geq 1} n^{-2}\cos^2(n\phi_4^{L1})\, K(\beta_L,\gamma_n^{L1}) +$$

$$+ 8\frac{\mu_L^{0L}}{\mu_H^{0L}}\frac{p_L}{p_H} \sum_{n\ \text{odd}\geq 1} n^{-2}\cos^2(n\phi_4^{L2})\, K(\beta_L,\gamma_n^{L2}) +$$

$$+ \pi^2\frac{\mu_S^{0L}}{\mu_H^{0L}}\frac{p_S}{p_H} K(\beta_S,\gamma_1^S)$$

$$\frac{\pi^2}{e\mu_H^{0L} p_H}\sigma_{22} = 4\left\{\frac{(2\phi_4^{H1}-\pi)^2}{8} K(\beta_H,0) + \sum_{n\geq 1} n^{-2}\sin^2(n\phi_4^{H1})\, K(\beta_H,\gamma_n^{H1})\right. +$$

$$\left. + 4\left\{\frac{(2\phi_5^{H1}-\pi)^2}{8} K(\beta_H,0) + \sum_{n\geq 1} n^{-2}\sin^2(n\phi_5^{H2})\, K(\beta_H,\gamma_n^{H2})\right\} +\right.$$

$$+ \frac{16}{3}\frac{\mu_L^{0L}}{\mu_H^{0L}}\frac{p_L}{p_H}\frac{\pi^2}{32} K(\beta_L,0) + \sum_{n\ \text{odd}\geq 1} n^{-2}\sin^2(n\phi_4^{L1})\, K(\beta_L,\gamma_n^{L1}) +$$

$$+ \frac{4}{3}\frac{\mu_L^{0L}}{\mu_H^{0L}}\frac{p_L}{p_H}\frac{(\pi-2\phi_5^{L2})^2}{8} K(\beta_L,0) + \sum_{n\geq 1} n^{-2}\left\{\left[(-1)^n - 1\right]\sin(n\phi_4^{L2}) +\right.$$

$$\left. - \sin(n\phi_5^{L2})\right\}^2 K(\beta_L,\gamma_n^{L2}) + \pi^2\frac{\mu_S^{0L}}{\mu_H^{0L}}\frac{p_S}{p_H} K(\beta_S,\gamma_1^S)$$

TABLE VI

(continued)

$$\frac{\pi^2}{e\mu_H^{OL} p_H}\sigma_{33} = \tfrac{1}{2}\left\{\frac{(\pi+\phi_4^{H1})^2}{2} K(\beta_H,0) + \sum_{n\geq 1} n^{-2}\sin^2(n\phi_4^{H1})\, K(\beta_H,\gamma_n^{H1})\right\} +$$

$$+ \tfrac{1}{2}\left\{\frac{(\pi-2\phi_5^{H2}+3\phi_4^{H2})^2}{2} K(\beta_H,0) + \sum_{n\geq 1} n^{-2}\left[2\sin(n\phi_5^{H2}) - 3\sin(n\phi_4^{H2})\right]^2 X\right.$$

$$\left. K(\beta_H,\gamma_n^{H2})\right\} +$$

$$+ \frac{8}{3}\frac{\mu_L^{OL}}{\mu_H^{OL}}\frac{p_L}{p_H}\left\{\frac{\pi^2}{8} K(\beta_L,0) + \sum_{n \text{ odd}\geq 1} n^{-2}\sin^2(n\phi_4^{L1})\, K(\beta_L,\gamma_n^{L1})\right\} +$$

$$+ \frac{2}{3}\frac{\mu_L^{OL}}{\mu_H^{OL}}\frac{p_L}{p_H}\left\{\frac{(\pi-2\phi_5^{L2})^2}{2} K(\beta_L,0) + \sum_{n\geq 1} n^{-2}\left[\left((-1)^n - 1\right)\sin(n\phi_4^{L2}) +\right.\right.$$

$$\left.\left. + 2\sin(n\phi_5^{L2})\right]^2 K(\beta_L,\gamma_n^{L2})\right\} + \pi^2\frac{\mu_S^{OL}}{\mu_H^{OL}}\frac{p_S}{p_H} K(\beta_S,0)$$

$$\frac{\pi^2}{e\mu_H^{OL} p_H}\sigma_{12} = 6^{\frac{1}{2}}\sum_{n\geq 1}(-1)^{n-1} n^{-2}\sin(n\phi_4^{H1})\left\{1 - (-1)^n\cos(n\phi_4^{H1})\right\} X$$

$$\frac{\pi^{\frac{1}{2}}}{2}(\gamma_n^{H1})^{\frac{1}{2}} L(\beta_H,\gamma_n^{H1}) +$$

$$+ 6^{\frac{1}{2}}\sum_{n\geq 1} n^{-2}(-1)^{n-1}\sin(n\phi_5^{H2})\left\{1 - (-1)^n\cos(n\phi_4^{H2})\right\} X$$

$$\frac{\pi^{\frac{1}{2}}}{2}(\gamma_n^{H2})^{\frac{1}{2}} L(\beta_H,\gamma_n^{H2}) +$$

$$+ \frac{4(2)^{\frac{1}{2}}}{3^{\frac{1}{2}}}\frac{\mu_L^{OL}}{\mu_H^{OL}}\frac{p_L}{p_H}\sum_{n \text{ odd}\geq 1} n^{-2}\sin(2n\phi_4^{L1})\frac{\pi^{\frac{1}{2}}}{2}(\gamma_n^{L1})^{\frac{1}{2}} L(\beta_L,\gamma_n^{L1}) +$$

$$+ \frac{8}{6^{\frac{1}{2}}}\frac{\mu_L^{OL}}{\mu_H^{OL}}\frac{p_L}{p_H}\sum_{n \text{ odd}\geq 1} n^{-2}\cos(n\phi_4^{L2})\left\{\left[1 - (-1)^n\sin(n\phi_4^{L2}) +\right.\right.$$

TABLE VI

(continued)

$$+ \sin(n\phi_5^{L2})\Big\} \frac{\pi^{\frac{1}{2}}}{2} (\gamma_n^{L2})^{\frac{1}{2}} L(\beta_L, \gamma_n^{L2}) + \pi^2 \frac{\mu_S^{OL}}{\mu_H^{OL}} \frac{p_S}{p_H} \frac{\pi^{\frac{1}{2}}}{2} (\gamma_1^S)^{\frac{1}{2}} L(\beta_S, \gamma_1^S)$$

$$\frac{\pi^2}{e\mu_H^{OL} p_H} \sigma_{13} = \frac{3^{\frac{1}{2}}}{2} \sum_{n \geq 1} n^{-2} (-1)^{n-1} \sin(n\phi_4^{H1}) \Big\{1 - (-1)^n \cos(n\phi_4^{H1})\Big\} X$$

$$\frac{\pi^{\frac{1}{2}}}{2} (\gamma_n^{H1})^{\frac{1}{2}} L(\beta_H, \gamma_n^{H1}) +$$

$$+ \frac{3^{\frac{1}{2}}}{2} \sum_{n \geq 1} n^{-2} (-1)^n \Big[1 - (-1)^n \cos(n\phi_4^{H2})\Big] \Big[2\sin(n\phi_5^{H2}) - 3 \sin(n\phi_4^{H2})\Big] X$$

$$\frac{\pi^{\frac{1}{2}}}{2} (\gamma_n^{H2})^{\frac{1}{2}} L(\beta_H, \gamma_n^{H2}) +$$

$$- \frac{4}{3^{\frac{1}{2}}} \frac{\mu_L^{OL}}{\mu_H^{OL}} \frac{p_L}{p_H} \sum_{n \text{ odd} \geq 1} n^{-2} \sin(2n\phi_4^{L1}) \frac{\pi^{\frac{1}{2}}}{2} (\gamma_n^{L1})^{\frac{1}{2}} L(\beta_L, \gamma_n^{L1}) +$$

$$+ \frac{4}{3^{\frac{1}{2}}} \frac{\mu_L^{OL}}{\mu_H^{OL}} \frac{p_L}{p_H} \sum_{n \text{ odd} \geq 1} n^{-2} \cos(n\phi_4^{L2}) \Big\{\Big[(-1)^n - 1\Big] \sin(n\phi_4^{L2}) +$$

$$+ 2\sin(n\phi_5^{L2})\Big\} \frac{\pi^{\frac{1}{2}}}{2} (\gamma_n^{L2})^{\frac{1}{2}} L(\beta_L, \gamma_n^{L2})$$

$$\frac{\pi^2}{e\mu_H^{OL} p_H} \sigma_{23} = 2^{\frac{1}{2}} \Big\{ (\pi + \phi_4^{H1}) (2\phi^{H1} - \pi) K(\beta_H, 0) + \sum_{n \geq 1} n^{-2} \sin^2(n\phi_4^{H1}) X$$

$$K(\beta_H, \gamma_n^{H1})\Big\} +$$

$$- 2^{\frac{1}{2}} \Big\{ \frac{(2\phi_5^{H2} - \pi)(\pi - 2\phi_5^{H2} + 3\phi_4^{H2})}{4} K(\beta_H, 0) + \sum_{n \geq 1} n^{-2} \sin(n\phi_5^{H2}) X$$

$$\Big[2\sin(n\phi_5^{H2}) - 3\sin(n\phi_4^{H2})\Big] K(\beta_H, \gamma_n^{H2}) +$$

TABLE VI

(continued)

$$-\frac{8(2)^{\frac{1}{2}}}{3}\frac{\mu_L^{0L}}{\mu_H^{0L}}\frac{p_L}{p_H}\left\{\frac{\pi^2}{16}K(\beta_L,0)+\sum_{n\ \text{odd}\geq 1} n^{-2}\sin^2(n\phi_4^{L1})\,K(\beta_L,\gamma_n^{L1})\right\}+$$

$$-\frac{2(2)^{\frac{1}{2}}}{3}\frac{\mu_L^{0L}}{\mu_H^{0L}}\frac{p_L}{p_H}\left\{\frac{(\pi-2\phi_5^{L2})^2}{4}K(\beta_L,0)+\sum_{n\geq 1}\left[\left((-1)^n-1\right)\sin(n\phi_4^{L2})+\right.\right.$$

$$\left.\left.-\sin(n\phi_5^{L2})\right]\left[\left((-1)^n-1\right)\sin(n\phi_4^{L2})+2\sin(n\phi_5^{L2})\right]n^{-2}K(\beta_L,\gamma_n^{L2})\right\}$$

$$(\gamma_n^{H1})^{\frac{1}{2}} = 1.705\ n\ \mu_H^{0L}\ H\ X10^{-8}$$

$$(\gamma_n^{H2})^{\frac{1}{2}} = 0.852\ n\ \mu_H^{0L}\ H\ X10^{-8}$$

$$(\gamma_n^{L1})^{\frac{1}{2}} = 1.279\ n\ \mu_L^{0L}\ H\ X10^{-8}$$

$$(\gamma_n^{L2})^{\frac{1}{2}} = 2.046\ n\ \mu_L^{0L}\ H\ X10^{-8}$$

$$(\gamma_1^{S})^{\frac{1}{2}} = 1.329\ \mu_S^{0L}\ H\ X10^{-8}$$

$\phi_4^{H1} = 58\frac{1}{2}^{o}$

$\phi_4^{H2} = 28\frac{1}{2}^{o}$

$\phi_5^{H2} = 73^{o}$

$\phi_4^{L1} = 39\frac{1}{4}^{o}$

$\phi_4^{L2} = 39\frac{1}{4}^{o}$

$\phi_5^{L2} = 58\frac{1}{2}^{o}$

n is an integer ≥ 1

n odd ≥ 1 means that n is an odd integer ≥ 1

subscript ij is taken to be 21 (read as two one); when the electric current is directed along the 2-axis (y-axis), the subscript ij is 12 (read as one two). The magnetic field, measured in kilogauss, is directed in both cases along the 3-axis (z-axis).

The final step in expressing the galvanomagnetic effects in terms of the elements of the magnetoconductivity tensor is the relationships, defined below, between the elements of the resistivity and conductivity tensors:

$$\rho_{ii} = \frac{\sigma_{jj}\sigma_{kk} - \sigma_{jk}\sigma_{kj}}{\det(\sigma)} \qquad \begin{matrix} i \neq j \neq k \neq i \\ i,j,k = 1,2,3 \end{matrix} , \tag{19}$$

and

$$\rho_{ij} = \frac{\sigma_{ik}\sigma_{kj} - \sigma_{ij}\sigma_{kk}}{\det(\sigma)} \qquad \begin{matrix} i \neq j \neq k \neq i \\ i,j,k = 1,2,3 \end{matrix} . \tag{20}$$

The symbol "det(σ)" stands for the determinant of σ.

For a given orientation of the magnetic field, the elements of the magnetoconductivity tensor were taken from the appropriate table (Table IV, V, or VI). All infinite series were approximated by taking only the first two nonzero terms of the series. The Romberg method was used to numerically evaluate the integrals $K(\beta,\gamma)$ and $L(\beta,\gamma)$.

Selection of Parameters

The parameters necessary to evaluate the galvanomagnetic effects are the effective mass, lattice scattering mobility in zero magnetic field in the limit of negligible impurity scattering, and the mixed scattering parameter β for each type of hole. The average effective masses and spin-orbit splitting as measured by C. J. Rauch (36) in cyclotron

resonance experiments at $4^{o}K$ were used. Since the density of holes in a valence band composed of spherical constant energy surfaces varies directly as the three halves power of the effective mass, the ratio of the density of light to heavy holes is

$$\frac{p_L}{p_H} = \left(\frac{m_L}{m_H}\right)^{3/2} = 0.19 \tag{21}$$

Taking into account the 0.006 electron volt separation between the top of the heavy and light hole valence bands and the top of the split-off valence band, the ratio of the density of split-off to heavy holes at the temperatures of $308^{o}K$ and $436^{o}K$ are

$$\frac{p_S}{p_H} = \left(\frac{m_S}{m_H}\right)^{3/2} \exp-[0.006/kT] = \begin{cases} 0.28 \text{ at } 308^{o}K \\ 0.30 \text{ at } 436^{o}K \end{cases} \tag{22}$$

According to the elementary theory of the lattice scattering mobility in the absence of a magnetic field, the mobility varies inversely as the effective mass to the five halves power (called the elementary theory behavior). However, A. C. Beer and R. K. Willardson (43) have explained the magnetic field dependence of the transverse magnetoresistance and Hall coefficient effects in germanium with the lattice scattering mobility varying inversely as the first power of the effective mass (called the germanium-like behavior). An explanation of the two types of behavior is given in the article written by H. Brooks (46). Since there is no experimental evidence favoring one or the other type of effective mass dependence (if either) in diamond, calculations were performed for both types of behavior. With respect to the elementary theory, the ratio of the lattice scattering mobilities of the light and heavy holes is

$$\frac{\mu_L^{OL}}{\mu_H^{OL}} = \left(\frac{m_H}{m_L}\right)^{5/2} = 15.6, \tag{23}$$

and the ratio of the lattice scattering mobilities of the split-off and heavy holes is

$$\frac{\mu_S^{OL}}{\mu_H^{OL}} = \left(\frac{m_H}{m_S}\right)^{5/2} = 5.66. \tag{24}$$

With respect to the germanium-like behavior, the ratio of mobilities are

$$\frac{\mu_L^{OL}}{\mu_H^{OL}} = \frac{m_H}{m_L} = 3, \tag{25}$$

and

$$\frac{\mu_S^{OL}}{\mu_H^{OL}} = \frac{m_H}{m_S} = 2. \tag{26}$$

The elementary theory suggests that the ionized impurity lattice scattering mobility in the absence of the magnetic field varies inversely as the square root of the effective mass. Inspection of the approximate expression for β given in equation (14) reveals that its effective mass dependence depends on the effective mass dependence of the lattice scattering mobility. Therefore, when the elementary theory of lattice scattering was used, the ratio of the mixed scattering parameters of the light and heavy holes was taken as

$$\frac{\beta_L}{\beta_H} = \left(\frac{m_H}{m_L}\right)^2 = 9 \approx 10, \tag{27}$$

and the ratio of the mixed scattering parameters of the split-off and heavy holes was taken as

$$\frac{\beta_S}{\beta_H} = \left(\frac{m_H}{m_S}\right)^2 = 4 \approx 3. \tag{28}$$

On the other hand, the use of the germanium-like lattice scattering behavior makes the two ratios

$$\frac{\beta_L}{\beta_H} = \left(\frac{m_H}{m_L}\right)^{\frac{1}{2}} = \sqrt{3} \approx 1, \tag{29}$$

and

$$\frac{\beta_S}{\beta_H} = \left(\frac{m_H}{m_S}\right)^{\frac{1}{2}} = \sqrt{2} \approx 1. \tag{30}$$

The values on the right hand side of equations (27) to (30) were used. For the germanium-like case, several values (10^{-4} and 10^{-2} at 436°K; 10^{-2} and 1 at 308°K) of β_H were investigated. For the elementary theory, only one value of β_H at each temperature was used (10^{-3} at 436°K and 10^{-1} at 308°K).

From the assumption that the conductivity of the diamond is the sum of the conductivities of each of the three valence bands, it follows that

$$\mu^0(p_H + p_L + p_S) = p_H\mu_H^0 + p_L\mu_L^0 + p_S\mu_S^0. \tag{31}$$

The effective conductivity mobility in zero magnetic field (superscript 0) of all charge carriers in diamond is μ^0; the total density of carriers is $p_H + p_L + p_S$; and μ_H^0, μ_L^0, and μ_S^0 are respectively the conductivity mobilities of the heavy, light, and split-off holes. A. C. Beer (47) has shown that the relationship between the conductivity mobility and lattice scattering mobility of the heavy holes for the case of composite scattering by lattice acoustic phonons and ionized impurities can be reduced to

$$\mu_H^0 = \mu_H^{0L} \; K(\beta_H, 0), \tag{32}$$

where the integral $K(\beta_H,0)$ is defined by equation (15) with $\gamma_H = 0$. Similar relationships hold for the light and split-off holes. A. C. Beer (47) has also shown that the conductivity and Hall mobilities of the diamond satisfy the expression

$$\mu_0^{Hall} = \mu^0 r. \tag{33}$$

The quantity r is the ratio of the Hall coefficient in the limit of zero magnetic field to the saturation Hall coefficient in large magnetic fields. The Hall mobility and the quantity r are directly measured from the data. To compute the "best guess" for the heavy hole lattice scattering mobility μ_H^{0L}, the conductivity mobility was determined via equation (33) from the measured (actually estimated) values of the Hall mobility and r. Having chosen β_H, and determining β_L and β_S, allows the conductivity mobility of each type of hole to be a known function of the associated lattice scattering mobility. Finally, equation (31) was used to determine the "best guess" for μ_H^{0L}.

A summary of the numerical values of the pertinent parameters is given in Table VII. The calculation of the field dependence of all magnetoresistances and Hall coefficient factors at both 308°K and 436°K were made for one value of β_H (at each temperature) and the elementary effective mass behavior of μ_H^{0L}. The results are represented by the solid line in Figures 26 to 52. The lattice scattering mobility is written as μ^L and the effective mass is written as m^* in Figures 26 to 52. In explaining the results of this calculation in the succeeding sections, it will, for convenience, be labeled as the "elementary theory". Calculations of the field dependence of all magnetoresistances and Hall coefficient factors at both 308°K and 436°K were made for

two values of β_H (at each temperature) and the germanium-like behavior of μ_H^{OL}. One result is represented by the long-dash-short-dash line in Figures 26 to 52, and the other is represented by the short-dash line. Whenever the change in the value of β_H had little effect on the magnetoresistance, only the long-dash-short-dash line was drawn. The results of these calculations will be labeled as the "germanium-like theory".

Comparison of Experiment and Theory

In comparing the results of the "elementary theory" for the longitudinal magnetoresistances to the data shown in Figures 26, 27, 38, and 39, it is observed that too large of a magnetoresistance at small magnetic fields, too small of a magnetoresistance in large magnetic fields, and a greater tendency towards saturation than the data is predicted. The "germanium-like theory" predicts the same size of magnetoresistance as measured in small magnetic fields (less than 10 kilogauss), too small of a magnetoresistance in large fields, and more of a tendency towards saturation than the data. Comparing the two "theories" with the longitudinal mangetoresistance in the $[\bar{1}11]$ direction shown in Figures 32 and 33 reveals that both "theories" show too large of a magnetoresistance and less of a tendency towards saturation than the data.

In comparing the results of the "elementary theory" for the transverse magnetoresistances to the data shown in Figures 28, 29, 34 and 35, the best overall agreement between the data and theory is observed. The "germanium-like theory" for the same transverse magnetoresistances shows too small of a magnetoresistance overall and more of a tendency

TABLE VII

SUMMARY OF SELECTED PARAMETERS

p_L/p_H	.19	.19	.19	.19	.19	.19
p_S/p_H	.28	.30	.28	.30	.28	.30
μ_L^{OL}/μ_H^{OL}	15.6	15.6	3	3	3	3
μ_S^{OL}/μ_H^{OL}	5.66	5.66	2	2	2	2
μ_L/μ_H	10	10	1	1	1	1
μ_S/μ_H	3	3	1	1	1	1
μ_{Hall}^{*}/μ_0^H	.01	.001	1	.01	.01	.0001
	1300	500	1250	409	1250	409
r	.9	.9	.91	.85	.91	.85
μ^{0} +	1450	550	1370	480	1370	480
μ_H^{OL} #	400	150	1440	330	960	330
T	308°K	436°K	308°K	436°K	308°K	436°K
Symbol						

*μ_0^{Hall} measured in $cm.^2$/volt sec.

+μ^0 measured in $cm.^2$/volt sec.

#μ_H^{OL} measured in $cm.^2$/volt sec. and written as μ^L in Figures 26 to 52.

towards saturation than indicated by the data. The transverse magnetoresistances in Figures 30 and 31 show a closer correspondence to the "germanium-like theory" in size and field dependence, while the "elementary theory" gives too large of a magnetoresistance overall and less of a tendency towards saturation than the data. The transverse magnetoresistance at 308°K in Figure 36 shows a closer correspondence to the "germanium-like theory" in size and field dependence; at 436°K (Figure 37), the "elementary theory" would be preferred. It should be recalled that this particular transverse magnetoresistance showed very little temperature dependence compared to other magnetoresistances. Although this difference in temperature dependence may be characteristic of diamond, one cannot help but be suspicious of the data. A closer correlation is found between the transverse magnetoresistances shown in Figures 40 and 41 with the "elementary theory" in overall size and field dependence than between the data and the "germanium-like theory" (which shows a smaller magnetoresistance and a greater tendency towards saturation). However, a closer correlation between the transverse magnetoresistances shown in Figures 42 and 43 with the "germanium-like theory" is observed with respect to size and magnetic field dependence. The results of the "elementary theory" are too large at all fields.

In comparing both the "elementary theory" and the "germanium-like theory" results for the Hall coefficient factors to the data shown in Figures 45 to 52, it is observed that the latter theory may be more preferable. The trend in the small field dependence of the data suggests that the Hall coefficient factor increases with increasing magnetic field. This trend is predicted in the "germanium-like theory"

results shown in Figures 45, 47, 49, and 50. This type of behavior has been observed in silicon (10). Peaks in the data as observed in Figures 47, 49, and 51 may, like in silicon, be labeled as "fine structure". It has been shown by A. C. Beer (10), and by A. C. Beer and R. K. Willardson (43) that the location and prominence of the fine structure depends both on the lattice scattering mobility and on the mixed scattering parameter. This is observed in comparing the two "germanium-like theory" results with one another in each of Figures 45, 47, 49, and 51. The best correlation between the occurence and location of the peaks in the data and the "germanium-like theory" occurred in Figure 49. It should be noted, however, that most of the Hall coefficient factors as predicted by the "germanium-like theory" in the limit of zero magnetic field are greater than one. The breaks in the experimental data correlated with the production of the pulsed fields did not allow the limiting Hall factors to be determined. The data of R. T. Bate and R. K. Willardson (9) suggests that this limiting Hall factor may be less than one.

Summary and Conclusion

The magnetoresistance for six orthogonal and three parallel orientations of the magnetic field and current, and the Hall coefficient for four orthogonal orientations of the magnetic field and current of the blue end of one semiconducting diamond were measured at the temperatures of 308°K and 436°K in pulsed magnetic fields up to 160 kilogauss. Most measurements were repeated twice using independent pairs of electrical probe contacts. Assuming that conduction in diamond is due to holes associated with three uncoupled

valence bands, and assuming that the constant energy surfaces comprising the heavy hole, light hole, and split-off hole valence bands can, for small energies, be approximated respectively by a set of cubes, octahedrons, and spheres, the magnetoresistances and Hall coefficient factors at both temperatures were computed for the case of mixed scattering by acoustic lattice vibrations and ionized impurities. The diamond is treated as an anisotropic, isothermal solid. For the effective mass dependence of the lattice scattering mobility as predicted by the elementary theory, one value of the mixed scattering parameter was used; two values of the mixed scattering parameter were used for the effective mass dependence of the lattice scattering mobility as experimentally determined for germanium.

Differences in size and magnetic field dependence between the independent measurements of the magnetoresistance were regarded as small at both 308°K and 436°K for the following orientations: (1) magnetic field in the $[110]$ and current in the $[\bar{1}11]$ directions; (2) magnetic field and current in the $[\bar{1}11]$ direction (308°K only); (3) magnetic field in the $[\bar{1}11]$ and current in the $[110]$ directions; (4) magnetic field in the $[\bar{1}11]$ and current in the $[1\bar{1}3]$ directions (436°K only); and (5) magnetic field in the $[1\bar{1}3]$ and current in the $[110]$ directions. Differences in magnetic field dependence, but not size, between the independent measurements of the Hall coefficients were small. Taking a strict average of all independent measurements of a magnetoresistance at 140 kilogauss for a given orientation of the magnetic field revealed that the two transverse magnetoresistances differed in nearly all cases by a factor of two. For each orientation of the magnetic field, the longitudinal magnetoresistance, which is smaller

than the transverse magnetoresistances, is smaller than the largest transverse magnetoresistance by a factor between two and five. An unexplained correlation between the measurements of the Hall coefficient and the pattern of producing the pulsed magnetic fields occurred. This prevented the Hall coefficient factors in the limit of zero magnetic field from being determined. The Hall coefficient at both temperatures appears to increase, for small magnetic fields, with increasing magnetic field. At 308°K, an apparent broad peak in the Hall coefficient factors was observed for the following orientations: (1) magnetic field in the [110] and current in the [1$\bar{1}$3] directions; (2) magnetic field in the [$\bar{1}$11] and current in the [110] directions; and (3) magnetic field in the [1$\bar{1}$3] and current in the [110] directions. At 436°K, saturation in the Hall coefficient at magnetic fields about 100 kilogauss was observed for the following orientations: (1) magnetic field in the [110] and current in the [1$\bar{1}$3] directions; and (2) magnetic field in the [$\bar{1}$11] and current in the [110] directions.

For the constant energy surface model composed of cubes, octahedrons, and spheres, and when the lattice scattering mobility varied inversely as the five halves power of the effective mass (elementary theory), reasonable agreement with the data in size and magnetic field dependence of the transverse magnetoresistance occurred at 308°K and 436°K for the following orientations: (1) magnetic field in the [110] and current in the [$\bar{1}$11] directions; (2) magnetic field in the [$\bar{1}$11] and current in the [110] directions; (3) magnetic field in the [$\bar{1}$11] and current in the [1$\bar{1}$3] directions (436°K only); and (4) magnetic field in the [1$\bar{1}$3] and current in the [110] directions. The size and magnetic field dependence of the calculated Hall coefficient factors

did not correspond to the experimental data. For an increasing magnetic field along the [110] axis and current along either the [$\bar{1}$11] or the [1$\bar{1}$3] axis, the calculated Hall coefficient factor decreased from a zero magnetic field limit greater than 2 to a minimum and then increased. For either an increasing magnetic field along the [$\bar{1}$11] axis or an increasing magnetic field along the [1$\bar{1}$3] axis and the current along the [110] axis, the computed Hall coefficient factors increased from a zero magnetic field limit between 1.1 and 2.2 to a maximum and then decreased.

When the lattice scattering mobility varied inversely as the first power of the effective mass (germanium-like behavior), most predicted magnetoresistances were too small for all values of the magnetic field and showed an earlier tendency towards saturation than the data. Changing the mixed scattering parameter by a factor of 100 along with a change in the "best guess" value of the heavy hole lattice scattering mobility did not significantly change the calculated magnetoresistances. The best agreement with the data in size and magnetic field dependence of the Hall coefficient factor at 308^{o}K and 436^{o}K occurred for the magnetic field in the [$\bar{1}$11] and the current in the [110] directions. The calculated Hall coefficient factors were significantly affected with regard to the position of the peak, the limiting value in zero magnetic field; and the magnetic field dependence for magnetic fields less than 50 kilogauss. Most of the limiting predicted Hall coefficient factors at both temperatures were between 0.9 and 1.1.

BIBLIOGRAPHY

1. Sir Wm. Thomson, "On the Effects of Magnetization of the Electrical Conductivity of Metals," Phil. Trans. 146, 736 (1856).

2. E. H. Hall, "On a New Action of the Magnet on Electric Currents," Amer. J. Math. 2, 287 (1879).

3. M. Glicksman, "The Magnetoresistivity of Germanium and Silicon," Progress in Semiconductors, Ed. A. F. Gibson. (John Wiley and Sons Inc., New York, 1958). Vol. 3, p. 3.

4. F. J. Blatt, Physics of Electronic Conduction in Solids, (McGraw-Hill Book Co., New York, 1968), Chap. 8, p. 287.

5. J. J. Brophy, "Preliminary Study of the Electrical Properties of a Semiconducting Diamond," Phys. Rev. 99, 1336 (1955).

6. I. G. Austin and R. Wolfe, "Electrical and Optical Properties of a Semiconducting Diamond," Proc. Phys. Soc. (London) B69, 329 (1956).

7. P. T. Wedepohl, "Electrical and Optical Properties of Type IIb Diamonds," Proc. Phys. Soc. (London) B70, 177 (1957).

8. E. W. J. Mitchell and P. T. Wedepohl, "Magnetoresistance of a P-Type Semiconducting Diamond," Proc. Phys. Soc. (London) B70, 527 (1957).

9. R. T. Bate and R. K. Willardson, "Hall Coefficient and Magneto-resistance in Semiconducting Diamond," Proc. Phys. Soc. 74, 363 (1959).

10. A. C. Beer, "Fine Structure in the Hall Coefficient," J. Phys. Chem. Solids 8, 507 (1959).

11. P. J. Kemmey and E. W. J. Mitchell, "The Magneto-Resistance of P-Type Semiconducting Diamond," Proc. Roy. Soc. (London) 263, 420 (1961).

12. W. J. Leivo, M. D. Bell, C. C. Johnson, J. B. Krumme, K. J. Russell, H. J. Stein, J. H. Wayland, and T. Young, "Investigations of Semiconducting Properties of Type IIb Diamonds," (Final Report, Air Force Office of Scientific Research, May, 1962), AFOSR-2642, Chap. 5.

13. R. L. Schelhorn and H. G. Nordlin, "Hall and Resistivity Measurements on Semiconducting Diamonds," (Air Force Cambridge Research Laboratories, July, 1963), AFCRL-63-309.

14. K. J. Russell and W. J. Leivo, "High Field Magnetoresistance of a Semiconducting Diamond," Bull. Amer. Phys. Soc. 10, 1092 (1965).

15. K. J. Russell, "High Field Magnetoresistance of Semiconducting Diamond," (Unpub. Ph.D. Dissertation, Oklahoma State University, 1965).

16. F. J. Blatt, Physics of Electronic Conduction in Solids, (McGraw-Hill Book Co., New York, 1968), Chaps. 7 and 8.

17. E. N. Adams and R. W. Keyes, "Galvanomagnetic Phenomena in Very Strong Magnetic Fields," Progress in Semiconductors, Ed. A. F. Gibson. (John Wiley and Sons Inc., New York, 1962), Vol. 6, p. 96.

18. R. K. Willardson, T. C. Harman, and A. C. Beer, "Transverse Hall and Magnetoresistance Effects in P-Type Germanium," Phys. Rev. 96, 1512 (1954).

19. E. H. Putley, The Hall Effect and Semi-Conductor Physics, (Dover Publications, Inc., New York, 1968), Chap. 2, p. 26.

20. R. Berman, E. L. Foster, and J. M. Ziman, "The Thermal Conductivity of Dielectric Crystals: The Effect of Isotopes," Proc. Roy. Soc. (London) 237, 344 (1956).

21. H. J. Goldsmid, C. C. Jenns, and D. A. Wright, "The Thermoelectric Power of a Semiconducting Diamond," Proc. Phys. Soc. 73, 393 (1958).

22. H. Weiss, Structure and Application of Galvanomagnetic Devices, (Pergamon Press, Oxford, 1969), Chap. 1, p. 16.

23. R. F. Wicks, "Solution of the Field Problem of the Germanium Gyrator," J. Appl. Phys. 25, 741 (1954).

24. H. J. Lippmann and F. Kuhrt, "Der Geometrieeinfluss auf den transversalen magnetischen Widerstandseffekt bei rechteckformigen Halblieterplatten," Z. Naturforsch. 13a, 462 (1958).

25. H. J. Lippmann and F. Kuhrt, "Der Geometrieeinfluss auf den Hall-Effekt bei rechteckigen Halblieterplatten," Z. Naturforsch. 13a, 474 (1958).

26. C. Herring, "Effect of Random Inhomogeneities on Electrical and Galvanomagnetic Measurements," J. Appl. Phys. 31, 1939 (1960).

27. R. T. Bate and A. C. Beer, "Influence of Conductivity Gradients on Galvanomagnetic Effects in Semiconductors," J. Appl. Phys. 32, 800 (1961).

28. H. Weiss, "Magnetoresistance," Semiconductors and Semimetals, Ed. R. F. Willardson and A. C. Beer. (Academic Press, New York, 1966), Vol. 1, Chap. 10, p. 315.

29. R. T. Bate, J. C. Bell, and A. C. Beer, "Influence of Magnetoconductivity Discontinuities on Galvanomagnetic Effects in Indium Antimonide," J. Appl. Phys. 32, 806 (1961).

30. K. J. Russell and W. J. Leivo, "Pulsed Magnet System for Production of High Magnetic Fields," Proc. Okla. Acad. Sci. 46, 122 (1966).

31. D. B. Montgomery, Solenoid Magnet Design, The Magnetic and Mechanical Aspects of Resistive and Superconducting Systems, (Wiley Interscience, a Division of John Wiley and Sons, New York, 1969), Chap. VII.

32. S. Foner and W. G. Fisher, "Solid Helix Magnets for Large Volume Pulsed High Fields," Rev. Sci. Instr. 38, 440 (1967).

33. M. D. Bell and W. J. Leivo, "Electrical Contacts to Semiconducting Diamond," Proc. Okla. Acad. Sci. 48, 117 (1969).

34. M. Dresden, "Recent Developments in the Quantum Theory of Transport and Galvanomagnetic Phenomena," Revs. Modern Phys. 33, 265 (1961).

35. J. W. McClure, "Field Dependence of the Magnetoconductivity," Phys. Rev. 101, 1642 (1956).

36. C. J. Rauch, "Millimeter Cyclotron Resonance in Diamond," Proceedings of the International Conference on the Physics of Semiconductors, Ed. A. C. Strickland. (The Institute of Physics and the Physical Society, London, 1962) p. 276.

37. G. Dresselhaus, A. F. Kip, and C. Kittel, "Cyclotron Resonance of Electrons and Holes in Silicon and Germanium Crystals," Phys. Rev. 98, 368 (1955).

38. C. Goldberg, E. N. Adams, and R. E. Davis, "Magnetoconductivity in P-Type Germanium," Phys. Rev. 105, 865 (1957).

39. H. Miyazawa, K. Suzuki, and H. Maeda, "Evidence for the [110] Swelling Constant Energy Surface for Heavy Holes in Silicon," Phys. Rev. 131, 2442 (1963).

40. H. Miyazawa, "Anisotropy of the Hall Effect in P-Type Germanium," Proceedings of the International Conference on the Physics of Semiconductors, Ed. A. C. Strickland. (The Institute of Physics and the Physical Society, London, 1962) p. 636.

41. E. G. S. Paige, "The Electrical Conductivity of Germanium," Progress in Semiconductors, Ed. A. F. Gibson and R. E. Burgess (John Wiley and Sons Inc., New York, 1964) Vol. 8, p. 55.

42. A. C. Beer, "Galvanomagnetic Effects in Semiconductors," Solid State Physics Supplement 4, Ed. F. Seitz and D. Turnbull. (Academic Press, New York, 1963) p. 130.

43. A. C. Beer and R. K. Willardson, "Hall and Transverse Magnetoresistance Effects for Warped Bands and Mixed Scattering," Phys. Rev. 110, 1286 (1958).

44. A. C. Beer, J. A. Armstrong, and I. N. Greenberg, "Evaluation of Transport Integrals for Mixed Scattering and Application to Galvanomagnetic Effect," Phys. Rev. 107, 1506 (1957).

45. A. C. Beer, "Galvanomagnetic Effects in Semiconductors," Solid State Physics Supplement 4, Ed. F. Seitz and D. Turnbull. (Academic Press, New York, 1963) p. 76.

46. H. Brooks, "Electrical Properties of Germanium and Silicon," Advances in Electronics and Electron Physics, Ed. L. Marton. (Academic Press, New York, 1955). Vol. VII, p. 85.

47. A. C. Beer, "Galvanomagnetic Effects in Semiconductors," Solid State Physics Supplement 4, Ed. F. Seitz and D. Turnbull. (Academic Press, New York, 1963) p. 130.

VITA

Leonard Chester Laskowski

Candidate for the Degree of

Doctor of Philosophy

Thesis: AN INVESTIGATION OF THE TRANSPORT PROPERTIES OF HOLES IN A SEMICONDUCTING DIAMOND

Major Field: Physics

Biographical:

Personal Data: Born in Chicago, Illinois, June 30, 1942, the son of Chester and Antonette Laskowski.

Education: Graduated from Saint Patrick High School, Chicago, Illinois, in May, 1960; attended Northwestern University, Summer of 1961; attended DePaul University and Wilbur Wright Junior College, Summer of 1962; received the Bachelor of Arts degree with a major in physics from Saint Mary's College, Winona, Minnesota, in May, 1964; National Science Foundation Undergraduate Research Participant award, 1963-1964; awarded National Aeronautics and Space Administration Traineeship, 1966-1969; completed requirements for the Doctor of Philosophy degree at Oklahoma State University in July, 1972.

Professional Experience: Undergraduate Teaching Assistant, Saint Mary's College Physics Department, 1963; Graduate Teaching Assistant, Oklahoma State University Physics Department, 1964-1966 and 1969-1971.

Professional Organizations: Sigma Pi Sigma, National Physics Honor Society; Delta Epsilon Sigma, Scholastic Honor Society.